The Astrophysical Journal, 989:182 (38pp), 2025 August 20 https://doi.org/10.3847/1538-4357/adea38

Evidence for an Instability-induced Binary Merger in the Double-peaked, Helium-rich Type IIn Supernova 2023zkd

A. Gagliano[1,2,3], V. A. Villar[1,2], T. Matsumoto[4,5], D. O. Jones[6], C. L. Ransome[2], A. E. Nugent[2], D. Hiramatsu[1,2], K. Auchettl[7,8], D. Tsuna[9,10], Y. Dong[2], S. Gomez[2], P. D. Aleo[11,12], C. R. Angus[13], T. de Boer[14], K. A. Bostroem[15,26], K. C. Chambers[14], D. A. Coulter[16], K. W. Davis[8], J. R. Fairlamb[14], J. Farah[17,18], D. Farias[19], R. J. Foley[8], C. Gall[19], H. Gao[14], E. P. Gonzalez[17,18], D. A. Howell[17,18], M. E. Huber[14], C. D. Kilpatrick[20], C.-C. Lin[14], T. B. Lowe[14], M. E. MacLeod[2], E. A. Magnier[14], C. McCully[17,18], P. Mínguez[14], G. Narayan[11,12], M. Newsome[17,18], K. C. Patra[8,21], A. Rest[16,22], S. Rest[23], S. Smartt[13,24], K. W. Smith[13,24], G. Terreran[25], R. J. Wainscoat[14], Q. Wang[3], S. K. Yadavalli[2], and Y. Zenati[16,22]

[1] The NSF AI Institute for Artificial Intelligence and Fundamental Interactions, USA; alexander.gagliano@cfa.harvard.edu
[2] Center for Astrophysics | Harvard & Smithsonian, Cambridge, MA 02138, USA
[3] Department of Physics and Kavli Institute for Astrophysics and Space Research, Massachusetts Institute of Technology, 77 Massachusetts Avenue, Cambridge, MA 02139, USA
[4] Department of Astronomy, Kyoto University, Kitashirakawa-Oiwake-cho, Sakyo-ku, Kyoto, 606-8502, Japan
[5] Hakubi Center, Kyoto University, Yoshida-honmachi, Sakyo-ku, Kyoto, 606-8501, Japan
[6] Institute for Astronomy, University of Hawai'i, 640 N. A'ohoku Place, Hilo, HI 96720, USA
[7] OzGrav, School of Physics, The University of Melbourne, VIC 3010, Australia
[8] Department of Astronomy and Astrophysics, University of California, Santa Cruz, CA 95064, USA
[9] TAPIR, Mailcode 350-17, California Institute of Technology, Pasadena, CA 91125, USA
[10] Research Center for the Early Universe (RESCEU), School of Science, The University of Tokyo, Bunkyo-ku, Tokyo 113-0033, Japan
[11] Department of Astronomy, University of Illinois at Urbana-Champaign, 1002 W. Green Street, IL 61801, USA
[12] Center for AstroPhysical Surveys (CAPS) Fellow
[13] Astrophysics Research Centre, School of Mathematics and Physics, Queen's University Belfast, Belfast BT7 1NN, UK
[14] Institute for Astronomy, University of Hawaii, 2680 Woodlawn Drive, Honolulu, HI 96822, USA
[15] Steward Observatory, University of Arizona, 933 North Cherry Avenue, Tucson, AZ 85721-0065, USA
[16] Space Telescope Science Institute, Baltimore, MD 21218, USA
[17] Las Cumbres Observatory, 6740 Cortona Drive, Suite 102, Goleta, CA 93117, USA
[18] Physics Department, University of California, Santa Barbara, Santa Barbara, CA 93106, USA
[19] DARK, Niels Bohr Institute, University of Copenhagen, Jagtvej 155A, 2200 Copenhagen, Denmark
[20] Center for Interdisciplinary Exploration and Research in Astrophysics (CIERA) and Department of Physics and Astronomy, Northwestern University, Evanston, IL 60208, USA
[21] University of California, Observatories 1156 High Street Santa Cruz, CA 95064, USA
[22] Physics and Astronomy Department, Johns Hopkins University, Baltimore, MD 21218, USA
[23] Department of Computer Science, The Johns Hopkins University, Baltimore, MD 21218, USA
[24] Department of Physics, University of Oxford, Denys Wilkinson Building, Keble Road Oxford OX1 3RH, UK
[25] Adler Planetarium, 1300 S. DuSable Lake Shore Drive, Chicago, IL 60605, USA

Received 2025 February 26; revised 2025 May 20; accepted 2025 May 27; published 2025 August 13

Abstract

We present ultraviolet to infrared observations of the extraordinary Type IIn supernova 2023zkd (SN 2023zkd). Photometrically, it exhibits persistent and luminous precursor emission spanning ∼4 yr preceding discovery ($M_r \approx -15$ mag, 1500 days in the observer frame), followed by a secondary stage of gradual brightening in its final year. Post-discovery, it exhibits two photometric peaks of comparable brightness ($M_r \lesssim -18.7$ mag and $M_r \approx -18.4$ mag, respectively) separated by 240 days. Spectroscopically, SN 2023zkd exhibits highly asymmetric and multicomponent Balmer and He I profiles that we attribute to ejecta interaction with fast-moving (1000–2000 km s^{-1}) He-rich polar material and slow-moving (∼400 km s^{-1}) equatorially distributed H-rich material. He II features also appear during the second light curve peak and evolve rapidly. Shock-driven models fit to the multiband photometry suggest that the event is powered by interaction with ∼5–6 $M_\odot$ of CSM, with 2–3 $M_\odot$ associated with each light curve peak, expelled during mass-loss episodes ∼3–4 yr and ∼1–2 yr prior to explosion. The observed precursor emission, combined with the extreme mass-loss rates required to power each light curve peak, favors either super-Eddington accretion onto a black hole or multiple long-lived eruptions from a massive star to luminosities that have not been previously observed. We consider multiple progenitor scenarios for SN 2023zkd, and find that the brightening optical precursor and inferred explosion properties are most consistent with a massive ($M_{\rm ZAMS} \geqslant 30\,M_\odot$) and partially stripped He star undergoing an instability-induced merger with a black hole companion.

---

[26] LSST-DA Catalyst Fellow.

Unified Astronomy Thesaurus concepts: Core-collapse supernovae (304); Circumstellar matter (241); Spectroscopy (1558); Photometry (1234)

Materials only available in the online version of record: data behind figure

1. Introduction

The observational taxonomy of stars that end their lives as core-collapse supernovae (CCSNe) continues to grow. Multiyear, wide-field imaging surveys such as the Zwicky Transient Facility (ZTF; E. C. Bellm et al. 2019; R. Dekany et al. 2020), the Young Supernova Experiment (YSE; D. O. Jones et al. 2021; P. D. Aleo et al. 2023), and the Asteroid Terrestrial-impact Last Alert System (ATLAS; J. L. Tonry et al. 2018), have enabled detailed photometric analyses of SNe from the photospheric to the nebular phase.

Of particular interest are CCSNe with significant photometric variability following their primary peak. These events cannot be naturally explained by the radioactive decay chain of ^{56}Ni→ ^{56}Co→ ^{56}Fe, or by recombination in the ejecta. Observations of these events instead indicate the presence of circumstellar material (CSM), which can produce a broad diversity of photometric and spectroscopic signatures during SN interaction due to its efficient conversion of kinetic energy and during SN shock breakout due to its re-processing of high-energy photons (N. Smith 2014 provides a conceptual picture of SN–CSM interaction, and Figure 3 of D. K. Khatami & D. N. Kasen 2024 provides a sense of the variety of possible photometric signatures).

From the recombination of the photoionized CSM, strongly interacting transients may reveal narrow spectral lines of H (as with SNe IIn; E. M. Schlegel 1990; A. V. Filippenko 1997), He (SNe Ibn; A. Pastorello et al. 2008a; N. N. Chugai 2009), or C and O while lacking H/He (SNe Icn; A. Gal-Yam et al. 2021, 2022; C. Pellegrino et al. 2022). Where the density of the CSM deviates from spherical symmetry or cannot be parameterized as a smooth power-law profile with radius, interacting SNe can also re-brighten to a secondary photometric maximum (as seen in, e.g., the type Ib SN 2005bf; G. Folatelli et al. 2006; the candidate pair-instability SN 2016iet; S. Gomez et al. 2019; the ambiguous stripped-envelope SN 2020acct; C. R. Angus et al. 2024; the type Ic SN 2019cad; C. P. Gutiérrez et al. 2021; the type Ic/Luminous SN 2019stc; S. Gomez et al. 2021; the type IIn SN 2021qqp; D. Hiramatsu et al. 2024b; and the type Ic SN 2022xxf; H. Kuncarayakti et al. 2023, among others). Because CSM can be formed from mass-loss episodes in the months to years prior to core collapse, observations of these strongly interacting transients are of vital importance for reconstructing the extremes of late-stage stellar evolution.

A second, complementary benefit of our growing photometric data sets is the ability to identify enhanced emission from a terminal system prior to core collapse. In some cases, these "precursor events" are luminous enough to be confused for an explosion itself. The most well studied of these precursor events is 2009ip, which was initially reported to be an SN until being spectroscopically confirmed as a luminous impostor with a dramatic re-brightening phase in 2012 (E. Berger et al. 2009; J. Maza et al. 2009; N. Smith et al. 2010; R. J. Foley et al. 2011; A. J. Drake et al. 2012; M. Fraser et al. 2013; J. C. Mauerhan et al. 2013; A. Pastorello et al. 2013; J. L. Prieto et al. 2013; N. Smith et al. 2013; M. L. Graham et al. 2014; E. M. Levesque et al. 2014; R. Margutti et al. 2014; J. C. Martin et al. 2014; T. J. Moriya 2015; M. L. Graham et al. 2017; E. Reilly et al. 2017; N. Smith et al. 2022; T. Pessi et al. 2023). SN 2015bh is another extreme case: optical variability spanning 20 yr concluded with a putative explosion peaking at $M_r < -18$ mag, although the interpretation of this final event as terminal is debated (N. Elias-Rosa et al. 2016; C. C. Thöne et al. 2017). The population of detected CCSN precursors has grown increasingly heterogeneous in the intervening years (A. Gagliano et al. 2025), and now includes the persistent and months-long emission preceding at least one normal SN II (SN 2020tlf; W. V. Jacobson-Galán et al. 2022); the years-long and quasiperiodic near-IR (NIR) variability associated with the nearby SN II 2023ixf; (C. D. Kilpatrick et al. 2023); and the years-long and steadily brightening optical emission preceding the SN Ibn 2023fyq (S. J. Brennan et al. 2024a; Y. Dong et al. 2024; D. Tsuna et al. 2024).

Systematic searches for precursors to SNe IIn, specifically, suggest that luminous pre-explosion emission is common. Luminosity estimates range from 25% of all events for $M_r < -13$ mag precursors in the final 3 months preceding explosion (N. L. Strotjohann et al. 2021) to >30% of all SNe IIn (A. Reguitti et al. 2024). When attributed to a steady-state wind from the progenitor, the luminosity of this emission indicates mass-loss rates of 10^{-4}–$1\,M_{\odot}\,\mathrm{yr}^{-1}$, significantly higher than can be explained by line-driven winds alone (F. Taddia et al. 2013; T. J. Moriya et al. 2014; C. L. Ransome & V. A. Villar 2025). Multiple alternative physical mechanisms have been proposed to power these brightening phases, including energy deposition in the core associated with late-stage nuclear burning (S. E. Woosley et al. 2002); wave damping from vigorous stellar convection (E. Quataert & J. Shiode 2012; J. H. Shiode & E. Quataert 2014; J. Fuller 2017; J. Fuller & S. Ro 2018; S.-C. Leung & J. Fuller 2020; S. C. Wu & J. Fuller 2022); centrifugally induced mass loss (F. Lignieres et al. 2000; J. Fuller & S. Ro 2018; X. Zhao & J. Fuller 2020); and binary interaction (N. Smith & W. D. Arnett 2014; A. Ercolino et al. 2024).

Precursor emission, in addition to characterizing the mass deposited in the terminal star's surroundings, provides insights into the nature of the progenitor itself (T. Matsumoto & B. D. Metzger 2022). The high mass-loss rates and CSM velocities associated with SN IIn precursors have been likened to the massive eruptions of luminous blue variables (LBVs), two of which have been well documented in our own Galaxy (η Carinae and P Cygni; G. Israelian & M. de Groot 1999). Though the massive outbursts of these Galactic sources are not causally connected to core collapse (and traditional stellar theory predicts an LBV as a brief transitionary stage for stars of mass $M_{\mathrm{ZAMS}} > 30\,M_{\odot}$ en route to an H-free Wolf–Rayet (W-R), instead of a stellar endpoint; R. M. Humphreys & K. Davidson 1994; N. Smith 2017a), an LBV-like origin for SNe IIn has other observational support. Pre-explosion photometry with the Hubble Space Telescope (HST) is consistent with an LBV-like progenitor for SN 2005gl (A. Gal-Yam & D. C. Leonard 2009), SN 2009ip (R. J. Foley et al. 2011), SN 2010bt

(N. Elias-Rosa et al. 2018), SN 2015bh (J. E. Jencson et al. 2022), and SN 2010jl (N. Smith et al. 2011b).[27]

The LBV interpretation is actively debated. SNe IIn whose progenitors exhibit eruptive episodes span a wider mass range than can be easily explained by LBVs alone (J. L. Prieto et al. 2008; T. A. Thompson et al. 2009). Spectropolarimetric measurements of SNe IIn also suggest enduring CSM asymmetries not expected for an isotropic outburst in a pristine environment (C. Bilinski et al. 2024).

Binary interaction between an LBV-like primary and its massive companion may naturally be able to explain the additional diversity, both in SN IIn precursors and the more ambiguous but closely related "SN impostors" (A. Kashi 2010; N. Smith et al. 2011a; R. A. Chevalier 2012; N. Smith & W. D. Arnett 2014; A. Ercolino et al. 2024; T. Matsuoka & R. Sawada 2024). Indeed, binary interaction has been proposed to explain the presence of Galactic LBVs in locations incompatible with the young stellar clusters where massive stars are born (N. Smith & R. Tombleson 2014). Binary kicks may also explain the substantial fraction of low-redshift SNe IIn not occurring in the star-forming regions of their host galaxies (C. L. Ransome et al. 2022). A binary LBV system was recently suggested for the SN impostor 2000ch to explain its periodic eruptions (M. Aghakhanloo et al. 2023), and for 2020ywx because of the event's long-lived CSM interaction (R. Baer-Way et al. 2025).

SNe IIn exhibiting both a luminous precursor event and photometric variability from CSM interaction offer a unique opportunity to unify distinct lines of evidence into a unified picture of the pre-explosion system. We now undertake this task for SN 2023zkd, a helium-rich SN IIn with two photometric peaks and a years-long precursor that steadily brightens to event discovery. As we will later argue, SN 2023zkd's unique photometric and spectroscopic evolution provide renewed evidence for the role of binary interaction in type IIn explosions.

This paper is organized as follows. We describe our photometric and spectroscopic observations in Section 2, from the archival imaging used to construct the pre-discovery light curve to the optical and NIR spectroscopy spanning the post-discovery peaks. We model the spectral energy distribution (SED) of the SN host galaxy in Section 3 and infer its global properties. In Section 4, we describe 2023zkd's unique photometric evolution following discovery. We characterize the spectroscopic sequence of SN 2023zkd in detail in Section 5. We present evidence for multiple CSM components (Section 5.3), evaluate the ambiguous spectroscopic classification of the event in the context of other He-rich SNe IIn (Section 5.4), and constrain the density of the interaction region using the Balmer decrement (Section 5.5). Next, we infer the blackbody properties of the SN from precursor to secondary maximum in Section 6. In Section 7, we use multiple shock-luminosity models to infer the properties of the CSM and reconstruct the mass-loss history of the progenitor system. Finally, we discuss the most likely interaction geometry for the event in Section 8.1 and consider potential progenitor systems in Section 8.2. We conclude with our main findings in Section 9.

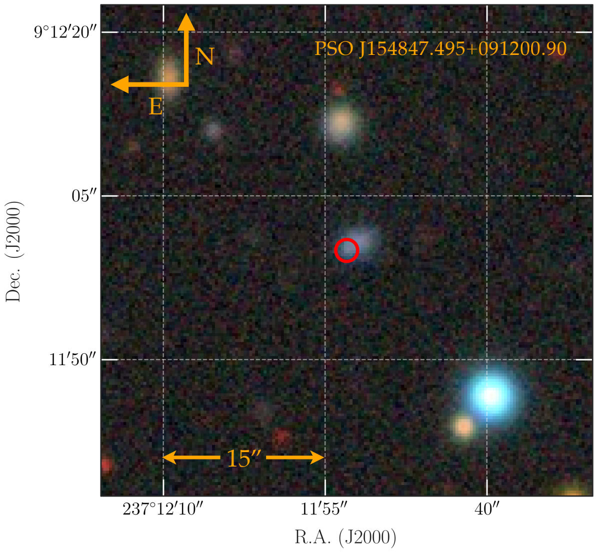

Figure 1. *grz*-band color image of the explosion site of SN 2023zkd from the Dark Energy Camera Legacy Survey (DECaLS) Data Release 9 (A. Dey et al. 2019). The SN location is denoted by the red circle with radius 1″, and the image scale is given in the bottom left. The host galaxy at image center is PS0 J154847.495+091200.90, with a spectroscopic redshift of $z = 0.0560 \pm 0.0002$.

We have corrected all photometry and spectroscopy for Galactic extinction assuming the K. D. Gordon et al. (2023) extinction law, where $E(B-V) = 0.038$ mag (E. F. Schlafly & D. P. Finkbeiner 2011). We have further corrected all observations for a host extinction of $A_V = 0.35$ mag (or $E(B-V) = 0.11$ mag, assuming a Milky Way–like $R_V = 3.1$ for the host), which is inferred from the SED of the host galaxy derived in Section 3. We have adopted an event redshift of $z = 0.0560 \pm 0.0002$ measured from the peak of the Hα emission in a host spectrum obtained obtained on 2025 April 22.

Throughout this paper, we assume a flat Λ cold dark matter cosmology with $H_0 = 70\,\mathrm{km\,s^{-1}\,Mpc^{-1}}$, $\Omega_M = 0.3$, and $\Omega_\Lambda = 0.7$. All dates are given in UTC. Unless otherwise noted, phases are presented in rest-frame days relative to the observed maximum of the first photometric peak in ZTF-*r*, which we calculate from an uncertainty-weighted average of the dates of four comparable observations to be MJD $\approx 60290.6 \pm 1.2$.

2. Data

SN 2023zkd was discovered by the ZTF on 2023 July 7 at 04:36:28.8 UTC (MJD = 60132.5) with an apparent brightness of 20.6 in ZTF-*r* (C. Fremling 2023). The SN occurred at (J2000) $(\alpha, \delta) = (15^{\mathrm{hr}}48^{\mathrm{m}}47\overset{\mathrm{s}}{.}536, +09^\circ12'00\overset{''}{.}28$, $0\overset{''}{.}58$ South and $0\overset{''}{.}70$ East of the center of its host galaxy (PSO J154847.495+091200.90, shown in Figure 1). SN 2023zkd was later flagged on the morning of 2024 January 18 (MJD $\approx$ 60327) by the Light curve Anomaly Identification and Similarity Search (LAISS; P. D. Aleo et al. 2024) tool running within the ANTARES Astronomical Time-domain Event Broker (T. Matheson et al. 2021) and integrated into the Young Supernova Experiment via a Slack bot (details on the event's early anomalous features are provided in Appendix B). A classification spectrum was obtained by our group

---

[27] This interpretation comes primarily from the luminosities of the pre-explosion systems, in tandem with the velocities of H-rich material measured in spectra obtained post-explosion. These properties do not unambiguously indicate an LBV (see V. V. Dwarkadas 2011 and C. L. Ransome & V. A. Villar 2025 for related discussions).

(P.I. Gagliano) with the Magellan Low Dispersion Survey Spectrograph 3 (LDSS-3; J. Allington-Smith et al. 1994) on 2024 March 17 (+90 days).

We determined an initial type IIn classification for the event by comparing our +90 day spectrum to templates in the GEneric cLAssification TOol (GELATO)[28] and noting the prominent multicomponent Balmer features. A public type Ibn classification was later released on the Transient Name Server[29] (TNS) on 2024 July 13 (J. Duarte et al. 2024) (+202.2 days), when the Hα feature was less prominent.

Statistically significant $>3\sigma$ positive flux was detected in unbinned difference imaging at the SN site in Pan-STARRS (K. C. Chambers et al. 2016) GPC1-w on 2023 March 30 (MJD $\approx$ 60033.6, $m_w \approx 21.4$), 98.9 days before discovery in the observer frame. This preliminary measurement hinted at enhanced emission from the pre-explosion system. We have undertaken a comprehensive analysis of archival imaging at the explosion site, and detect statistically significant ($>3\sigma$) positive flux in 50 day bins spanning $\sim$1500 days prior to discovery and in photometric filters from ZTF, ATLAS, and Pan-STARRS.

2.1. Optical Photometry

2.1.1. FLWO/Keplercam

We observed SN 2023zkd with the KeplerCam Camera on the 1.2 m Telescope at the at the Fred Lawrence Whipple Observatory (FLWO) from MJD 60416.23 to 60576.17 (+110.0 days to +270.4 days). Photometric observations were reduced using a custom point-spread function (PSF) photometry routine in python. Bias and flat frames were also obtained. Multiple exposures were obtained for each observation, and images from the same night were stacked using SWarp (E. Bertin et al. 2002). The PSF was constructed from a customized version of SExtractor (E. Bertin & S. Arnouts 1996) written in python, with calibrations from the Pan-STARRS catalog (K. C. Chambers et al. 2016). Template images in the field of SN 2023zkd were obtained using PANSTAMPS (D. Young 2023), and template subtraction was done using `Pyzogy` (D. Guevel & G. Hosseinzadeh 2017).[30] Only observations $\geqslant 5\sigma$ above the calculated noise background after template subtraction are reported.

2.1.2. Atlas

We queried the ATLAS forced photometry web service[31] (K. W. Smith et al. 2020; L. Shingles et al. 2021) for photometry at the explosion site, and obtained observations spanning MJD 57230.3 (−2898.0 days) to MJD 60561.3 (+256.3 days). We used the `ATClean` code (S. Rest et al. 2024) to identify bad flux measurements and account for systematics in the reported c- and o-band photometry. We requested 10 control light curves in an annulus of radius 15″ surrounding the SN site to calibrate uncertainties across phases. We further applied the quality cuts recommended in S. Rest et al. (2024) and removed measurements with $\chi^2 > 4$, flux uncertainty $>160\,\mu$Jy, and $\chi/N > 10$ (where N is the number of points used to fit the pointing PSF).

The templates used to produce ATLAS differential forced photometry were changed on approximately MJD $\approx$ 58417 (2018 October 26) and MJD $\approx$ 58882 (2020 February 3). To avoid step-like artifacts in the pre-explosion flux measurements from these changes, we separately estimated and subtracted baseline flux values between $58417 < \text{MJD} < 58882$ and MJD > 58882 (we did not consider photometry prior to MJD $\approx$ 58417). In each window, we computed the median flux from the first 200 days of observations, removed values $>1\sigma$ from the median, and re-computed the median from the remaining data. We have ensured that >20 observations remain after sigma-clipping to estimate a robust baseline. We then subtracted this value from flux measurements within each window and proceeded with binning using the same procedure as for ZTF data (Section 2.1.4).

We binned all post-explosion photometry in 50 day bins pre-explosion and 5 day bins post-explosion if a bin contained at least two flux measurements. Due to the potential for systematics remaining after our multibaseline binning procedure, we report only detections with $>5\sigma$ significance prior to discovery and $>3\sigma$ following discovery.

2.1.3. Pan-STARRS

SN 2023zkd was observed in *grizyw* filters with the Pan-STARRS GPC1 telescope from MJD 57179.3 (-2946.3 days) to MJD 60544.3 (+240.2 days). Photometry was reduced using the University of Hawaii's PS1 Image Processing Pipeline IPP (IPP; E. A. Magnier et al. 2020a, 2020b). Pan-STARRS images were ingested, processed, and archived by IPP, then underwent template image convolution and subtraction. PS1 template images were created from stacked exposures (primarily the PS1 3π survey), from which new nightly images were resampled and astrometrically aligned to match a skycell in the PS1 sky tessellation. A nightly image zero-point was calculated by comparing PS1 stellar catalogs (K. C. Chambers et al. 2016) to the PSF photometry. Template images were then convolved with nightly images and matched to their PSF via a three-Gaussian kernel before being subtracted with the `HOTPANTS` code (C. Alard 2000; A. Becker 2015). Photometry was then obtained using the `Photpipe` forced photometry pipeline (A. Rest et al. 2005, 2014), where epochs flagged as potentially having bad pixels are removed. For all other epochs, a flux-weighted centroid was forced to be at the transient candidate position and a nightly zero-point was applied to calculate the source's brightness. Final data were then accessed through the YSE's transient management platform, `YSE-PZ` (D. A. Coulter et al. 2022, 2023).

The SN was also observed in *iw* filters with the Pan-STARRS GPC2 camera from MJD 58664.4 (−1540.0 days) to MJD 60540.3 (+236.4 days). As Pan-STARRS GPC2 zero-points are not well calibrated, and the majority of pre-explosion observations could not be successfully reduced using `Photpipe`, we report only post-discovery GPC2 photometry.

2.1.4. Zwicky Transient Facility

We queried the ZTF forced photometry service (F. J. Masci et al. 2019) for differential photometry at the explosion site spanning the full duration of the survey. We followed a similar procedure to that outlined in F. J. Masci et al. (2023) to

---

[28] https://gelato.tng.iac.es/

[29] https://www.wis-tns.org/

[30] https://github.com/dguevel/PyZOGY

[31] https://fallingstar-data.com/forcedphot/

analyze the pre-explosion forced photometry at the explosion site. We applied a series of nominal quality cuts (ensuring $\chi^2 < 1.4$, removing all observations with `procstatus = 56` or `seeing > 4`, and excluding *g*-band photometry between MJD 58119.5 and MJD 58139.5 where images are reported to be miscalibrated). We used the reported difference image χ^2 values at each epoch to re-scale reported flux uncertainties. For pre-discovery epochs, we defined a reference baseline flux value as the median flux value >1700 days before the discovery date while ensuring that there are at least 30 epochs within the reference period for each band and field combination. We subtracted all flux measurements by this value, and rescaled flux uncertainties to account for potential systematics identified during the baseline subtraction.

Next, we placed all difference flux observations on a consistent reference zero-point and defined 50 day bins spanning all pre-discovery epochs and 1 day bins spanning all post-discovery epochs. Our bin size was chosen as a trade-off between the number of detections and the statistical significance of each detection; nonetheless, statistically significant pre-explosion emission is detected with bin widths of 5–200 days. We computed uncertainty-weighted averages of flux values in each bin, and converted the binned fluxes to magnitude using the reference binned zero-point. We report statistically significant detections ($>3\sigma$) at each bin center, and nondetections were converted to 5σ upper limits using the reference zero-point.

2.1.5. Las Cumbres Observatory

As part of the Global Supernova Project (D. A. Howell 2017), we obtained *BgVri*-band imaging data for SN 2023zkd with the Las Cumbres Observatory (LCO; T. M. Brown et al. 2013) network of 1m robotic telescopes with Sinistro cameras and spanning Cerro Tololo Inter-American Observatory (Región IV, Chile), McDonald Observatory (Texas, USA), South African Astronomical Observatory (Sutherland, South Africa), and Teide Observatory (Canary Islands, Spain). The observations covered the secondary photometric peak from MJD 60508.1 to MJD 60593.1 (+206.0 days to +286.5 days). LCO photometry was performed with PSF fitting using `lcogtsnpipe`[32] (S. Valenti et al. 2016), a PyRAF-based photometric reduction pipeline. *BV* and *gri*-band data were calibrated to Vega and AB magnitudes, respectively, using the ninth Data Release of the AAVSO Photometric All Sky Survey (A. A. Henden et al. 2016) using the 13th Data Release of the Sloan Digital Sky Survey (SDSS; F. D. Albareti et al. 2017).

2.2. UV Photometry

The SN site was observed with the Swift Ultra-Violet/Optical Telescope (P. W. A. Roming et al. 2005; ObsIDs: 00016727001-00016727006) at eight epochs spanning MJD = 60514.5 (+211.9 days) to MJD = 60545.5 (+241.4 days). Following the analysis steps described in P. J. Brown et al. (2014), we used `uvotsource` from the `HEASoft v6.26` package to perform aperture photometry on UVOT pointings within a 3″ aperture centered on SN 2023zkd. We estimated the background flux at the SN site using an annulus with inner radius 6″ and outer radius 6″ centered on the SN. The aperture-corrected background flux was then subtracted from all observations to obtain differential photometry.

2.3. X-Ray

In addition to the Swift UVOT data, contemporaneous X-ray observations were taken by the Neil G. Gehrels Swift X-Ray Telescope (XRT) in photon-counting mode (ObsIDs: 00016727001-00016727008). All observations were reprocessed with the standard filter and screening criteria[33] as well as the most recent calibration files from level one XRT data using XRTPIPELINE version 0.13.7. Using a source region with a radius of 49″ centered on the location of 2023zkd and a source-free background region with a radius of 150″ centered at $(\alpha,\delta) = (15{:}48{:}37.8212, +9{:}19{:}32.377)$, no significant X-ray emission associated with the source was detected in individual epochs. To increase the signal-to-noise ratio of our observations, we merged all eight individual Swift observations using XSELECT version 2.5b. We find no significant X-ray emission arising from SN 2023zkd. Using the source and background regions above, we have derived a 3σ upper limit to the 0.3–10.0 keV count rate of 0.004 counts s^{-1}. Assuming a galactic column density of $3.72 \times 10^{20}\ \mathrm{cm}^{-2}$ derived from R. Willingale et al. (2013) and adopting a thermal Brehmsstrahlung source spectrum with $kT \approx 19$ keV as suggested by the strongly interacting type IIn SN 2010jl (P. Chandra et al. 2015),[34] we obtained a 3σ upper limit on the unabsorbed flux (0.3–10.0 keV) of $2.06 \times 10^{-13}\ \mathrm{erg\ cm^{-2}\ s^{-1}}$. Assuming a redshift of $z = 0.056$, this corresponds to an X-ray luminosity of $1.5 \times 10^{42}\ \mathrm{erg\ s^{-1}}$.

2.4. Optical and NIR Spectroscopy

In this section, we outline the spectroscopic sequence obtained for SN 2023zkd. The dates, phases, and wavelength coverage of each obtained spectrum are summarized in Table 1. All spectra will be publicly released via WISeREP[35] (O. Yaron & A. Gal-Yam 2012) following publication.

2.4.1. MMT/Binospec

We obtained two spectra of SN 2023zkd with the Binospec wide-field optical spectrograph on the 6.5 m MMT through a follow-up program on behalf of the Young Supernova Experiment on MJD 60555.1 (+250.5 days) and MJD 60563.1 (+258.1 days). An additional spectrum was obtained at the explosion site on MJD 60787.0 (+470.1 days), after the SN had dimmed, for host fitting (Section 3). Each spectrum was obtained with the 270 line grating, LP3800 blocking filter, a 1″ slit width, and a central wavelength of 6500 Å. We reduced the spectra with standard reduction methods using the `redspec` pipeline[36] (S. Gomez 2024), which uses a combination of standard IRAF routines and the `twodspec` package.

2.4.2. Magellan/LDSS-3

We also obtained three spectra of SN 2023zkd with the LDSS-3 spectrograph mounted atop the Magellan 6.5 m Clay

---

[32] https://github.com/LCOGT/lcogtsnpipe/

[33] https://swift.gsfc.nasa.gov/analysis/xrt_swguide_v1_2.pdf

[34] This event exhibited an LBV-like progenitor and multiple spectroscopic similarities to 2023zkd; we discuss these in subsequent sections.

[35] https://www.wiserep.org/

[36] https://github.com/gmzsebastian/redspec

Table 1
Spectroscopic Observations of SN 2023zkd

Observation Date (UT)	MJD	Phase (Days)	Telescope	Spectrograph	Wavelength Range (Å)	Exposure Time (s)
2024-03-17	60386.1	+90.4	Magellan	LDSS-3	3800–10000	2700
2024-07-13	60504.1	+202.2	NTT	EFOSC2	3000–8800	Unk.[a]
2024-07-19	60510.9	+208.7	NOT	ALFOSC	3500–8500	3063
2024-07-22	60514.0	+211.5	NOT	ALFOSC	3500–8500	3063
2024-07-27	60519.0	+216.3	NOT	ALFOSC	3500–8500	3063
2024-08-01	60523.3	+220.4	Gemini-North	GNIRS	9000–24000	6300
2024-08-03	60525.0	+222.0	NOT	ALFOSC	3500–8500	3063
2024-08-08	60530.1	+226.8	Magellan	LDSS-3	3800–9000	1800
2024-08-16	60538.2	+234.5	Shane	KAST	3500–9000	3000[b]
2024-09-01	60555.0	+250.4	Magellan	LDSS-3	3800–10000	1800
2024-09-02	60555.1	+250.5	MMT	Binospec	3500–8800	1950
2024-09-10	60563.1	+258.0	MMT	Binospec	3500–8800	2250
2025-04-22	60787.0	+470.1	MMT	Binospec	3500–8800	3300

Notes. All phases are presented in rest-frame days relative to the first ZTF-*r* peak at MJD = 60290.6.

[a] Public TNS spectrum; exposure time unknown.

[b] Exposure time for each (red/blue) side of the spectrograph.

telescope on MJD 60530.1 (+226.8 days), MJD 60386.1 (+90.4 days), and MJD 60555.0 (+250.4 days). All spectra were obtained in three exposures using a $1''$ slit, the LP3800 filter, and 270 grating set to a central wavelength of 6500 Å. We set 900 s per exposure for the first spectrum and 600 s per exposure for the final two. Spectra were reduced using the same pipeline as the MMT/Binospec data.

2.4.3. NOT/ALFOSC

We obtained four spectra of SN 2023zkd using the Alhambra Faint Object Spectrograph and Camera (ALFOSC) mounted on the Nordic Optical Telescope (NOT). The ALFOSC spectra were taken with a $1''$ slit and grism 4. All spectra were bias subtracted, flat-fielded, wavelength-calibrated, and then extracted using standard routines within `IRAF`. Nightly spectroscopic standard stars were used for flux calibration.

2.4.4. Gemini-North/GNIRS

We used the Gemini-North Near-IR Spectrograph (GNIRS) to obtain a single NIR spectrum of SN 2023zkd on 2024 August 1 (MJD ≈ 60523.3, +220.4 days), during the secondary photometric maximum. Observations were taken with the SXD prism and 32mm cross-disperser grating, in 21 exposures of 300 s each. The spectrum was reduced in the standard manner with the PypeIt pipeline (J. X. Prochaska et al. 2020).

3. Host-galaxy Properties with Prospector

SN 2023zkd's ambiguous spectroscopic classification motivates an investigation into its host properties, as systematic differences have been found between the hosts of archival SNe IIn, SLSNe IIn, and SNe Ibn (see Figure 7 of Y.-J. Qin & A. Zabludoff 2024; see also Figure 12 of S. Schulze et al. 2021). The derived global properties of the host, including its stellar mass and star formation rate (SFR), can also provide indirect evidence for a particular progenitor system (S. M. Habergham et al. 2014; C. L. Ransome et al. 2022; T. J. Moriya et al. 2023).

An ongoing challenge in galaxy SED fitting lies in aggregating catalog-level photometry from diverse surveys, each obtained from instruments with distinct systematics and extracted using survey-specific techniques. To circumvent this issue, we use the `BLAST` web application (D. O. Jones et al. 2024; A. E. Nugent et al. 2025, in preperation) to retrieve postage stamps of the host galaxy in GALEX (D. C. Martin et al. 2005), Pan-STARRS, SDSS (D. G. York et al. 2000; M. R. Blanton et al. 2017), Dark Energy Survey (DES; A. Dey et al. 2019), and Two Micron All Sky Survey (2MASS; M. F. Skrutskie et al. 2006). We use the morphological properties of the host reported in Pan-STARRS to construct global PSF-matched elliptical apertures and extract photometry for the host in each filter. The host galaxy is detected in GALEX (*far-UV* and *near-UV*), Pan-STARRS (*griz*), SDSS (*ugriz*), and DES (*gz*). The source is not detected in 2MASS *J* and *K*; given the large aperture correction required to account for the $1''$ pixel scale, we convert the raw flux measurements to 3σ upper limits for SED fitting.

We constrain the stellar population properties of the host galaxy using `Prospector` (J. Leja et al. 2019; B. D. Johnson et al. 2021). Within `Prospector`, we apply a nested sampling fitting routine through `dynesty` (J. S. Speagle 2020) to jointly fit the observed host photometry and upper limits with the host spectrum and obtain posterior distributions on the stellar population properties of interest, including redshift, mass formed (M_F), stellar metallicity (Z_*), and dust attenuation from old ($\tau_{v,2}$) and young ($\tau_{v,1}$) stellar light. We construct a model SED with `FSPS` and `python-FSPS` (C. Conroy et al. 2009; C. Conroy & J. E. Gunn 2010), which internally uses the `MIST` stellar isochrones (B. Paxton et al. 2011, 2013, 2015; J. Choi et al. 2016; A. Dotter 2016) and `MILES` spectral library (P. Sánchez-Blázquez et al. 2006; J. Falcón-Barroso et al. 2011).

For the `Prospector` SED fit, we employ a G. Chabrier (2003) initial mass function, the M. Kriek & C. Conroy (2013) dust attenuation model, which measures an offset from the D. Calzetti et al. (2000) attenuation curves and determines the fraction of light attenuated from old to young stellar light, a nebular emission model, and the A. Gallazzi et al. (2005) mass–metallicity relation to probe realistic M_F and Z_*

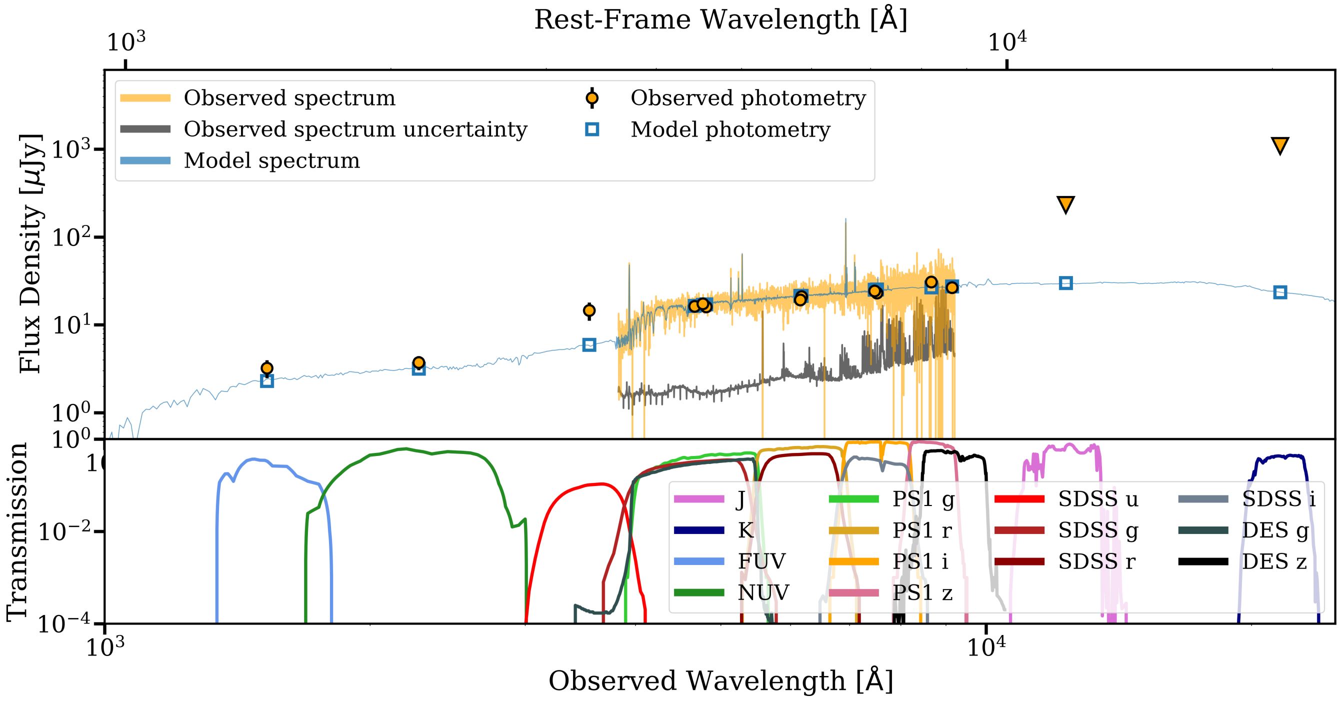

Figure 2. The model spectrum derived at the median of the posterior distributions (blue line) and its associated photometry (blue squares) compared to the observed host photometry (orange circles) and spectrum (orange line). Note that 2MASS near-IR (NIR) observations have been converted to 5σ upper limits (orange triangles). Transmission curves for UV, optical, and NIR photometry are shown in the bottom panel. The model underestimates the observed SDSS-u photometry but is otherwise consistent with a Balmer break at ~4000 Å for $z = 0.056$, indicating minimal star formation.

combinations. We use a parametric delayed-τ star formation history (SFH) model, SFH $\propto t \times \exp{-t/\tau}$, where $t = t_{\rm age}$ is a sampled lookback time, constrained to be less than the age of the Universe at SN redshift, and τ is an additional sampled parameter representing the e-folding time. We fit the observed spectral continuum with a tenth-order Chebyshev polynomial and add a sampled parameter (N_0) that normalizes the model to the observed continuum. We finally add two sampled parameters to fit the observed spectral lines: the gas-phase metallicity ($Z_{\rm gas}$) and a dimensionless gas-ionization factor that measures the ratio of hydrogen ionizing photon density to hydrogen density ($U_{\rm gas}$). To compare to commonly used values in the literature, we convert M_F to a stellar mass M_*, $\tau_{v,2}$ and $\tau_{v,1}$ to the total dust attenuation (A_V) in mag, and determine a mass-weighted age (t_m) and present-day SFR from M_F, τ, and $t_{\rm age}$. We refer the reader to A. E. Nugent et al. (2020) and A. E. Nugent et al. (2022) for descriptions on these conversions.

We provide a corner plot of the posteriors in Appendix D, and the SED associated with the median posteriors in Figure 2. The model underestimates the galaxy flux in SDSS-u but is otherwise consistent with the measured photometry, spectral continuum, and spectral line strengths.

The posterior median values are presented in Table 2. We compare them to the properties of archival SN Ibn, SN IIn, and SLSN IIn host galaxies from S. Schulze et al. (2021) in Figure 3. The inferred stellar mass of $\log(M_*/M_\odot) = 7.93^{+0.05}_{-0.03}$ is in the bottom 10% of the 97 SN IIn hosts from S. Schulze et al. (2021), and substantially lower than the value of $\log(M/M_\odot) = 10.2$ reported for SN 2021qqp (an SN IIn with similar photometric properties to SN 2023zkd, as we discuss in Section 4). It is also lower than the majority of reported SN Ibn and SLSN IIn hosts.

Table 2

Median and 1σ Values for the Parameter Posteriors of the `Prospector` Stellar Population Model Fit to the Host-galaxy Photometry

Parameter	Posterior Median and 1σ Range
A_V	$0.35^{+0.07}_{-0.07}$
t_m	$0.98^{+0.15}_{-0.09}$
τ	$0.23^{+0.05}_{-0.03}$
SFR [$M_\odot$ yr^{-1}]	$0.01^{+0.00}_{-0.00}$
$\log(M_*/M_\odot)$	$7.93^{+0.05}_{-0.03}$
$\log(Z_*/Z_\odot)$	$-1.18^{+0.03}_{-0.01}$
$\log(Z_{\rm gas}/Z_\odot)$	$-0.50^{+0.05}_{-0.05}$

We find a best-fit global of 0.01 $M_\odot$ yr^{-1}. Only four hosts in the type IIn sample (PTF09bcl, PTF10dk, PTF10uiz, and iPTF14ajx) exhibit lower values. This can be predominantly explained by the low stellar mass: the specific of $\log_{10}$(sSFR) $= -9.93^{+0.03}_{-0.03}$ is marginally ($<1\sigma$) lower than the means of the SN IIn and SN Ibn samples. The mass of the host is most consistent with the reported distribution of SLSNe IIn, a class of strongly interacting H-rich SNe defined by a brightness at peak of $M_r < -21$ mag (A. Gal-Yam 2012). A sample median of $8.89^{+0.38}_{-0.37}$ $M/M_\odot$ is reported for SLSN IIn hosts versus $9.63^{+0.12}_{-0.12}$ $M/M_\odot$ for SN IIn hosts.

Finally, the inferred metallicity of the host galaxy is 0.3 dex lower than was inferred for 2021qqp using `Prospector` for the same assumed star formation model (D. Hiramatsu et al. 2024b). It is also lower than all values reported for SN IIn host galaxies in L. Galbany et al. (2016), where it was estimated from the O3N2 tracer in spaxel-integrated host spectra (D. Alloin et al. 1979).

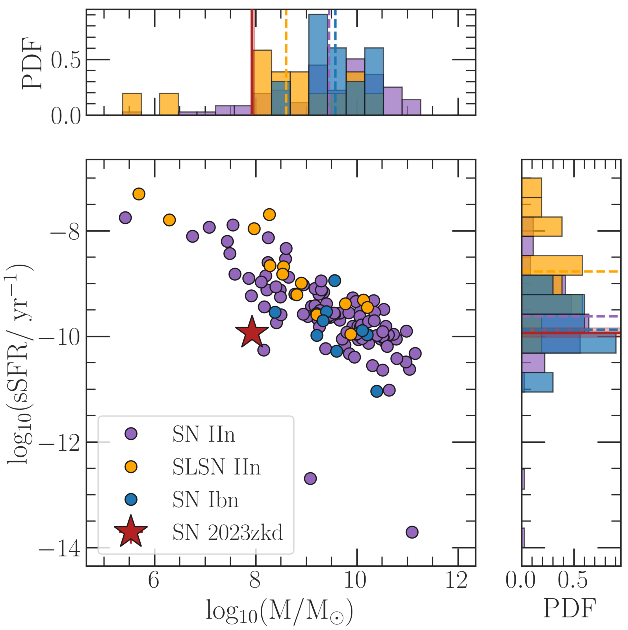

Figure 3. Comparison between the `Prospector`-derived global stellar mass and star formation rate (SFR) for the host of SN 2023zkd (red star) and those reported for the hosts of interaction-powered transients from S. Schulze et al. (2021; classes given in legend). Probability density functions are given at the top and right, with the red line and shaded region corresponding to the median and 1σ uncertainties for the properties of the SN 2023zkd host. Dashed lines indicate the median values for the reference samples. The host-galaxy mass is lower than most comparison objects, but the specific is comparable.

4. Photometric Evolution

We plot the full photometric sequence obtained for SN 2023zkd in Figure 4. The data reveal both long-lived precursor emission and two pronounced post-explosion peaks. Prior to a seasonal gap between MJD 60196 and 60289 (93 days in the observer frame, 88 days in the rest frame), the post-discovery light curve is characterized by a 62 day rise at a median rate of 24 mmag day^{-1}. A peak brightness of $M_r = -18.7$ mag was observed after re-appearing from behind the Sun, followed by a 1.3 magnitude decline over the following 170 days. The event then underwent a dramatic re-brightening period, reaching a secondary maximum of $M_r = -18.4$ mag in ZTF-r 85 days after first minimum. It finally exhibited a secondary dimming period, where it dimmed by by ∼2 mag in 22 days before passing behind the Sun.

The binned pre-discovery photometry is characterized by emission at a median $M_r \approx -15$ mag for ∼1500 days. This may represent roughly persistent emission across this period or multiple long-lived eruptive episodes. The detections ostensibly suggest two distinct periods spanning ∼500 days between MJD 58623 and MJD 59100 (−1601 days to −1127 days) and ∼550 days between MJD 59300 and MJD 59850 (−938 days to −417 days). This secondary interpretation is suggestive of the multiple eruptive mass-loss episodes associated with SNe IIn reported in N. L. Strotjohann et al. (2021), although the maxima of these proposed episodes are not detected in 50 day bins, and additional analysis (described in Appendix A) indicates that the observed variability is statistically insignificant. We therefore define this phase of roughly persistent emission, spanning MJD = 58623 (−1579 days) to MJD = 59873 (−417 days) as highlighted by the brown line in Figure 4, as "Precursor A."

In contrast with the plateau-like emission in Precursor A, the precursor emission in the ∼300 days prior to discovery (in the rest frame) exhibits a persistent brightening accompanied by a monotonic increase in the observed $g - r$ color (the color temperature decreases to ∼8000 K over this period, unlike any period during Precursor A). We define this phase of the pre-explosion emission as "Precursor B" (spanning the yellow line in Figure 4). Precursor B, coupled with a concave-up rise in the post-discovery photometry, is unlike the N. L. Strotjohann et al. (2021) sample of SN IIn precursors. Instead, it is more reminiscent of the inferred observational signatures of runaway binary accretion leading to an SN or merger event (e.g., M. MacLeod et al. 2018a; M. MacLeod & A. Loeb 2020a; S. L. Schrøder et al. 2020; D. Tsuna et al. 2024). We discuss potential progenitors for SN 2023zkd in the context of Precursor B in Section 8.2.

Considering only the photometry prior to discovery ($\leqslant -149.7$ days), the median precursor brightness of $M_r \approx -15.2$ mag and $M_g \approx -15.5$ mag is on the luminous end of the sample consolidated by N. L. Strotjohann et al. (2021). If all photometry prior to the first seasonal gap is included (<0 day), this median increases to $M_r \approx -16.1$ mag.

Precursor B brightens at a median rate of 5 mmag day^{-1} in ZTF-r. This is significantly slower than the median post-discovery rise rate of 24 mmag day^{-1}. If the post-discovery photometry is associated with the SN explosion, we can infer a rise time from discovery to r-band maximum of 60–148 days (with the spread corresponding to the duration of the seasonal gap). This lower limit is ∼40 days longer than the maximum rise time for the SNe IIn with precursors reported in N. L. Strotjohann et al. (2021), but comparable to the inferred rise time of Type IIn SN 2021qqp (D. Hiramatsu et al. 2024b). We caution, however, that the rise times reported in N. L. Strotjohann et al. (2021) are defined as the number of days to r-band peak from 1.086 mag below peak. This timescale will be lower than the period reported for SN 2023zkd, but this pre-peak phase occurs during the seasonal gap for 2023zkd.

Our lower limit on the rise time is also substantially higher than the average for the population of SNe IIn modeled by C. L. Ransome & V. A. Villar (2025), who calculate r-band rise times of 39^{+16}_{-23} days in the rest frame from discovery across their sample (the longest rise of 71.2 days attributed to SN 2020jhs is more consistent). In interaction-dominated SNe, the diffusion timescale of the CSM sets a lower limit on the SN rise. SN 2023zkd's long rise suggests that either the mass of the CSM whose interaction dominates the first peak is higher than most archival events (a median value of $\sim 1.2\,M_\odot$ is inferred for the sample in C. L. Ransome & V. A. Villar 2025), or the early post-discovery photometry is emission from the pre-explosion system and not the SN. As potential evidence for a later explosion date, ZTF-r observations starting at MJD ≈ 60180 (−124 days) indicate an increased brightening rate of ∼35 mmag day^{-1}. An even higher brightening rate of ∼49 mmag day^{-1} is observed in ZTF-g over this period; however, few observations exist at this rate prior to the seasonal gap.

Post-discovery, SN 2023zkd brightens to a maximum of $M_r \leqslant -18.7$ mag before dimming for ∼170 days. Excess flux is still detected from the system at this post-peak minimum. The SN then begins a secondary re-brightening period, and rises to a comparable secondary r-band maximum of $M_r \approx -18.4$ mag 240 days after the first.

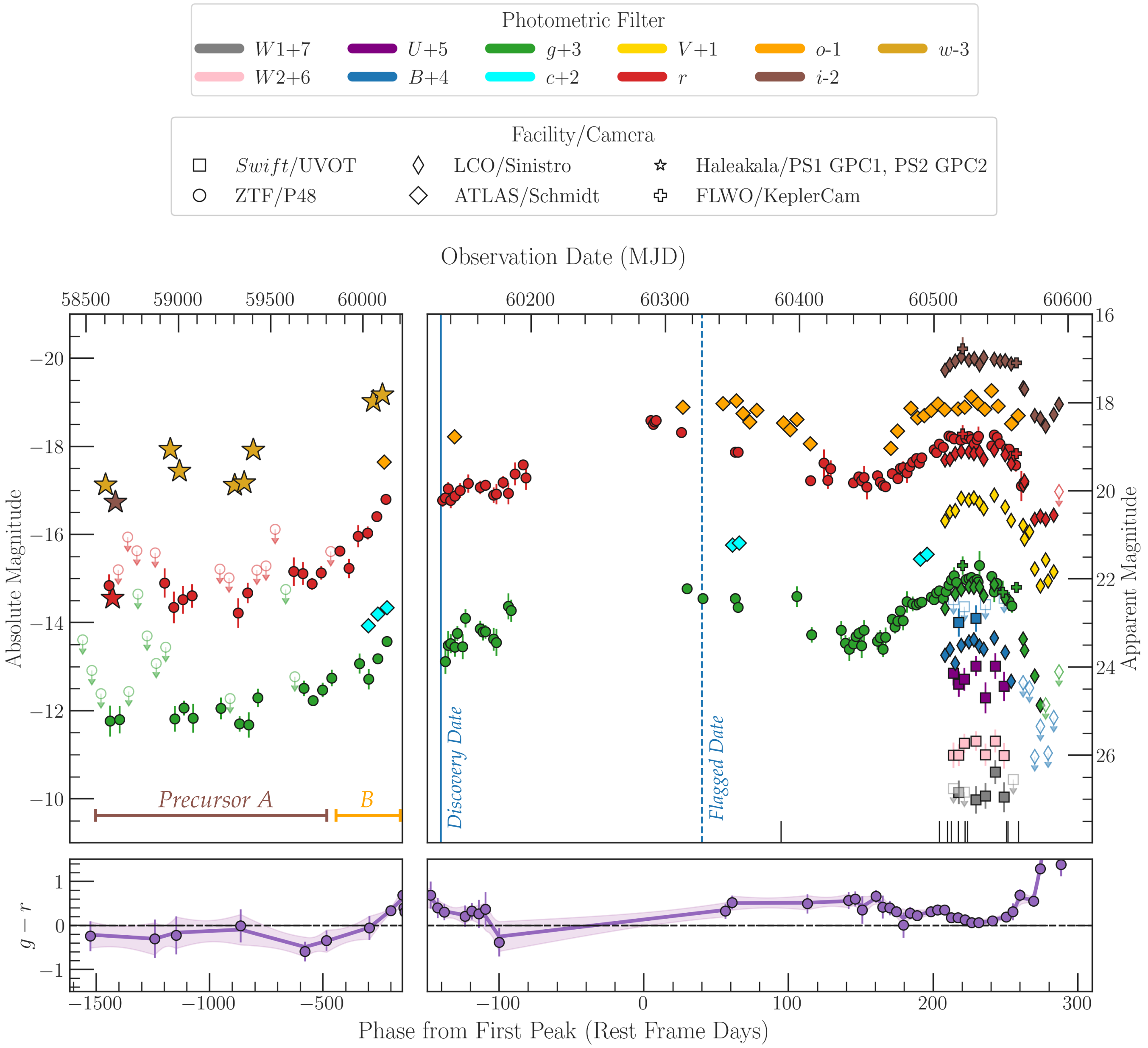

Figure 4. Multiband photometry (top panels) and observed $g-r$ color evolution (bottom panels) for SN 2023zkd. All data have been corrected for Galactic and host extinction ($A_{V,\mathrm{host}} = 0.35$). Photometry prior to discovery at MJD 60132.5 is shown in 50 day bins from ZTF and Pan-STARRS (left); post-discovery photometry is binned in 1 day bins for ZTF photometry, 5 day bins for ATLAS photometry, and unbinned otherwise (right). Filled points indicate detections with $>3\sigma$ significance, and open markers indicate 5σ upper limits. The right panel highlights the post-discovery photometry for the event, with vertical black lines at the bottom indicating the phases of obtained spectra. The blue solid line marks the discovery phase, and the blue dashed line marks the date the transient was flagged by LAISS. The gap during the first maximum is due to Sun constraints. Precursor emission (left panel) is detected to $>3\sigma$ significance in ZTF, ATLAS, and Pan-STARRS1 data up to $\sim$4.5 yr before the first ZTF-r-band maximum, and $\sim$4 yr before SN discovery. The $g-r$ color is estimated with weighted averages of photometry in 100 day bins pre-discovery and 5 day bins post-discovery. The purple line and shaded region correspond to the mean and 1σ standard deviation, respectively, of a univariate spline fit to the binned measurements.

(The data used to create this figure are available in the online article.)

Following the secondary peak, SN 2023zkd dims at a rate of 48 mmag day^{-1} in ZTF-r, six times faster than the decline rate during the first peak. This behavior is emblematic of the ejecta reaching the outer edge of the CSM, leading to a rapid drop in energy input from SN–CSM interaction. Similar behavior has been observed in other SNe IIn (e.g., 1994W; L. Dessart et al. 2009), and may also be suggestive of CSM asymmetry (see T. J. Moriya et al. 2014).

Figure 4 also shows the $g-r$ color of the transient in ZTF filters in 100 day bins pre-discovery and 5 day bins thereafter. The color of Precursor A is consistent with $g-r=0$, whereas the transient reddens during Precursor B and reaches a maximum of 0.7 ± 0.3 at the epoch of discovery. This is followed by a decrease from discovery to the start of the first seasonal gap, followed by a more gradual blueward evolution in the rise to secondary maximum at $g-r \approx 0$. SN 2023zkd's final dimming period is associated with a substantial increase in $g-r$, with the final observations having $g-r \sim 1$ on MJD $\approx$ 60640 (+331 days). When the cold-dense shell formed in an SN interaction reaches the edge of the CSM, a flood of

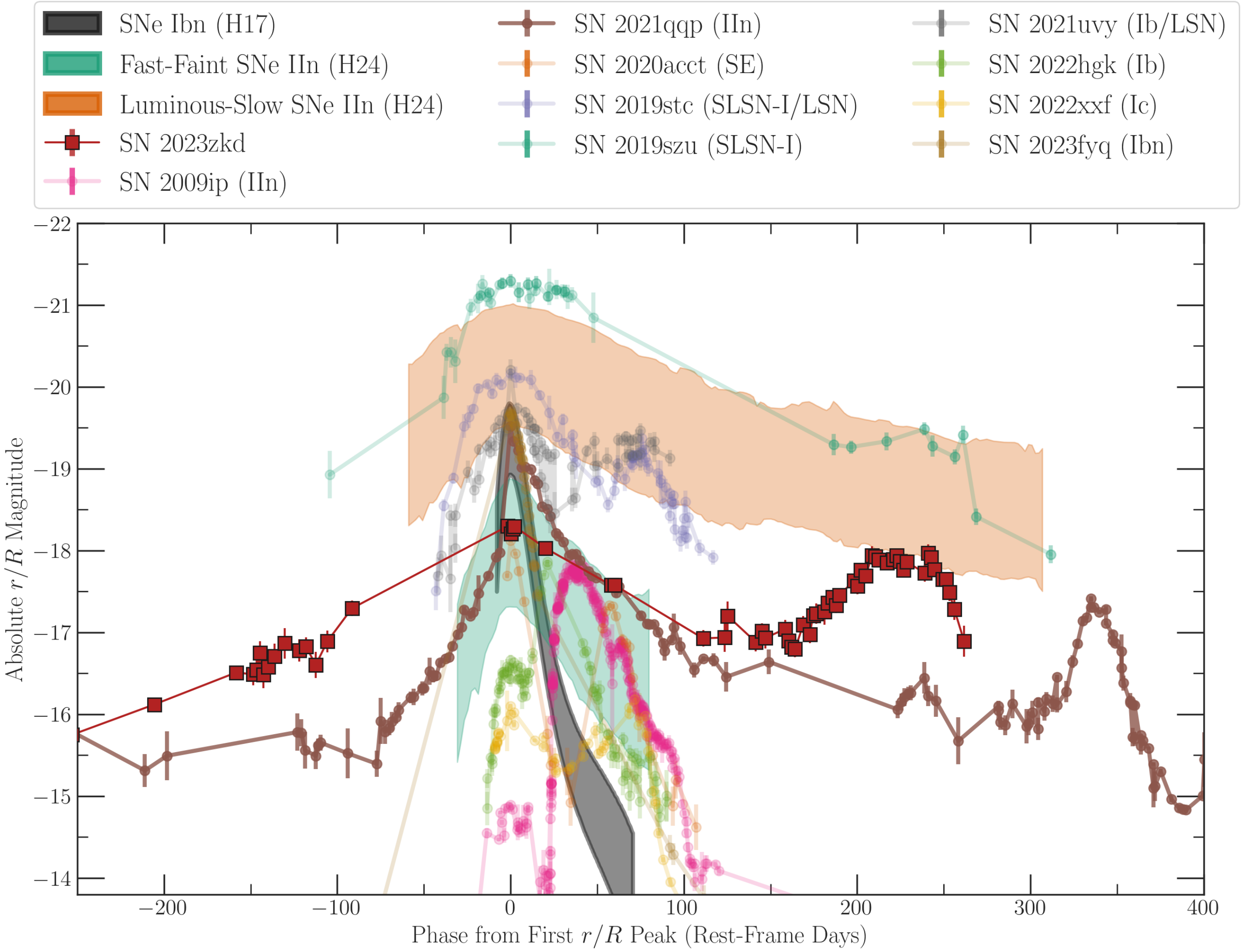

Figure 5. Comparison between the photometric evolution of SN 2023zkd in ZTF-r and other interacting SNe, including the double-peaked sample from C. R. Angus et al. (2024; S. Gomez et al. 2021; C. P. Gutiérrez et al. 2021; H. Kuncarayakti et al. 2023; A. Aamer et al. 2024; K. K. Das et al. 2024; T. Kangas et al. 2024; Y. Sharma et al. 2024) and 2021qqp (the closest photometric analog to 2023zkd, shown in brown; D. Hiramatsu et al. 2024b). The 95% range (1.96σ) for the SN Ibn template from G. Hosseinzadeh et al. (2017) is shown as the black shaded region, as is done for the "fast-faint" and "luminous-slow" SN IIn templates from D. Hiramatsu et al. (2024a) shown as green and orange shaded regions, respectively. SN 2023zkd evolves more slowly than expected for an SN Ibn and is more consistent with the "fast-faint" SN IIn template, reinforcing its type IIn classification in this work. Transient names and classes are given in the legend (the alternative classification of "luminous SN," LSN, is suggested by S. Gomez et al. 2022 for the double-peaked SN 2019stc).

suppressed redward-scattered photons can be released from behind the interaction front, potentially explaining the rapid reddening (N. Smith 2017b). Prompt dust formation may also be possible (C. Gall et al. 2014); late-time NIR follow-up observations would be valuable for confirming this scenario.

Double-peaked SNe IIn are relatively rare in the literature. Of a sample of 119 SNe IIn analyzed by C. L. Ransome & V. A. Villar (2025), five featured prominent re-brightening phases. Among other SN classes, double-peaked events span the diversity of stripped-envelope explosions: a sample of nine presented in C. R. Angus et al. (2024) include SNe Ib/c and SLSNe-I, with each suggesting ongoing SN interaction with material stripped from the progenitor prior to explosion. We plot the photometric evolution of SN 2023zkd in ZTF-r in Figure 5 along with the double-peaked sample from C. R. Angus et al. (2024). To more directly compare events, we exclude SNe where the first peak is not temporally resolved in r and does not correct 2023zkd's light curve for host extinction.

The photometric peaks of SN 2023zkd are separated by 223.5 days (236 days in the observer frame), 104.5 days (in the rest frame) higher than the event with the widest separation for the sample reported by C. R. Angus et al. (2024; 119 days for SN 2023aew, an SN IIb/Ic hybrid with no spectroscopic signatures of CSM interaction; T. Kangas et al. 2024; Y. Sharma et al. 2024). Of the events in this reference sample, only SN 2022xxf also features a secondary peak with maximum brightness within 1 mag of the first peak.

In Figure 5, we also show r-band templates for "fast-faint" and "luminous-slow" SNe IIn from D. Hiramatsu et al. (2024a; green and orange shaded regions, respectively) and for SNe Ibn (gray shaded region) from G. Hosseinzadeh et al. (2017). SN 2023zkd's evolution across both peaks is significantly slower than the SN Ibn template. It is most closely matched to the fast-faint SN IIn population (if the pre-discovery detections are not considered). Considering the full evolution across both peaks, the rise and decline rates are well matched to the luminous-slow population of SNe IIn (although the observed first peak is ∼2 mag fainter than the typical luminous-slow SN IIn peak). These comparisons further reinforce SN 2023zkd's classification as an SN IIn.

The missing photometry for the event, coupled with the host mass more closely matched to SLSN IIn hosts, raises the possibility of a luminous unobserved peak. Given the similar luminosity of the observed first peak to the SNe IIn from D. Hiramatsu et al. (2024a), we can place loose constraints on the behavior of the event during the seasonal gap. For the events in the sample, an SN IIn with a decline time to 20% r-band flux of ∼150 days exhibits a rise time from 20% flux before peak of ∼ 40 days, versus the ∼160 days that we measure for SN 2023zkd (the phase of pre-peak 20% flux is comparable to the discovery phase). This suggests that either the intrinsic event peak occurred during the seasonal gap, or the rise time of SN 2023zkd is atypically long among SNe IIn.

If we shift the fast-faint and slow-luminous templates to the phase of the last 2023zkd observation prior to the seasonal gap (to mimic an unobserved SN IIn peak), the observed post-peak luminosity falls squarely between these two populations. This suggests an intrinsic peak r-band brightness brighter than the faint population but fainter than the bright population (-18.3 mag $< M_r < -20.2$ mag). Linear fits extrapolated from the final pre-gap observations and the earliest post-gap observations intersect at -18.5 mag $< M_r < -19$ mag, or -18.9 mag $< M_r < -19.4$ mag after correcting for host extinction. This is substantially lower than required for an SLSN IIn ($M_{r/R} < -21$ mag). If a much higher brightening rate began during the seasonal gap, a rise time associated with SLSNe IIn to $M_r \approx -21$ mag would require a decline rate of $\geqslant 60$ mmag day^{-1} to be observed at $M_r = -18.7$ mag after re-appearing behind the Sun, three times higher than the decline rate observed for the SLSN IIn PTF09uy (A. Nyholm et al. 2020). We conclude that an unobserved peak much more luminous than the observed maximum is unlikely.

Qualitatively, the photometric evolution of SN 2023zkd appears remarkably similar to that of the strongly interacting and double-peaked SN IIn 2021qqp (D. Hiramatsu et al. 2024b, also shown in Figure 5). A long-lived precursor was also observed in SN 2021qqp at $M_r \approx -14$ mag and lasting >300 days in the frame of the SN, with marginal ($\sim 3\sigma$) detections reported ∼2500 days prior to first r-band maximum. The separation between observed r-band peaks in SN 2023zkd is ∼112 days smaller than the separation for SN 2021qqp (though shifting the phase of 2023zkd to account for an unobserved peak brings the difference to ∼50 days).

Though both events exhibited increases in brightening rate prior to first r-band maximum, the observed rise rates are substantially different. The fastest rise observed for SN 2023zkd of ∼50 mmag day^{-1} is still substantially slower than the 70 mmag day^{-1} associated with the explosion first light for SN 2021qqp. The lack of a clear distinction between precursor and SN provides additional evidence that the first emission from the SN 2023zkd ejecta occurred just prior to or during the first seasonal gap. In this case, all post-discovery observations prior to MJD 60183-60188 would be associated with the SN precursor.

5. Spectroscopic Evolution

5.1. Optical Spectra

We plot our full spectroscopic sequence for SN 2023zkd, spanning 168 days, in Figure 6. The spectra are dominated by multicomponent Balmer and He I emission features that evolve slowly from +90 days to +258 days. We plot the emission lines of Hα, Hβ, He I λ5876, and He I λ7065 in Figure 7. These spectral profiles are highly complex and grow increasingly asymmetric throughout the second peak, with prominent red wings most likely the product of electron scattering from the ionized CSM (similar to e.g., SN 2013L; F. Taddia et al. 2020; and SN 2021adxl; S. J. Brennan et al. 2024b). The Hα profiles at all epochs show a narrow core and a wide base (with the base spanning ∼6000 km s^{-1}).

SN 2023zkd is unique among SNe IIn for its persistent He I emission features. The Magellan/LDSS-3 spectrum obtained at +90 days exhibits double-peaked He I profiles at λ5876, λ7065 (Figure 7), and λ5016. In these profiles, the minimum between the peaks is consistent with the rest-frame wavelength for all lines. In the second spectrum at +202 days (during the second brightening phase), the He I features at 5876 and 7065 Å exhibit a more flat-topped profile. The double-peaked profiles then re-appear by +212 days, and the redward peak fades until only a single emission feature blueward of the rest wavelength dominates the He I profiles through the final spectrum at +258 days.

The double-peaked He I profiles at +90d are uncommon, even among SNe Ibn (G. Hosseinzadeh et al. 2017). These could alternatively be two He I features in emission and symmetric about the rest wavelength, or absorption from material with negligible velocity relative to the observer superimposed atop a broad emission feature. A detailed analysis of the velocity components in Section 5.3 favors the former interpretation.

A narrow P-Cygni feature also appears at ∼4700 Å in the NTT/EFOSC2 spectrum at +202 days. It strengthened by the phase of the second NOT/ALFOSC spectrum at +212 days, then decreases again but persists through the final spectrum at +258 days. Given the similar evolution of a likely He II profile near λ8237 (potentially blended with Mg II), we associate this with He II λ4686. Additional features are tentatively identified as He II at 5977 Å, 6004 Å, and 6037 Å.

Late-time He II features are extremely rare among interacting SNe (He II features from UV photons mediating the SN shock are typically observed only in the few days following explosion; A. Gangopadhyay et al. 2020, 2022; N. N. Chugai & V. P. Utrobin 2023; W. V. Jacobson-Galán et al. 2024; T. Pessi et al. 2024). The collision between the SN ejecta and a secondary CSM overdensity provides a natural explanation for renewed ionizing photons at these phases (as has been observed during the first peak of SN 2020acct; C. R. Angus et al. 2024; and in the peculiar type Ib SN 2006jc; N. Smith et al. 2008). The P-Cygni profile of He II λ4686 has its absorption trough at ∼1000 km s^{-1} in all spectra, similar to the velocity of the fast CSM we derive in Section 5.2.

2023zkd also shows a forest of additional narrow emission components in all spectra contemporaneous with the second light curve peak (>202 days). The majority of these features are Fe II, as shown by the orange lines in Figure 8 (we adopt the Fe II line list reported by N. N. Chugai et al. 2004). Additional blends near 7850 and 8200 Å may be Mg II, although additional unknown elements are suggested by the blends near 8000 and 8400 Å. An emission line observed from +209 to +250 days is most easily explained as N III at 4634 and 4641 Å, as seen in the SN IIn 1998S (I. Shivvers et al. 2015).

5.2. Optical Spectral Line Fitting

To better characterize the spectroscopic evolution of SN 2023zkd in the optical, we model the spectral features of Hα,

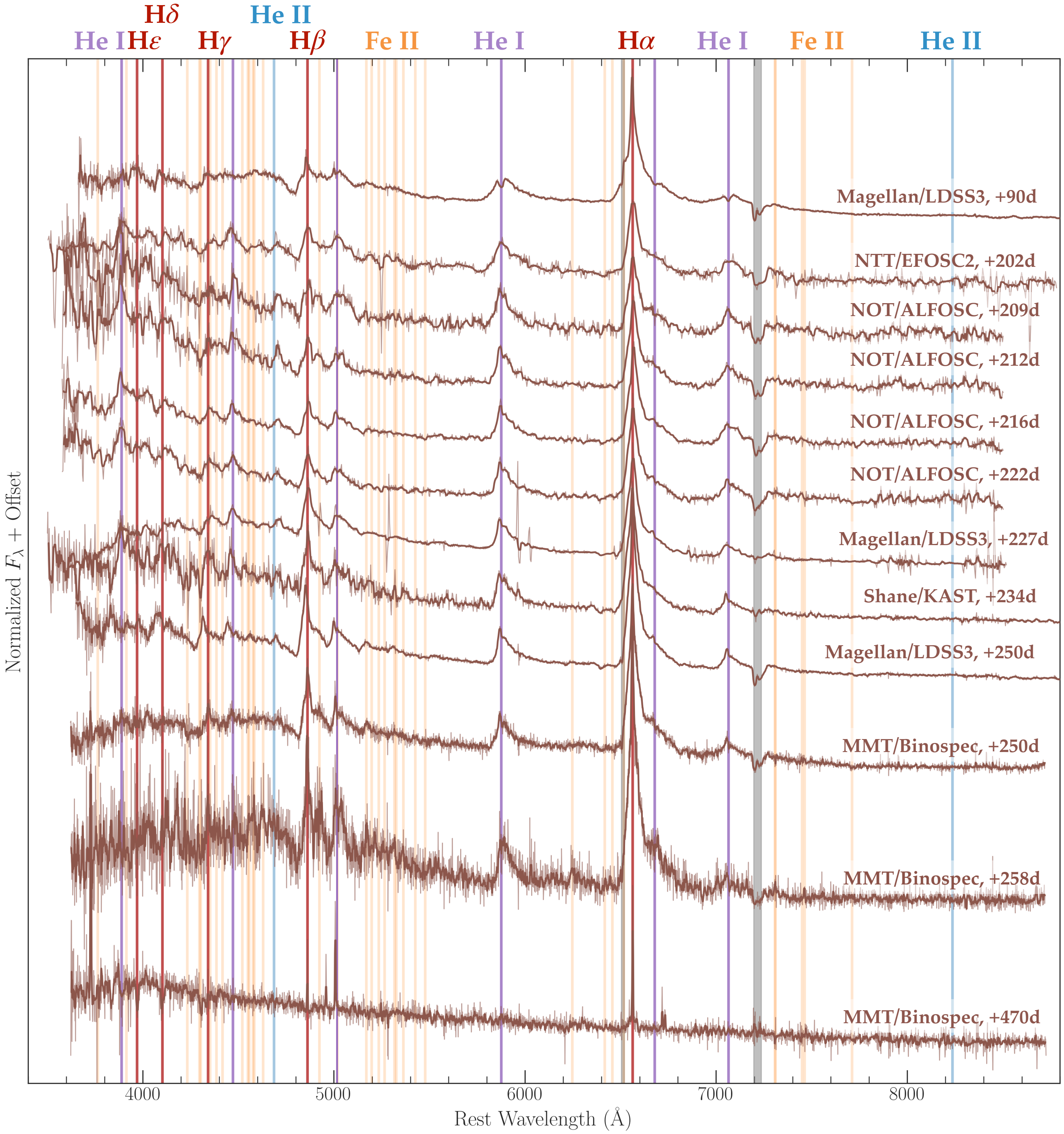

Figure 6. Optical spectroscopic sequence obtained for SN 2023zkd. Spectra are colored by spectrograph and relevant lines are annotated. Spectra have been normalized within 5500–7500 Å and corrected for Galactic and host extinction. Multicomponent and asymmetric Balmer and He I features are visible throughout its evolution, while a forest of Fe II lines appears alongside candidate He II features during the second light curve peak.

Hβ, and He I at λ5876 (given its strength relative to the other He I lines). For each observed feature, we fit a combination of Gaussian and Lorentzian profiles. Each component is parameterized by the amplitude, the center wavelength in the rest frame, and the profile spread (σ, the standard deviation of the Gaussian profile, and the FWHM for a Lorentzian profile).

We first fit a low-order polynomial to the spectral region of interest (masking the emission profile) and subtract it from the line region. We then visually determine the line width for fitting. We define uniform priors for each parameter and compare the wavelength and flux values (λ, f) with associated flux uncertainties σ_f to the combined model fit $M(\lambda)$ using a standard log-likelihood under assumptions of Gaussianity:

$$\ln \mathcal{L} \propto -\frac{1}{2}\sum\left[\frac{(f - M(\lambda))^2}{\sigma_f^2} + \ln(\sigma_f^2)\right]. \quad (1)$$

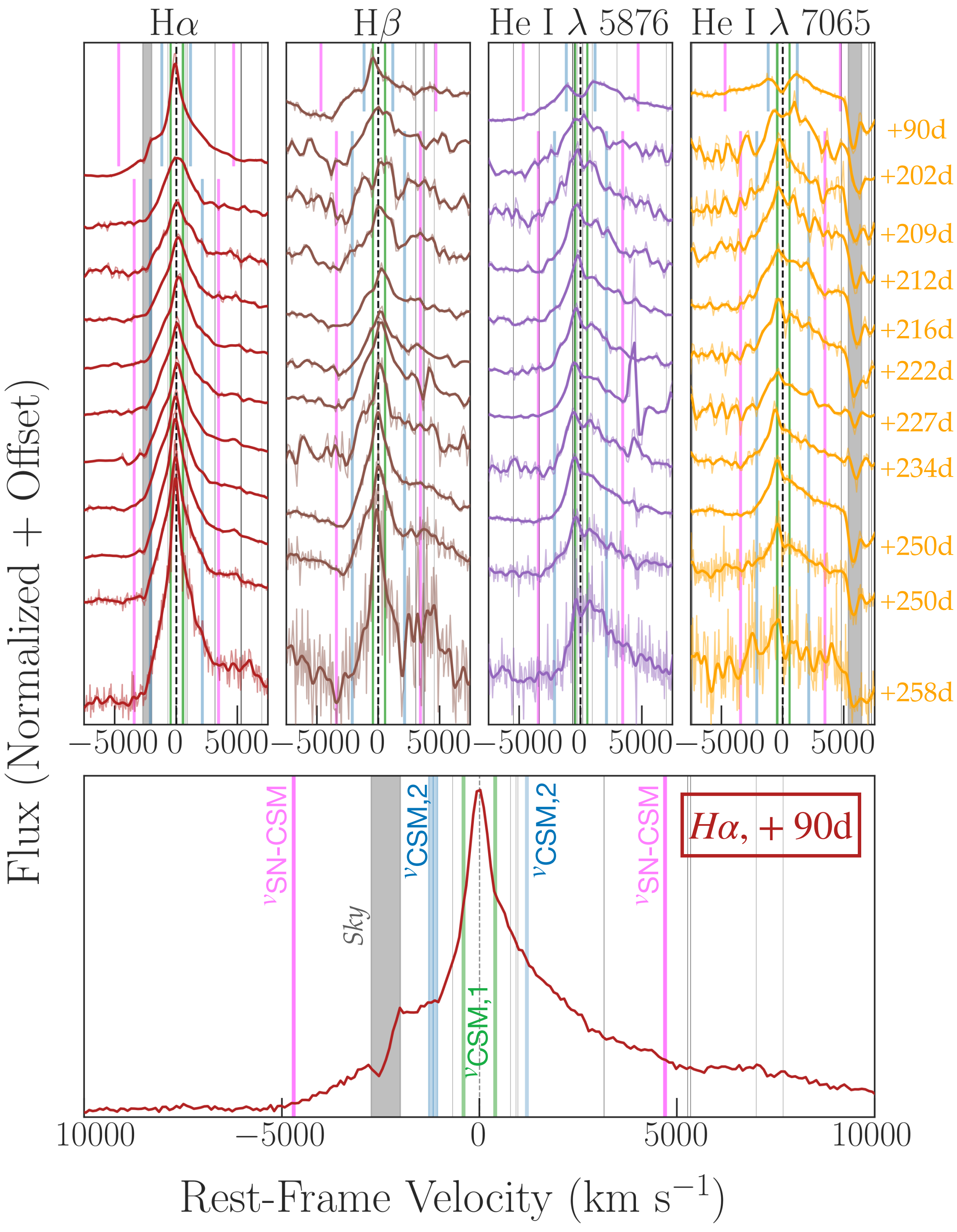

Figure 7. Top panels: line profiles for Hα, Hβ, He I λ5876, and He I λ7065 textcolorbluefrom +90 days to +258 days. All spectra have been smoothed to a fixed resolution of $R = 750$. Vertical lines indicate the range of the CSM (blue) and SN–CSM interaction shell velocities (magenta) derived in Section 5.2; for clarity, only the mean velocities are shown for spectra obtained during the second light curve peak (+202 days onward). Additional emission near the rest wavelength is suggestive of a secondary CSM component at ±400 km s^{-1} (green lines), and the +90 days spectrum shows two He I emission components at the SN–CSM shell velocity. The low-velocity components are further suggested by the GNIRS spectrum in Section 5.6. The broad base observed in the +90 day spectrum persists throughout the final spectrum at +258 days. Bottom panel: Hα profile at +90 days, with the same velocity components as above. The unresolved blue shoulder is consistent with a velocity of ∼1170 km s^{-1} (shaded magenta region) as measured from the FWHM of the Lorentzian profile fit to the emission (Section 5.4), but a narrower core can also be seen.

For each spectral feature, we initialize 64 walkers at randomized positions about an initial guess for the parameter vector with noise scale of 10^{-4}. We then run a Markov Chain Monte Carlo simulation using the `emcee` package for 10,000 total steps and a burn-in period of 1000 steps, with the log-likelihood as our update criterion. We verify convergence by examining the parameter posteriors with the `corner` package while ensuring that the final fits all have reduced $\chi^2 \approx 1$. We

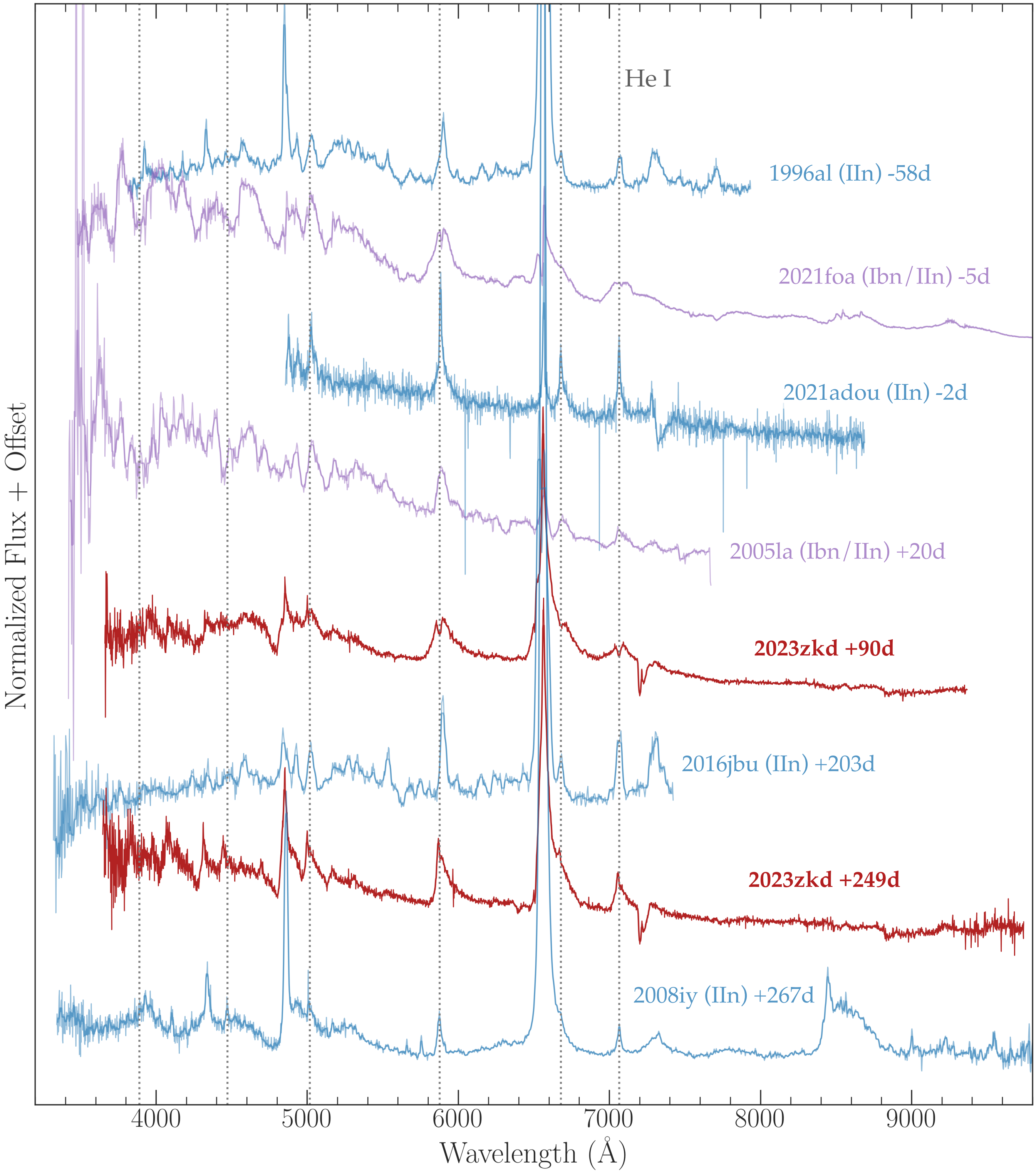

Figure 8. Comparison of 2023zkd spectra during the primary and secondary peaks to strongly interacting SNe from literature with prominent H and He emission features. All spectra have only been corrected for Galactic extinction. Comparison spectra are colored by spectroscopic class, and vertical dashed lines indicate strong He I lines. The emission profiles for SN 2023zkd are highly asymmetric, with narrow cores and a broad redward tail not observed in the features of other SNe IIn but potentially similar to the emission from the SN Ibn/IIn 2021foa.

show an example fit to our Hα, Hβ, and He I λ5876 profiles at MJD = 60519 (+216 days) in Figure 9.

We fit two profiles per line for each optical spectrum of SN 2023zkd, and integrate the combined fit from each chain to obtain the total line flux with associated uncertainties for Hα, Hβ, and He I λ5876. Due to the strong asymmetries observed in the profiles, we find our best results by adopting one narrow Lorentzian component (if resolved) and one broad Gaussian component to the emission for Hα and Hβ, and two Gaussian components for He I λ5876. For Hβ, we additionally fit a third

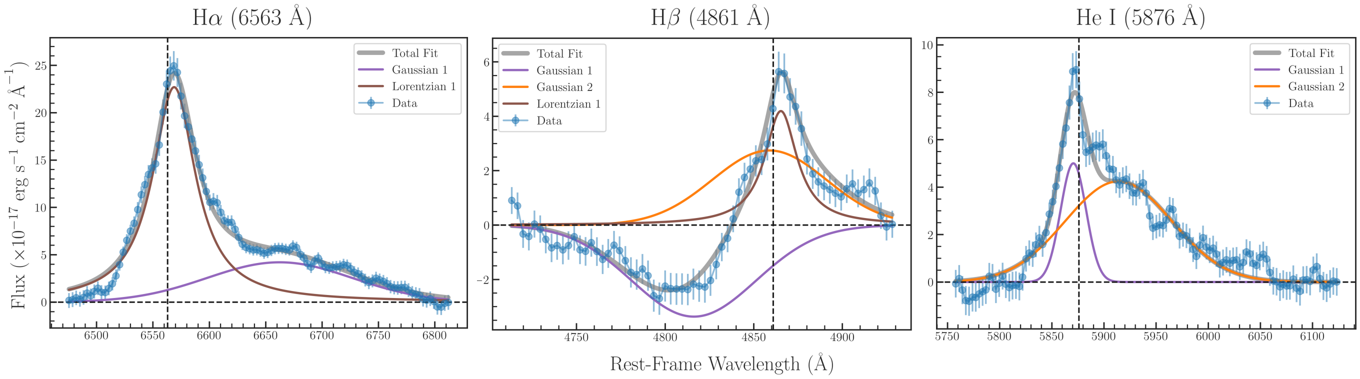

Figure 9. Line fits to the Hα (left panel), Hβ (middle panel), and He I λ5876 (right panel) profiles of the NOT/ALFOSC spectrum obtained on MJD 60519 (+216.3 days). Data are shown in blue, and the combined model for each profile is shown as a shaded gray line.

Gaussian profile in absorption to the trough of the P-Cygni profile. We caution that the red wing of Hα is completely blended with He I at 6678 Å, which contributes additional flux to the profile. This can be seen as an absorption as this wavelength transitions to emission in coevolution with He I λ7065 and λ5876.

We measure the FWHM of the Lorentzian component for Hα in velocity space, which we associate with the CSM velocity; we measure the minimum of the P-Cygni trough for Hβ in velocity space and associate it with the velocity of the SN–CSM interaction shell. The minimum of the Hβ trough decreases from $4,698^{+190}_{-150}$ km s^{-1} at MJD ≈ 60386 (+90 days) to $2,797^{+700}_{-700}$ km s^{-1} at MJD ≈ 60504 (+202 days), where it remains roughly constant through the second photometric peak (the highest measured value during the second peak is $3,622^{+670}_{-480}$ km s^{-1} at MJD ≈ 60530, or +227 days). The FWHM of the narrow Lorentzian component increases from $1,176^{+110}_{-110}$ km^{-1} at MJD ≈ 60386 (+90 days) to a maximum of $2,228^{+92}_{-92}$ km s^{-1} at MJD ≈ 60525 (+222 days), nearing to the SN–CSM shell velocity.[37] At the decline of the secondary peak, the measured CSM velocity marginally decreases to $2,032^{+86}_{-86}$ km s^{-1} (MJD ≈ 60555, +250 days) and then to $1,824^{+46}_{-46}$ km s^{-1} (MJD ≈ 60563, +258 days).

The evolution in the CSM velocity mimics that of SN 2021qqp (whose CSM was constrained to mean velocities of 1300 km s^{-1} during the first peak and 2500 km s^{-1} during the second; D. Hiramatsu et al. 2024b). This similarly suggests that the CSM associated with the second photometric peak was either accelerated or ejected at higher velocities (though our measured SN–CSM velocity is substantially lower than their values of 8500 and 5600 km s^{-1} during the first and second peak, respectively). All measured CSM velocities are also on the highest end of both the SN IIn samples associated with eruptive precursors (N. L. Strotjohann et al. 2021) and of the broader SN IIn population (C. L. Ransome & V. A. Villar 2025).

5.3. Evidence for High- and Low-velocity CSM Components

Having identified the dominant components in the emission lines of Hα, Hβ, He I λ5876, and He I λ7065, we now investigate their unusual structure.

In addition to the CSM and SN–CSM components fit by our spectral modeling, each profile exhibits additional and marginally resolved features that cannot be easily attributed to other transition lines (Figure 7). The blue shoulder and the primary Hα emission at +90 days both point to an unshocked CSM velocity of ∼1200 km s^{-1}. To probe the symmetry and composition of this CSM, we have added vertical lines to search for symmetric velocity components associated with the SN–CSM interaction shell (magenta) and the CSM (blue).

We find, surprisingly, that the CSM velocities align precisely with the peaks of the He I profiles at 5876 Å and 7065 Å at +90 days. These velocities are also consistent with blueward and redward dips in the He I λ5876 and the He I λ5876 profiles at +202d, and peaks in the Hβ profile at multiple epochs during the second light curve peak.

Furthermore, we find evidence for a secondary, lower-velocity CSM component. The peaks in the He I λ5876 profile starting during the second peak at +202 days are more consistent with velocities of ±400 km s^{-1}. These lower velocities are also suggested by a shift in the emission peaks of Hβ toward the approaching component. While the peaks in the Hα and Hβ profiles at +90d are Lorentzian and suggestive of Thomson scattering through a high-density plasma, the double-peaked He I profiles at this phase instead appear Doppler broadened. This strongly suggests two distinct emitting regions. Finally, we observe that, when the two He I profiles transition to a single dominant emission feature from +202 days onward (along with a broader rightward feature), the peak of the emission lies occurs near −400 km s^{-1}. The limited resolution of our spectra (∼250 km s^{-1}) prevents us from precisely constraining the velocity of the slow-moving material, but the components are persistent and distinct from the higher-velocity CSM at all phases after +202 days.

These features suggest two distinct and axisymmetric CSM components: one lower-velocity component where narrow H emission is observed at +90 days, and another higher-velocity component in which the peak of the He emission occurs during the second photometric peak. The enhancement of the blue emission component during the second light curve peak is probably the result of electron scattering, with redward photons behind the interaction shell preferentially scattered out of sight.

Fast-moving and low-moving CSM components have been identified in multiple SNe IIn. This includes 2016jbu, where a lower-velocity component at ∼250 km s^{-1} was attributed to a stellar wind in the terminal progenitor; and ASASSN-15ua,

---

[37] We caution that the resolution of the NOT spectrum (∼400 km s^{-1}) introduces additional uncertainty to the measured CSM velocity at +222 days.

2013L, and 2010jl, where a spectral component near $\sim 100\,\mathrm{km\,s^{-1}}$ was reported for each event (C. Fransson et al. 2014; C. Gall et al. 2014; C. Huang & R. A. Chevalier 2018; F. Taddia et al. 2020; D. Dickinson et al. 2024). In 2010jl, the narrow component was also suggested to originate in material distinct from the scattering medium (C. Huang & R. A. Chevalier 2018).

We favor a similar interpretation for the narrow H components at +90 days. In this scenario, emission from low-velocity material scatters through the more extended, faster-moving material dominating the photometric emission, leading to the observed emission at each of the velocities through the second brightening phase. While our spectral resolution at optical wavelengths is comparable to the inferred low velocities ($\sim 400\,\mathrm{km\,s^{-1}}$), this view is further supported by lower-intensity He I profiles in our higher-resolution NIR spectrum. We discuss these data in Section 5.6.

5.4. Spectroscopic Comparison to Other Interaction-powered SNe and Classification as a Type IIn Supernova

We next consider the ambiguous spectroscopic classification of SN 2023zkd. The event was publicly classified as an SN Ibn due to its narrow H and He profiles, but He has been also observed in the spectra of some SNe IIn. Notable examples of these He-rich SNe IIn include SN 2016jbu (an SN IIn that also exhibited precursor emission and a post-explosion re-brightening event 250 days after first peak; S. J. Brennan et al. 2022); and SN 1996al (a transitional object that first appeared as a spectroscopically normal SN II, then later evolved to show narrow Hα features reflective of an SN IIn; S. Benetti et al. 2016).

To understand the 2023zkd system within the broader context of interacting SNe, we query WiSeREP for the spectra of other SNe IIn with prominent He features at similar phases to 2023zkd. We find similar spectra for SNe 2016jbu (S. J. Brennan et al. 2022) and 1996al (S. Benetti et al. 2016), along with 2008iy (which showed an unprecedented rise time of ∼400 days, though photometric coverage of the event was poor; A. A. Miller et al. 2010) and 2021adou (W. Jacobson-Galán et al. 2021).[38] We also compare the spectra of the SNe Ibn/IIn 2021foa (D. Farias et al. 2024; A. Gangopadhyay et al. 2024) and 2005la (A. Pastorello et al. 2008a).

We plot the most similar spectra for these strongly interacting SNe in Figure 8. We do not observe a red wing in the Balmer features of any of our comparison SNe IIn (whose spectra span −58 to +203 days relative to peak), suggesting more extreme electron scattering in 2023zkd. Interestingly, the earliest spectrum of 2021foa (−5 days from *r*-band maximum) shows similar double-peaked emission profiles of He I $\lambda 7065$ and He I $\lambda 5876$, and with some line profile asymmetries. D. Farias et al. (2024) interpreted the double-peaked He I emission as a blend with the Na I doublet at $\lambda 5876$, and the secondary component at $\lambda 7065$ to the presence of an unknown element.

We repeat the process described in Section 5.2 to measure the integrated line flux of Hα and He I $\lambda 5876$ for the comparison SNe in Figure 8. We consider only optical spectra 50–365 days after *r*-band maximum (which we have either estimated photometrically or taken from the text of the cited publications, if available). The same combination of line fitting components was adopted as in 2023zkd, with the exception of SN 1996al: the prominent blue shoulder of its Hα profile at later phases required an additional Gaussian emission profile to accurately reconstruct its total flux.

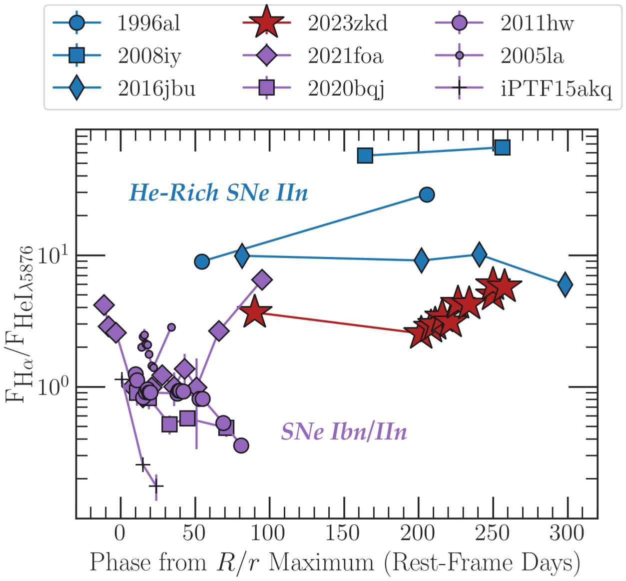

Figure 10. $F_{\mathrm{H}\alpha}/F_{\mathrm{HeI}\lambda5876}$ line ratios for SN 2023zkd (red), He-rich SNe IIn between 50 days and 1 yr from R/r-band maximum (blue), and for transitional SNe IIn/Ibn (purple; from D. Farias et al. 2024). SN 2023zkd lies at the boundary between spectroscopically normal SNe IIn and transitional SNe Ibn/IIn events.

We show the resulting $F_{\mathrm{H}\alpha}/F_{\mathrm{HeI}\,\lambda5876}$ flux ratios for the sample in Figure 10, along with the values calculated by D. Farias et al. (2024) for the transitional SNe Ibn/IIn 2020bqj (E. C. Kool et al. 2021), 2011hw (N. Smith et al. 2012a), 2005la (A. Pastorello et al. 2008b), and iPTF15akq (G. Hosseinzadeh et al. 2017). The flux ratio for SN 2023zkd is systematically lower than is observed in all comparison He-rich SNe IIn. SN 2016jbu has the lowest average $F_{\mathrm{H}\alpha}/F_{\mathrm{HeI}\,\lambda5876}$ ratio among SNe IIn, from 10.2 at +241 days to 6.0 at +299 days relative to *r*-band maximum, and only reaches a similar value to 2023zkd at one epoch.

In addition, we observe a gradual but monotonic increase in the ratio over the second light curve peak. The value increases from 2.2 in the second spectrum at +202 days, to 5.8–6.0 in the final two spectra at +250 days and +258 days. In comparison, the line ratios for the "flip-flopping" SN 2021foa reach those of 2023zkd's later epochs during its "SN IIn" phases, from 4.2 at −11 days to 6.5 at +95 days. The transitional SN IIn/Ibn sample has a mean line flux ratio of $F_{\mathrm{H}\alpha}/F_{\mathrm{HeI}\lambda5876} \approx 1$ (see Figure 12 of D. Farias et al. 2024), suggesting that the spectral evolution of SN 2023zkd is still more akin to an He-rich SN IIn than a transitional SN Ibn (though we note that the dearth of late-time spectroscopy for these populations limits a more comprehensive analysis).

SN 2023zkd has the lowest $\mathrm{F}_{\mathrm{H}\alpha}/\mathrm{F}_{\mathrm{HeI}\lambda5876}$ ratio of the SNe IIn analyzed. Blending of the Hα profile with He I at 6678 Å likely leads to an overestimation of the integrated flux we report, so the intrinsic $F_{\mathrm{H}\alpha}/F_{\mathrm{HeI}\lambda5876}$ ratio for SN 2023zkd may fall even closer to the set of "transitional" SN Ibn/IIn events. While the photometric evolution and host-galaxy

---

[38] Despite photometric similarities, only marginal He emission was observed in the SN IIn 2021qqp (D. Hiramatsu et al. 2024b).

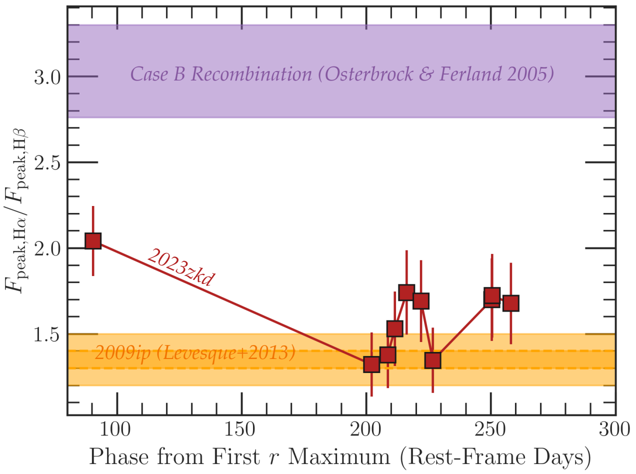

Figure 11. $F_{\rm peak,H\alpha}/F_{\rm peak,H\beta}$ values for SN 2023zkd across the spectral sequence (red squares), compared to the range expected for Case B recombination (purple shaded region) and those reported for SN 2009ip during its 2012-B event (orange dashed lines, with shaded regions corresponding to 1σ uncertainties; E. M. Levesque et al. 2014).

properties of 2023zkd strongly suggest a type IIn, these line ratios indicate an explosion filling the gap between SNe Ibn and He-rich SNe IIn.

5.5. Evolution of the Balmer Decrement

Next, we consider the evolution of the Hα and Hβ line strengths and its implications for the circumstellar emission and geometry. The Balmer decrement is the ratio between the intensities of these profiles. Balmer decrements have been well constrained for photoionized nebulae that absorb Lyα photons but are optically thin to Hα. Collisionally excited material produces systematically lower Balmer decrements that also correlate with the properties of the emitting region (S. A. Drake & R. K. Ulrich 1980). This makes the measurement a valuable (and underutilized in SN science) probe of the ionization physics of both high-density and low-density material.

Because of the strong blending observed in Hα (both with multiple-velocity components and with He I at 6678 Å), we compute the Balmer decrement at each spectral epoch from the maximum flux value of each profile ($F_{\rm peak,H\alpha}$ and $F_{\rm peak,H\beta}$). The peak flux is expected to trace the low-velocity component of the CSM across the spectral sequence more reliably than the integrated flux, particularly when multiple-velocity components are blended (E. M. Levesque et al. 2014).

We plot the resulting $F_{\rm peak,H\alpha}/F_{\rm peak,H\beta}$ ratio in Figure 11. We also compare our results to the Balmer decrement expected for Case B recombination (D. E. Osterbrock & G. J. Ferland 2006) across a broad range of gas temperatures (2500–20,000 K) in purple, and to those measured in the luminous "2012-B" event from the LBV SN 2009ip (orange; E. M. Levesque et al. 2014).

We measure a low Balmer decrement spanning the full spectral sequence of SN 2023zkd, from a value of 2.0 ± 0.2 at +90 days and spanning a consistently low 1.3–1.8 across the second r-band peak. We measure a minimum value of 1.3 ± 0.2 from the NTT/EFOSC2 spectrum at +202 days).

We also observe a decrease in the Balmer decrement from the first to the second spectrum (at 2.6σ significance). During three epochs covering the second peak, the Balmer decrements fall below 1.5 and are comparable to those observed in SN 2009ip (E. M. Levesque et al. 2014). Following the line intensity calculations of S. A. Drake & R. K. Ulrich (1980), these values indicate emission from an extremely high-density plasma ($n_e > 10^{13}$ cm^{-3}).

5.6. NIR Spectroscopy at Secondary Maximum

In Figure 12, we plot the NIR spectrum obtained near secondary r-band maximum at +220 days. The spectrum shows a blue continuum and prominent Paschen features, and the absorption trough to the Paδ P-Cygni profile at 4000–5000 km s^{-1} is consistent with the velocity of the SN–CSM shell inferred from Hβ at +222 days (Section 5.2). He I emission features are also observed at 1.08 and 2.06 μm, and the profile of He I at 1.08 μm exhibits the same asymmetric and double-peaked profile as seen in the optical spectrum at +222 days.

To further investigate a multicomponent origin for our H/He-rich CSM, we search for He I features that are both NIR-bright and minimally contaminated by Paschen/Brackett or other strong transition lines (there are very few strong and uncontaminated H lines within this wavelength range). We select the lines at 10030.6 Å, 18685.3 Å, and 12785.0 Å from the NIST Database of Atomic Lines (Y. Ralchenko & A. Kramida 2020). We estimate and subtract a flux continuum near each line, and normalize each profile within ±2500 km s^{-1} to a maximum flux of unity.

We plot these three spectral regions in velocity space in the inset of Figure 12, along with the inferred velocities of the CSM and SN–CSM components from Section 5.2 (gray lines). We observe correlated excess flux symmetric about the rest wavelength at the same velocities suggested by the additional components in our optical spectra (shown in green) to within the spectral resolution of our data, confirming the presence of confined, slow-moving CSM.[39] The emission at the positive component is stronger than at the negative component; this may be a viewing angle effect.

O I is also detected in the NIR spectrum at 8446 and at 9263 Å, as was seen in the SNe IIn 1987F (A. V. Filippenko 1989; G. Wegner & S. R. Swanson 1996) and 2013L (F. Taddia et al. 2020). The blue continuum suggests that no substantial dust has formed, as has been observed with other SNe IIn at these or earlier phases relative to peak (e.g., 2005ip; A.-S. Bak Nielsen et al. 2018; 2010jl, N. Smith et al. 2012b; C. Gall et al. 2014). This is consistent with the high temperatures maintained during the secondary CSM interaction ($>6 \times 10^3$ K is suggested by the blackbody fits in Figure 13), as dust cannot exist or form at $\gtrsim$3000 K (C. Gall et al. 2011; A.-S. Bak Nielsen et al. 2018).

6. Blackbody Fitting and Bolometric Luminosity

Next, we infer the bolometric properties of SN 2023zkd.

We define a set of 100 day bins spanning the pre-discovery photometry (starting from the earliest $>3\sigma$ detection) and 5 day bins after discovery. In each bin, we calculate an uncertainty-weighted average of the available photometry in each filter and fit a blackbody SED to the resulting flux values. Bins containing fewer than two photometric filters pre-discovery, and three filters after discovery, are not reported. We then calculate a pseudo-bolometric luminosity in each valid bin by trapezoidal integration of the available filters, and

---

[39] We caution that contamination remains likely for these features; the closest Paschen feature (Pa 7-3 at 10052.1 Å), for moderate velocities of ~ 650 km s^{-1}, would be indistinguishable from He I at 10030.6 Å.

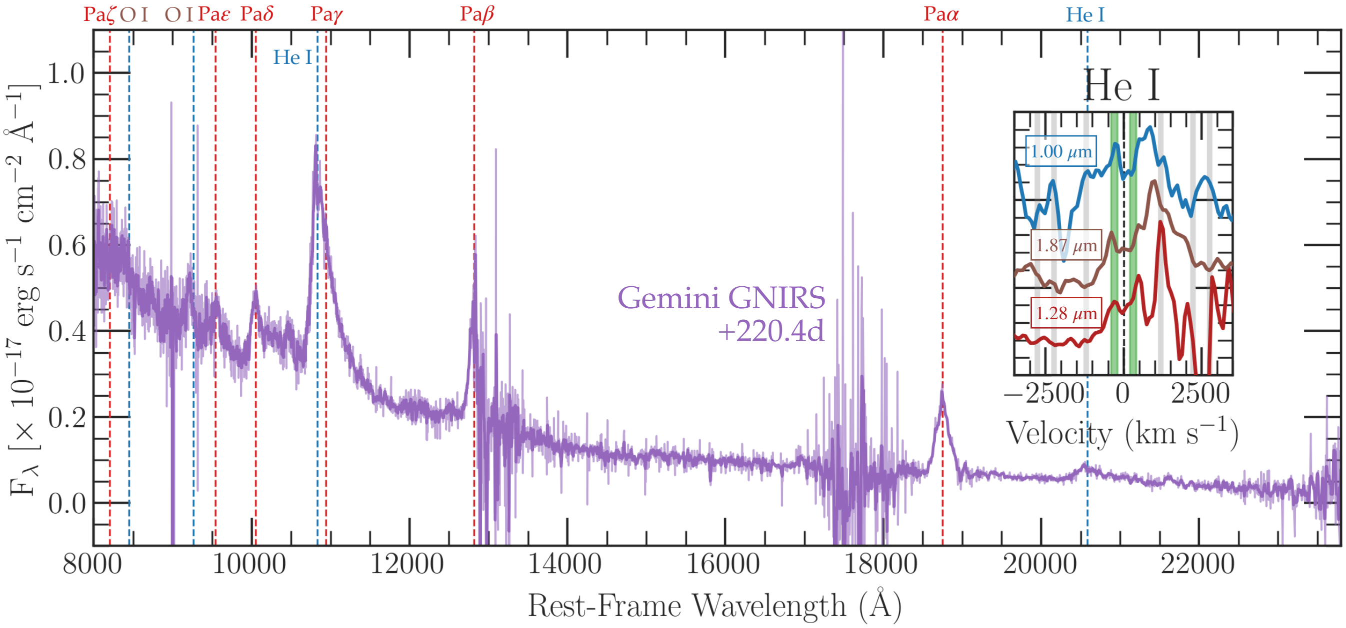

Figure 12. NIR spectrum of 2023zkd at secondary *r*-band maximum obtained with GNIRS, showing prominent H and He features superimposed on a blue continuum. The spectrum has been corrected for Galactic and host extinction. The He I profiles at 12785 Å, 10031 Å, and 18685 Å are shown in velocity space in the top-right inset, with the CSM velocity components identified in optical spectra annotated (green for ±400 km s^{-1} and gray for the velocities of the faster CSM and the SN–CSM shell during the two peaks). All profiles show evidence of low-velocity CSM components consistent with those identified at optical wavelengths.

a bolometric luminosity using the Stefan–Boltzmann law with the best-fit blackbody parameters.

We plot the resulting blackbody temperature, radius, and luminosity for bins with converged fits in Figure 13. To guide the eye, we also plot first-order spline fits of the blackbody properties along with their associated 1σ uncertainties. We show the bolometric luminosity of the precursor associated with the SN Ibn 2023fyq (top-left panel, blue line; Y. Dong et al. 2024) and the `MOSFiT`-inferred blackbody properties for the SN IIn sample modeled by C. L. Ransome & V. A. Villar (2025; thin gray lines for individual events and thick black line from a spline fit to the population, obtained by private communication).

Precursor A has a pseudo-bolometric luminosity of ∼8 × 10^{40} erg s^{-1} and a bolometric luminosity of ∼3 × 10^{41} erg s^{-1}, roughly an order of magnitude higher than the flat portion of the precursor detected in 2023fyq but comparable to the precursors to the type IIn SNe 2016bdu (A. Pastorello et al. 2018), 2015bh (which exhibited long-lived eruptions reminiscent of SN 2009ip; N. Elias-Rosa et al. 2016; C. C. Thöne et al. 2017; C. D. Kilpatrick et al. 2018), 2021qqp (D. Hiramatsu et al. 2024b), and SN 2010mc (E. O. Ofek et al. 2013). Precursor A is consistent with a ∼10^4 K blackbody of radius 0.2 ± 0.1 × 10^{15} cm, where the small radius (∼10 au) suggests emission extremely close to the progenitor system.

Interestingly, the blackbody properties of Precursor B are distinct from those of Precursor A. In Precursor B, we observe a lower blackbody temperature of ∼ 8000 K (also suggested by the $g-r$ color evolution in Figure 4) and a marginally higher blackbody radius of 0.8 ± 0.2 × 10^{15} cm. The luminosity is also higher, ∼10^{42} erg s^{-1} and aligns with the steady brightening seen in the multiband photometry.

After each of the photometric peaks, the bolometric luminosity reaches a comparable observed maximum of ∼ 6 × 10^{42} erg s^{-1}. The blackbody temperature steadily increases from the end of the first seasonal gap to a maximum of ∼8000 K at the second photometric peak. It then decreases through the decline of the second peak, reaching a minimum of 3000–4000 K. The second peak is also accompanied by a decrease in the blackbody radius relative to the photometry at +80 days, to a minimum of ∼10^{15} cm.

The median bolometric properties of the SN IIn sample from C. L. Ransome & V. A. Villar (2025) align closely with the first-peak evolution of 2023zkd, further confirming its classification and suggesting an unobserved first peak bolometric luminosity near ∼3 × 10^{43} erg s^{-1}. The blackbody temperature near the end of the first peak is comparable to the SN IIn population, but the blackbody radius is systematically lower at all phases. This may suggest emission from a more compact interaction zone, or may be an artifact of the temperature floor (the minimum temperature the photosphere can cool to before it must recede) set in those models.

7. Inferring the Properties of the Circumstellar Medium

7.1. Constraints on the CSM Mass with MOSFiT

We now constrain the properties of the CSM using the Modular Open Source Fitter for Transients (`MOSFiT`; J. Guillochon et al. 2018). `MOSFiT` fits a model to user-provided multiband photometric data using a chosen sampling method (we use nested sampling via `dynesty`). We use the CSM interaction models of E. Chatzopoulos et al. (2012), which were originally based on the work of R. A. Chevalier (1982) and then extended by V. A. Villar et al. (2017) and B. Jiang et al. (2020). Most models in `MOSFiT`, including the CSM interaction model, take the form of a blackbody SED and an expanding and cooling photosphere, which recedes when a minimum temperature is reached. We impose a set of physically informed priors on the parameters, which are presented in Table 3. The parameters that are used in the fitting of the CSM model are as follows:

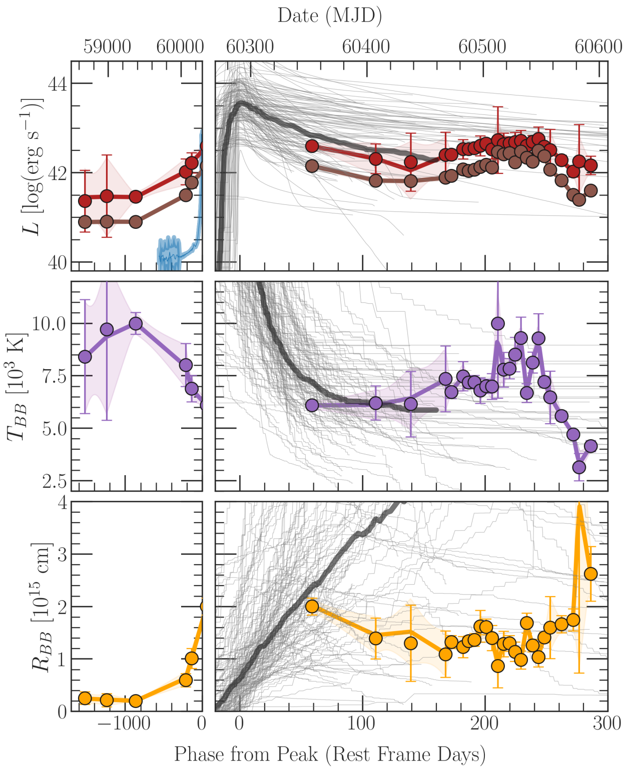

Figure 13. Blackbody properties of SN 2023zkd in 100 day bins pre-discovery (left column) and 5 day bins after discovery (right column). Spline fits are shown for all properties (colored lines) with associated 1σ uncertainties (shaded regions). The event's pseudo-bolometric luminosity (top panel, brown points) is estimated by trapezoidal integration of available photometry in each bin and the bolometric luminosity (red points) is calculated by integrating the best-fit blackbody curves for each bin. The blackbody temperature (middle panel, purple) and radius (bottom panel, gold) is also shown. The precursor emission associated with the SN Ibn 2023fyq (Y. Dong et al. 2024) is shown in blue in the top-left panel for comparison, as are the median (thick black line) and individual (thin gray lines) blackbody properties for archival SNe IIn derived from the fits in C. L. Ransome & V. A. Villar (2025) (gray lines, obtained via private communication).

1. s, the CSM profile geometry parameter, where $\rho \propto r^{-s}$. Unlike in most other work, s is left as a free parameter (between 0 and 2), but smaller values of s indicate a more shell-like CSM geometry. Conversely, when s approaches 2, the CSM can be considered wind-like with a steady mass-loss rate.
2. n, describing the SN ejecta density profile set by the polytropic index of the stellar envelope. n is varied between 7 and 12.
3. R_0, the inner CSM radius.
4. ρ_0, the density of the CSM at R_0, i.e., the inner CSM density.
5. $\mathrm{M_{CSM}}$, the total CSM mass.
6. v_{ej}, the characteristic velocity of the ejecta (which scales with the ejecta mass and explosion energy as $v_{\mathrm{ej}} = \sqrt{\frac{10\,E_{\mathrm{SN}}}{3\,M_{\mathrm{ej}}}}$)
7. T_{min}, the temperature at which the photosphere begins to recede.
8. Nuisance parameters such as σ, which quantifies any potential photometric uncertainty in excess of the measured values.

Table 3
Median and 1σ Confidence Intervals for the Parameters of the Circumstellar Interaction Model in `MOSFiT`

Parameter	Units	Prior	Posterior Median and 1σ Range
$\log_{10}(M_{\mathrm{CSM}})$	$\log_{10}(M_{\odot})$	$\log U(0.1,\ 100)$	$0.32^{+0.02}_{-0.02}$
n	⋯	U(7, 12)	$9.46^{+0.64}_{-0.42}$
$\log_{10}(n_{\mathrm{H,host}})$	$\log_{10}(\mathrm{cm}^{-3})$	$\log U(10^{16},\ 10^{23})$	$17.49^{+0.95}_{-1.02}$
$\log_{10}(R_0)$	$\log_{10}(\mathrm{AU})$	$\log U(1,\ 100)$	$0.93^{+0.35}_{-0.33}$
$\log_{10}(\rho_0)$	$\log_{10}(\mathrm{g\ cm}^{-3})$	$\log U(10^{-15},\ 10^{-11})$	$-12.42^{+0.60}_{-0.33}$
s	⋯	U(0,2)	$0.68^{+0.24}_{-0.18}$
$\log_{10}(T_{\mathrm{min}})$	$\log_{10}(\mathrm{K})$	$\log U(1,\ 10^4)$	$1.39^{+2.20}_{-0.93}$
t_{exp}	days	U(−20, 0)	$-19.17^{+1.03}_{-0.59}$
$\log_{10}(\sigma)$	$\log_{10}(\mathrm{mag})$	$\log U(10^{-5},\ 1)$	$-0.53^{+0.01}_{-0.01}$
$\log_{10}(v_{\mathrm{ej}})$	$\log_{10}(\mathrm{km\ s}^{-1})$	$\log U(10^3,\ 10^5)$	$3.38^{+0.01}_{-0.01}$

Note. Parameter definitions are provided in the text.

The ejecta mass is set to $M_{\mathrm{ej}} = 10\,M_{\odot}$. Using our set of physically informed priors, we fit the photometry of SN 2023zkd during only the secondary peak (we exclude first-peak photometry due to the lack of temporal coverage and `MOSFiT`'s inability to model CSM structure deviating from the expected $\rho \propto r^{-s}$ profile). We construct posterior distributions of the parameters listed above, and estimate the CSM properties powering SN 2023zkd's secondary peak from each posterior's median and 1σ standard deviation.

We present the median of the posteriors obtained from our modeling in Table 3. We find a reasonably well-constrained CSM mass of 2–2.2 $M_{\odot}$, whose interaction with the SN ejecta powers the secondary peak. Note that s, which parameterizes the density profile of the CSM, is constrained to $s = 0.68^{+0.24}_{-0.18}$. This suggests a "shell-like" density profile, and is lower than the median value of $s = 1.27$ inferred for the population SNe IIn fit with the `MOSFiT` model in C. L. Ransome & V. A. Villar (2025). A corner plot of the joint posteriors across all realizations is shown in Appendix C.

The median value for the posterior of n, which parameterizes the ejecta density profile, is $9.46^{+0.64}_{-0.42}$. n can be used to distinguish between red supergiant-like progenitors (whose indices are typically considered to be $n = 12$; C. D. Matzner & C. F. McKee 1999; T. J. Moriya et al. 2013) and LBV or W-R-like progenitors for SNe IIn (having $7 < n < 10$; S. A. Colgate & C. McKee 1969). The range inferred for SN 2023zkd suggests a density structure more aligned with LBV-like progenitors, though the range is large. The inner CSM density required to power the second maximum, $\rho \sim 10^{-12.4}$ g cm^{-3}, is well constrained and consistent with archival SNe IIn (C. L. Ransome & V. A. Villar 2025).

The inferred ejecta velocity associated with the secondary peak is 2340–2460 km s^{-1}, substantially lower than the median value of $4{,}810^{+3{,}454}_{-2{,}082}$ km s^{-1} reported for the SN IIn sample in C. L. Ransome & V. A. Villar (2025). These low velocities could be due to deceleration of the ejecta from collision with the CSM that powers the first light curve peak.

We keep the ejecta mass fixed at $M_{\mathrm{ej}} = 10\,M_{\odot}$ in our modeling. In separate `MOSFiT` runs where we fit this parameter, two solutions are degenerate and consistent with the photometry: one with lower ejecta mass ($10\,M_{\odot} < M_{\mathrm{ej}} < 15\,M_{\odot}$, comparable to our assumed value) and higher CSM mass ($1.5\,M_{\odot} < M_{\mathrm{CSM}} < 2.5\,M_{\odot}$); and another with higher ejecta mass

($40\,M_\odot < M_{\rm ej} < 45\,M_\odot$) and lower CSM mass ($0.5\,M_\odot < M_{\rm CSM} < 1\,M_\odot$). The solution with higher ejecta mass can be ruled out from the explosion energy most consistent with the SN–CSM shell velocities, as we discuss in Section 7.2. We conclude that an ejecta mass of $10\,M_\odot < M_{\rm ej} < 15\,M_\odot$ is most likely.

Finally, we use our model constraints to infer an average mass-loss rate associated with the secondary peak. We calculate $R_{\rm CSM}$, the characteristic CSM radius probed at these epochs under the assumption of a constant CSM velocity, as

$$R_{\rm CSM} = (A \cdot M_{\rm CSM} + B)^C \tag{2}$$

with

$$A = \frac{3 - s}{4\pi\rho R_0^s} \tag{3}$$

$$B = R_0^{3-s} \tag{4}$$

$$C = \frac{1}{3 - s}. \tag{5}$$

We find a value of $R_{\rm CSM} \approx 0.4 \times 10^{15}$ cm, comparable to the results from our blackbody fits (bottom panel of Figure 13). Then, we estimate the average mass-loss rate as

$$\langle \dot{M} \rangle \approx \frac{M_{\rm CSM} \cdot v_{\rm CSM}}{R_{\rm CSM}}, \tag{6}$$

where we adopt a median CSM velocity during the second peak of $v_{\rm CSM} \approx 2200$ km s^{-1} from our spectroscopic fits in Section 5. Substituting values, we find $\dot{M} \approx 20\,M_\odot$ yr^{-1}. This is likely an overestimate of the true mass-loss rate associated with the second peak due to MOSFiT's underestimation of the CSM extent $R_{\rm CSM}$ (see C. L. Ransome & V. A. Villar 2025, for a discussion), as well as the possibility of mechanical acceleration of the CSM probed by our spectral modeling. If we instead assume that the CSM from the second peak is accelerated by collision, and adopt the lower CSM velocity of $v_{\rm CSM} \approx 1200$ km s^{-1} from the +90 day spectrum, we find a value of $\dot{M} \approx 11\,M_\odot$ yr^{-1}. This value is more consistent with the mass-loss rate of $\sim 7\,M_\odot$ yr^{-1} we infer from the shock model in the following section.

7.2. Shock Modeling

We can also reconstruct a nonparametric CSM density profile and associated mass-loss history for 2023zkd using the same shock-luminosity formalism that was adopted for SN 2021qqp (D. Hiramatsu et al. 2024b). Since both the photometric and spectroscopic evolution of SN 2023zkd suggest an interaction-dominated transient, the model's assumption that the transient is exclusively powered by the interaction between the expanding fast-moving SN ejecta and surrounding CSM (with kinetic energy at the forward and the reverse shocks dissipating energy to optical photons) is well justified.

We adopt a fiducial value of $M_{\rm ej} = 10\,M_\odot$ for the explosion ejecta mass (as was used for SN 2021qqp and suggested by our earliest `MOSFiT` modeling in Section 7.1; we discuss the validity of this assumption below), along with $\delta = 0$ and $n = 12$ for the indices of the broken power-law density profile describing the SN ejecta (though our `MOSFiT` fits from Section 7.1 suggest an index closer to 10, the posterior is broad). We further define a constant radiative efficiency for both the forward and the reverse shock of $\varepsilon = 0.5$, as is assumed in our `MOSFiT` models.

Given the lack of spectroscopic constraints through the first light curve peak, we assume an initial SN–CSM shell velocity of 10,000 km s^{-1}. We set the initial CSM velocity to 1176 km s^{-1}, as calculated from our Hα emission-line fits. Though we find evidence for lower-velocity CSM in Section 5.3, the broad-line profiles indicate that the interaction with the faster CSM dominates the observed emission. The total energy of the explosion, $E_{\rm SN}$, is constrained by comparing the model's predicted shell velocities to those we measure in Section 5.2.

We plot the results of our shock modeling in Figure 14. The upper-left panel compares the luminosity contributions from the forward and reverse shocks to the bolometric luminosity, while the upper-right panel shows the temporal evolution of the SN–CSM shell velocities for different assumed $E_{\rm SN}$. The bottom panels show the associated CSM density profile (left) and mass-loss rates as a function of time to explosion (right), assumed to be the discovery date of MJD = 60132.5. The measured SN–CSM shell velocities are consistent with an explosion of energy $E_{\rm SN} = 2 \times 10^{51}$ erg (the observed scatter is a result of the blueward skew of the P-Cygni absorption feature in the later spectra, which leads to degeneracies in the emission and absorption Gaussian profiles used to fit the Hβ line).

For an assumed explosion energy of $E_{\rm SN} = 2 \times 10^{51}$ erg, we infer a mass-loss history with two distinct peaks at $\sim$1–2 yr and $\sim$3 yr prior to explosion (blue line), with the progenitor ejecting material at a maximum rate of $\sim 4\,M_\odot$ yr^{-1} and $\sim 7\,M_\odot$ yr^{-1} at the first and second episodes, respectively. Integrating the full mass-loss history leads to a total CSM mass of 5–6 $M_\odot$, with $M_{\rm CSM} \approx 2\,M_\odot$ inferred from the second peak alone. This second-peak estimate is compatible with the mass suggested by `MOSFiT`, despite different assumptions about the ejecta density profile n.

We caution that this approach has assumed that the SN explosion began at the discovery date, whereas the photometry prior to the first seasonal gap could be entirely precursor emission due to the slow rise times (see Section 4). If this is the case, it will not be well characterized under the assumption of SN–CSM interaction. For this reason, we consider the mass-loss episode $\sim$3 yr before explosion to be more tightly constrained. We note, however, that if Precursor A is taken to be composed of two distinct mass-loss episodes, the first set of detections spans 2.7–4.0 yr prior to discovery while the second set spans 0.7–2.2 yr prior to discovery. These are well matched to the mass-loss phases suggested by our shock modeling assuming an explosion time of the discovery epoch, although at the level of our Precursor A detections, we cannot distinguish between persistent emission and two eruptive episodes.

Finally, we comment on the validity of our assumed $M_{\rm ej} = 10\,M_\odot$. The adopted shock model gives a rough scaling relation between the event's explosion energy $E_{\rm SN}$ and the ejecta mass $M_{\rm ej}$. Rearranging Equation (14) from D. Hiramatsu et al. (2024b), we find that for explosion energies of 10^{51} erg s^{-1} $< E_{\rm SN} < 5 \times 10^{51}$ erg s^{-1} (higher values are incompatible with our shell velocity evolution, shown in the top-right panel of Figure 14), 2023zkd requires $2\,M_\odot < M_{\rm ej} < 15\,M_\odot$. This range is consistent with the lower-mass solution found by `MOSFiT` ($10\,M_\odot < M_{\rm ej} < 15\,M_\odot$) and

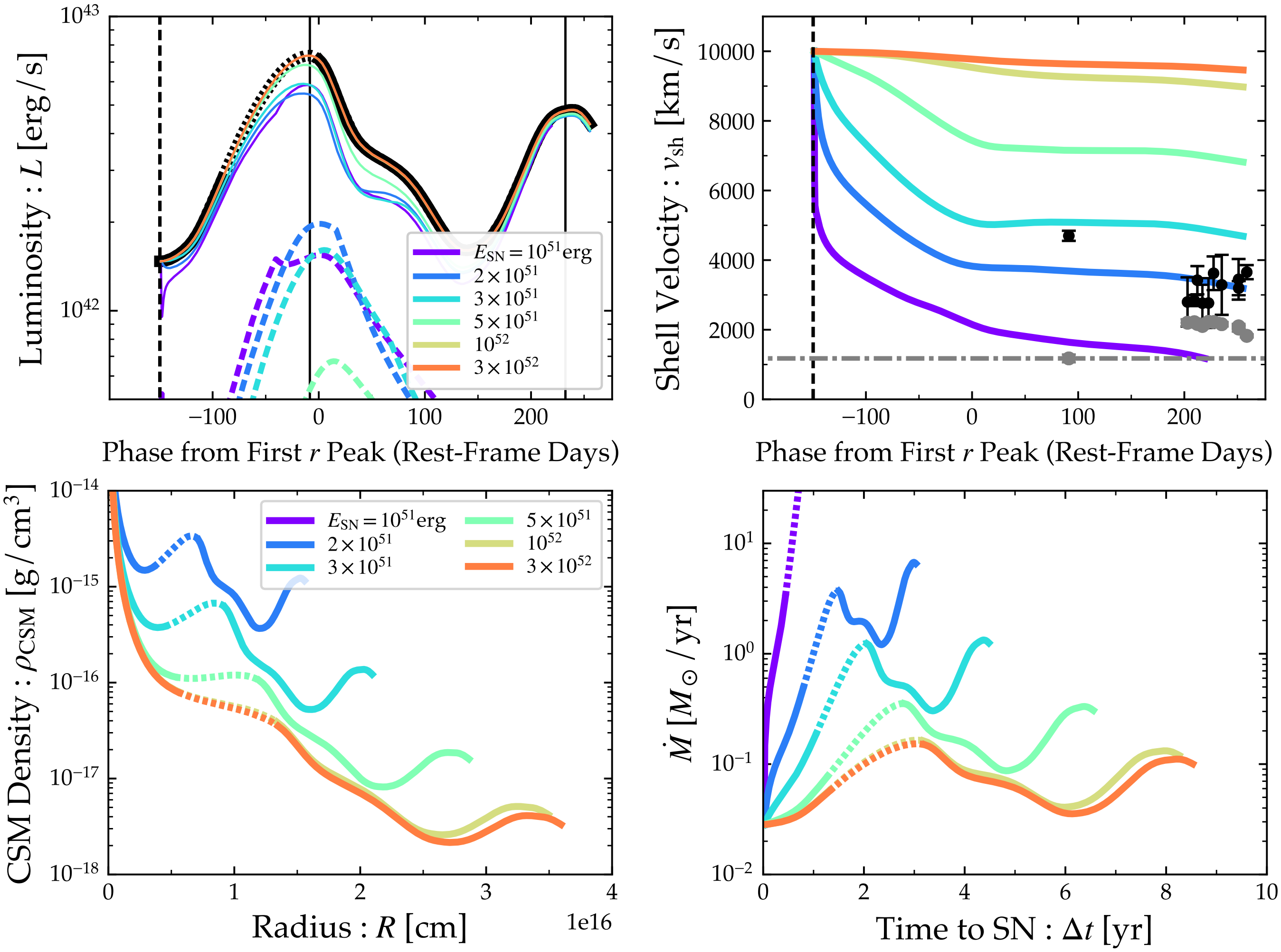

Figure 14. Top-left panel: luminosity evolution of the forward (solid colored lines) and reverse (dashed colored lines) shocks for the best-fitting models to the interpolated 2023zkd photometry (black curve). The dashed section of the black curve denotes the seasonal gap in observations. Top-right panel: evolution of the associated SN–CSM interaction shell velocity for the models shown at left. Black points indicate the SN–CSM velocities measured from the absorption trough of the Hβ profile, and gray points indicate the CSM velocities measured from the narrow component of the Hα profile. The SN–CSM measurements are consistent with an explosion of energy $E_{\rm SN} = 2 \times 10^{51}$ erg s^{-1} (dark-blue line). Bottom-left panel: inferred density profiles for the models at the top, which suggest highly structured CSM with two distinct overdensities. Bottom-right panel: inferred mass-loss rates for the SN 2023zkd progenitor. With an assumed efficiency of $\epsilon = 0.5$ and ejecta mass of $10 M_\odot$, the total CSM mass is estimated to be 5–6 $M_\odot$.

comparable to the ejecta mass inferred for 2021qqp (they find a lower total CSM mass of 2–4 $M_\odot$ due to their higher shell velocities/inferred $E_{\rm SN}$; D. Hiramatsu et al. 2024b).

7.3. Pre-explosion Mass-loss Limits from Swift/XRT Nondetections

We follow the prescription outlined in S. Immler et al. (2006) to convert the unabsorbed X-ray flux upper limit derived in Section 2.3 during the secondary maximum to a maximum mass-loss rate for the system. We assume that the SN luminosity during the second peak is fully shock-powered, with the reverse shock L_r contributing 30x as much as the forward shock L_f to the total observed luminosity (due to the higher CSM density at the reverse shock; relative ratios of 10–100 are suggested in R. A. Chevalier 1982, which change our upper limit by at most a factor of 2). We adopt a CSM power-law index of $s = 0.6$ from our `MOSFiT` results in Section 7.1, and an ejecta profile index of $n = 12$. We assume our CSM has a mean mass per particle of $\approx 2.1 \times 10^{-24}$ g as appropriate for H+He plasma (e.g., A. A. Miller et al. 2010), and we adopt a value for the cooling function of $\Lambda = 3 \times 10^{-23}$ erg s^{-1} cm^3 (appropriate for a plasma with $T = 10^9$ K).

Substituting values, our X-ray nondetection corresponds to a 3σ upper limit of

$$\frac{\dot{M}}{M_\odot\ {\rm yr}^{-1}} \leqslant 2.2 \times 10^{-7} \times \left(\frac{v_{\rm sh}}{\rm km\ s^{-1}}\right)^{0.61} \left(\frac{t}{\rm day}\right)^{0.61} \left(\frac{v_w}{\rm km\ s^{-1}}\right). \tag{7}$$

Assuming a shock velocity at secondary maximum of $\sim$3300 km s^{-1} (from the median of the velocities of the Hβ trough in Section 5.4), a CSM velocity of $\sim$2200 km s^{-1} from the median FWHM of the narrow component of Hα, and a phase of $t \approx 74$ days from the start of the secondary peak in the rest frame, we infer a mass-loss rate of $\dot{M} < 1.0\ M_\odot$ yr^{-1}. Adopting the initial shock velocity of 10,000 km s^{-1}from Section 7.2 increases the limit by a factor of 2, while assuming $n = 10$ from our `MOSFiT` results leads to a tighter limit of

$\dot{M} < 0.1\,M_\odot\,\mathrm{yr}^{-1}$. All of these estimates are lower than the mass-loss rate derived from the shock modeling in the following section for an SN explosion energy of $2 \times 10^{51}\,\mathrm{erg\,s^{-1}}$, but only take into account absorption by the Galactic ISM. Photoelectric absorption by a thick neutral medium, as well as an asymmetric explosion or CSM structure (as has been invoked for SN 2023ixf as an explanation for Swift X-ray nondetections; S. Panjkov et al. 2024), could suppress X-ray emission from photons produced during the SN–CSM interaction.

8. Discussion

8.1. Emission Phases and CSM Geometry

The observational sequence obtained for SN 2023zkd presents multiple peculiarities. The distinct phases of precursor emission (persistent for years during Precursor A followed by a brightening and reddening to discovery during Precursor B) are unlike those observed in other SNe IIn (e.g., N. L. Strotjohann et al. 2021) and qualitatively similar to that observed in 2023fyq (S. J. Brennan et al. 2024a; Y. Dong et al. 2024), where a brightening precursor was associated with runaway accretion onto a binary companion (D. Tsuna et al. 2024). Nevertheless, important differences also exist: Precursor A is an order of magnitude more luminous than the plateau phase of 2023fyq (with an integrated pseudo-bolometric luminosity of $\sim 10^{41}\,\mathrm{erg\,s^{-1}}$), while the brightening rate during Precursor B is substantially lower. Further, the progenitor system proposed for 2023fyq was a low-mass ($\sim 3\,M_\odot$) helium star with a neutron star companion, whereas the ejecta and CSM masses inferred for 2023zkd ($M_{\mathrm{ej}} \approx 10\,M_\odot$ and $M_{\mathrm{CSM}} \approx 5\,M_\odot$) favor a substantially more-massive progenitor.

Across all phases, 2023zkd also exhibits H/He line flux ratios lower than He-rich SNe IIn but higher than transitional SNe Ibn/IIn. The multipeaked H and He I profiles also suggest axisymmetric CSM components associated with both lower velocities (200–400 $\mathrm{km\,s^{-1}}$ and higher velocities (1200–2200 $\mathrm{km\,s^{-1}}$). The higher-velocity components are most pronounced in the He I profiles at +90 days, while the lower-velocity components dominate the peaks of the H profiles at the same epoch. Throughout the second light curve peak, multiple components are simultaneously observed (though many are blended) across both H and He profiles.

These observations strongly suggest interaction with two axisymmetric CSM components. The appearance of multiple components in both H and He from the +90d to the +258d spectrum suggests these components have distinct axes of symmetry, such that both are exposed to the initial SN shock and subsequent ejecta.

A configuration involving an outer, slow-moving, and toroidal/ring-like outflow and an inner, fast-moving bipolar outflow provides a natural explanation. This geometry is regularly observed in the circumstellar environments of Galactic stars, and equatorially distributed CSM has been invoked to explain the observations of numerous other interacting SNe. For the re-brightening of 2009ip (E. M. Levesque et al. 2014), a detached, disk-like CSM was favored over a spherically symmetric CSM shell due to the low Balmer decrement and the absence of P-Cygni profiles.[40] A toroidal CSM geometry was similarly proposed for the type Ib SN 2014C (that later transitioned into an SN IIn) due to the persistence of a 2000 $\mathrm{km\,s^{-1}}$ feature observed in Hα and no other lines (though, in the proposed collision between the SN ejecta and the toroidal CSM, the source of the H-rich material moving at this velocity was ambiguous; B. P. Thomas et al. 2022). High polarization in the emission from the SN IIn 1998S, coupled with double-peaked emission profiles, were similarly explained as dense disk- or ring-like CSM (D. C. Leonard et al. 2000; J. Mauerhan & N. Smith 2012). Finally, the early double-peaked He I profiles for SN IIn 1996al were argued to be the result of an explosion into stratified equatorial CSM (see Figure 22 of S. Benetti et al. 2016).

The mostly distinct peaks of H (low-velocity) and He I (high-velocity) at +90 days (during the decline of the first peak) can be explained by CSM components that are also partially compositionally distinct, with the bulk of the H confined to the lower-velocity CSM and the He associated with the higher-velocity CSM (though fainter high-velocity shoulders are marginally detected in, e.g., the Hβ component at this epoch, indicating that the components may be mixed during the interaction). The He I profiles are significantly broader than the H profiles at this phase, suggesting that the He I profiles may be Doppler broadened at this phase.

By the rise of the second peak (+209 days), both H and He are emitted from the high-velocity CSM. Much narrower double-peaked He I profiles are observed, and the Hα peak has broadened. This may be suggestive of a secondary collision with CSM more enriched in H than the first collision. This interaction dominates the second photometric peak.

A progenitor scenario for the explosion must reconcile these observational properties. We consider the viability of multiple progenitor systems and their implied mass-loss histories below.

8.2. Progenitor Scenarios for SN 2023zkd

8.2.1. Core Collapse of a Single Massive Star

First, we consider a single massive star as the progenitor to 2023zkd. Single-star LBVs and W-Rs have each been considered as the progenitors of strongly interacting SNe, with multiple lines of evidence in favor of each (A. Gal-Yam & D. C. Leonard 2009; V. V. Dwarkadas 2011; A. Pastorello et al. 2015).

The high-velocity CSM component observed in 2023zkd is faster than what is typically inferred for LBV winds, but is well within the range of wind velocities proposed for W-Rs (N. Smith 2017b). This, coupled with the detection of He II and tentatively N III during the secondary peak, ostensibly suggest a nitrogen-rich W-R (WN) wind. A young WN has been proposed as the progenitor of multiple strongly interacting SNe, including the SN Ibn 2006jc (R. J. Foley et al. 2007) and the transitional type IIn/Ibn SN 2005la (A. Pastorello et al. 2008b).

The pre-explosion photometry, on the other hand, supports an LBV scenario: the luminosity and decreasing temperature of Precursor A (10,000 K to ∼ 8000 K) aligns well with the luminosities and temperature evolution reported for LBV outbursts (R. M. Humphreys & K. Davidson 1994; Y.-F. Jiang et al. 2018) and observed in, e.g., 2009ip (N. Smith et al. 2011a). Finally, the timescale of Precursor A is suggestive of an LBV undergoing S-Dor eruptions, whereas both the

---

[40] The latter are expected in the strong velocity gradient established by an expanding spherical shell, whereas narrow features are more suggestive of a narrow-line-emitting region.

increasing bolometric luminosity of Precursor B and its magnitude ($\sim 10^{42}$ erg s^{-1}) are consistent with observed giant outbursts (R. M. Humphreys & K. Davidson 1994; see also the evolution of the 2012a outburst of 2009ip in, e.g., Figure 1 of N. Soker & A. Kashi 2013).

Both progenitor systems may naturally give rise to axisymmetric CSM structures with distinct compositions. (V. V. Dwarkadas & S. P. Owocki 2001; S. Akras & J. A. López 2012). In the Generalized Interacting Stellar Wind model, a fast-moving and isotropic wind emitted from an LBV or W-R collides with a slow-moving and dense toroidal structure (A. Frank et al. 1995). The interaction between components produces bipolar lobes of fast-moving material, as observed in W-R planetary nebulae (A. Danehkar 2022) and nearly all Galactic LBVs (e.g., η Car, HG Car, and A Car; J. H. Groh et al. 2009). Hydrodynamic simulations of massive LBV outbursts (J. P. Cassinelli & R. Ignace 1997; G. Garcia-Segura et al. 1997) suggest that near-critical rotation can also give rise to *both* bipolar outflows and dense equatorial material during a single outburst (see also V. V. Dwarkadas & S. P. Owocki 2001). Further, the majority of Galactic eruptive LBVs are also near-critical rotators. J. H. Groh et al. (2009) suggested that this rapid rotation may also prevent the loss of angular momentum required to transition to a WN, potentially leading to an explosion as an LBV.

Despite the compositional similarities, a single W-R alone seems extremely unlikely to have produced 2023zkd. The mass-loss rates inferred for WNs (10^{-6}–$10^{-4}\,M_\odot$ yr^{-1}) are many orders of magnitude lower than suggested by 2023zkd's two photometric peaks (N. Smith 2017b; though this can be partially reconciled by proposing short-lived W-R phases, which can rapidly sweep up CSM and produce dense shells despite low intrinsic mass-loss rates; see V. V. Dwarkadas 2011, for a discussion). An obvious additional problem is that the W-R stage of stellar evolution, canonically, denotes core-He burning with the absence of H, while we observe prominent and multicomponent H features at all phases of emission. Intermediate velocities, as we have observed for 2023zkd, are also not expected beyond the short-lived early WN stage (A. J. van Marle et al. 2005).

There are also multiple challenges with a single-star LBV origin for 2023zkd. Precursor A ($M_r \approx -15$ mag) is 3 magnitudes brighter than the brightest LBV S-Dor outburst observed to date (R. M. Humphreys & K. Davidson 1994), and the steady brightening of Precursor B is more suggestive of a continuous than an eruptive emission mechanism.[41] Finally, the LBV stage for stars of initial mass $>30\,M_\odot$ is believed to be short-lived (10^4 yr; A. J. van Marle et al. 2005). The explosion of an LBV in the midst of transitioning to an H-free WN may require excessive fine-tuning.

In conclusion, while 2023zkd exhibits signs of both massive LBV-like and WN progenitors, neither is a strong match. There has been steadily mounting evidence for alternative evolutionary channels for a massive star that include an LBV stage. For massive H-rich systems, in particular, the WN stage could *precede* the LBV stage instead of following it. The CSM velocities and compositions that suggest WN-like winds, coupled with the LBV-like Precursor B, make this rare evolutionary pathway worthy of consideration.

8.2.2. Transition of an H-rich WN to an LBV

The observational taxonomy of WNs has recently expanded to include H-*rich* WNs (designated "WNhs"; N. Smith & P. S. Conti 2008; F. Martins 2023; A. C. Gormaz-Matamala et al. 2025), stars whose compositions are not predicted by traditional evolutionary theory (e.g., R. M. Humphreys & K. Davidson 1994). These systems are produced at systematically higher masses than H-free WNs, and might provide an explanation for the H-rich ejecta in 2023zkd. As 2023zkd occurred in a low-metallicity host ($Z \approx 0.1\,Z_\odot$), it may be also possible to minimize mass-loss rates during the WNh stage such that an LBV-like successor achieves near-critical rotation. This could reproduce both the assumed multi-component circumstellar medium (CSM) geometry and the narrow, double-peaked profiles of H and He.

While the mass-distribution of H-*poor* WNs peaks closer to the inferred $M_{\rm ej} + M_{\rm CSM} \approx 15\,M_\odot$ value for 2023zkd (10–20 $M_\odot$, compared to $>30\,M_\odot$ for WNhs; N. Smith & P. S. Conti 2008), this could be taken as a lower limit on the true progenitor mass given the likelihood of sustained, enhanced mass loss—this is assuming that a characteristic mass-loss rate of $10^{-5}\,M_\odot$ yr^{-1} from Figure 3 of N. Smith & P. S. Conti (2008) over a typical lifetime of $\sim$3 Myr introduces 30 $M_\odot$ of additional mass lost during the MNH stage, placing the progenitor mass near the peak of the distribution of spectroscopic masses measured for Galactic WNhs (see Figure 1 of N. Smith & P. S. Conti 2008). Due to the observed scaling between the WNh luminosity and H mass fraction in Figure 2 of N. Smith & P. S. Conti (2008), a WNh progenitor luminous enough to power Precursor A would also produce H-rich CSM.

Nonetheless, the WNh stage of a single massive progenitor can be ruled out based on theoretical grounds. The observed luminosity of Precursor A, if attributed to an WNh wind, surpasses even the Eddington luminosity of a 100 $M_\odot$ star. Though luminosity phases approaching the Eddington limit are expected for massive stars given their myriad instabilities (G. Rakavy & G. Shaviv 1967; N. Langer 1997; H. Saio 2009; K. Davidson 2020), a star with mass close to 2023zkd's ejecta mass of 10 $M_\odot$ surpassing its Eddington limit by multiple orders of magnitude for years seems exceedingly unlikely.

Sustained super-Eddington luminosities can be naturally achieved with additional energy input from binary interaction (e.g., M. C. Begelman 2002). Companion interaction affects the majority of massive stars (H. Sana et al. 2012) and is expected to play a sizable role in the evolution of LBVs (N. Smith et al. 2011a). A binary progenitor also provides an intuitive explanation for equatorially distributed CSM (e.g., S. L. Schrøder et al. 2020); η Carinae, the well-studied Galactic system whose LBV-like outbursts produced the bipolar lobes and equatorial "skirt" of the Homunculus nebula (K. Davidson et al. 1997; D. J. Hillier et al. 2001; J. H. Groh et al. 2012; L. A. Zapata et al. 2022), is known to contain at least two massive stars (W. Bednarek & J. Pabich 2011; C. Panagiotou & R. Walter 2018). We investigate whether a binary progenitor can reproduce the observational properties of 2023zkd below.

---

[41] As a note of caution, the limited number of statistically significant detections pre-discovery make it challenging to distinguish between a monotonic increase in brightness and a long-lived eruption blending with the early SN rise near discovery; the statistical analysis of the rise in Appendix A (Figure 15, left panel) suggests that an eruption may also be also consistent with the photometry, and the giant outburst in the LBV HD 5980 was of comparable duration (N. Smith 2017b).

8.3. Binary-driven Merger-supernova

Motivated by the above considerations, we now consider a binary progenitor system for SN 2023zkd.

A massive stellar companion has been suggested for systems with similar CSM geometries to η Car., but theoretical studies suggest that the energy budget provided by colliding winds from these stars is insufficient to explain Precursor A (e.g., L. Abaroa et al. 2023). Super-Eddington accretion onto a compact companion provides a more favorable energy budget, with luminosities of $\sim 10^{41}$ erg s^{-1} favoring systems involving a black hole accretor (assuming spherical symmetry, the Eddington limit for accretion onto a companion of mass M_* is $\sim 10^{38}$ $(M_*/M_\odot)$ erg s^{-1}; M. Brightman et al. 2019). As a result, we discuss the feasibility of a binary progenitor between a massive primary and a black hole BH companion below.

After leaving the main sequence, an inflated primary star orbiting a black hole companion could overflow its Roche-Lobe and undergo stable mass transfer of its envelope (K. Pavlovskii et al. 2017; M. Gallegos-Garcia et al. 2021). The companion could detach before the star is fully stripped, leaving the primary with a residual H envelope. The mass of H-rich material remaining after this stable mass-transfer phase is highly dependent on metallicity, with a lower-metallicity primary producing a less-inflated envelope and more-massive H-rich material remaining after stable mass transfer has ceased (J. Klencki et al. 2020). Extrapolation of the results in E. Laplace et al. (2020) suggests that a primary of initial mass $M_{\mathrm{ZAMS}} > 30\,M_\odot$ and BH companion of mass $\sim 10\,M_\odot$ may be able to end this initial stage of mass transfer with a $\sim 10\,M_\odot$ He core and a residual envelope of $\sim 1\,M_\odot$ H/He.[42]

Following core-He burning, the re-expansion of the progenitor can restart mass transfer onto the companion (E. Laplace et al. 2020). Mass transfer is expected to be unstable at this secondary stage due to the progenitor's convective envelope (P. Marchant et al. 2021), causing the majority of stripped material to become unbound and distributed equatorially as a circumbinary outflow (CBO; as in, e.g., T. Morris & P. Podsiadlowski 2006). The loss of angular momentum from this material can cause a tightening of the binary in a runaway interaction that drives a monotonic increase in luminosity from disk winds and ends in a merger (M. MacLeod et al. 2018a; M. MacLeod & A. Loeb 2020b).

The luminosity and the years-long timescale of Precursor A can be produced by super-Eddington accretion during this unstable mass-transfer stage (S.-S. Weng & S.-N. Zhang 2011). The brightening seen during Precursor B is a strong indication of a shrinking binary separation during unstable accretion and is predicted by multiple models (e.g., N. Soker & A. Kashi 2013; D. Tsuna et al. 2024). In the merger-SN formalism modeled by D. Tsuna et al. (2024), a low-velocity CSM component arises from the CBO of stripped H/He (moving at a few hundred kilometers per second) and a faster-velocity component originates from polar outflows of the He-rich circumbinary disk (moving at 1000–10,000 km s^{-1}). Both predictions are consistent with the components observed in 2023zkd. Binary interaction can also produce CSM components with distinct geometries, compositions, and velocities according to the interaction phases at which they were ejected, with CSM ejected during runaway interaction probing He-rich material in the primary and collimated along the poles by its interaction with pre-existing toroidal CSM deposited in an earlier stage of mass loss (M. MacLeod et al. 2018b). Further, models for a merger-driven SN suggest an initial emission signature from radiative cooling of a confined inner envelope heated by the SN shock; substituting the properties of 2023zkd into Equations (40) and (41) of D. Tsuna et al. (2024) suggests that this early emission can span 20–30 days, comparable to the timescale of a small light curve feature observed immediately after discovery.

It is difficult to distinguish between a rapidly rotating massive star and one undergoing runaway mass loss onto a binary companion by geometric arguments alone. Both can produce slow and H-rich toroidal CSM ($\sim$400 km s^{-1}) and a faster and He-rich bipolar outflow ($\sim$1200 km s^{-1}). In the case of unstable mass transfer, however, the disk wind and CBO outflow expand along orthogonal axes of symmetry and are not expected to interact prior to explosion. This leads to an observational puzzle: if interaction with the toroidal material powers the second peak, how is emission delayed for over 250 days?

Interaction between the SN ejecta and the CBO can occur soon after core collapse, and prior to the interaction with the fast-moving disk wind. The rapidly expanding SN ejecta may quickly overrun the interaction region and instead trace the collision with the fast-moving CSM first. If this is the case, photons from the CBO interaction may be scattered through the secondary interaction region as they escape the photosphere and contribute to the total luminosity of the event. A reverse shock produced from the ejecta's collision with polar material should also propagate inward and drive additional collisions with the toroidal material, further powering a long-lived event. The complex inner interaction may only be revealed once the photosphere fully recedes. This scenario has already been proposed to explain the late-time interaction observed in some SNe IIn (e.g., N. Smith et al. 2011a).

The reconstructed mass-loss history and high CSM masses ($\sim 2\,M_\odot$ associated with each peak) suggest eruptive events rather than the steady disk winds proposed in the low-mass binary merger model developed by D. Tsuna et al. (2024). It is plausible that two long-lived pre-explosion outbursts, potentially from instabilities associated with the mass transfer, ejected fast-moving (1200–2200 km s^{-1}) polar material. The SN ejecta's interaction with each shell-like structure along the polar axis then powers the two distinct light curve peaks, and the SN–CSM shell velocity is lowered during the second peak by the ejecta's first collision. An inner H-rich disk or CBO may contribute additional luminosity throughout the two peaks.

If any CSM from either the CBO or the first polar shell is accelerated by the SN ejecta, it might also collide with the outermost polar material. Assuming the SN–CBO interaction occurs immediately after explosion and the material is accelerated to $\sim$2200 km s^{-1} (the faster CSM velocity calculated during the second peak), it would overrun the interaction photosphere at the first polar shell (which is expanding at $\sim$1200 km s^{-1} at a distance of $\sim 2 \times 10^{15}$ cm) $\sim$230 days after discovery in the rest frame. This is suspiciously close to the start of the second light curve peak, particularly given the uncertainty in the time of explosion. These ancillary interactions could compress the outer CSM to

---

[42] This estimate of the companion mass is also supported by the $\sim$linear scaling between the CSM and the accretor's mass suggested by the binary mass-transfer simulations of M. MacLeod & A. Loeb (2020a).

higher densities, and increase the energy budget available to power the second peak. For starting CSM shells of identical mass, this would naturally lead to the appearance of He II features from the extremely high-density ($n_e > 10^{13}\,\mathrm{cm}^{-3}$) interaction region during the second peak. This possibility reveals a potential limitation of our shock modeling: interaction between shells might systematically increase both the presumed CSM density at the time of explosion and the associated mass-loss rates inferred for the progenitor during the earlier outburst.

Finally, we cannot exclude an LBV-like primary in a binary system as the progenitor to 2023zkd. If an LBV outburst occurring during Precursor B is funneled in the polar direction by an H-rich disk formed during stable mass transfer, it could also produce two CSM interaction regions with distinct densities, compositions, and velocities. This scenario, however, must also explain the spectral evolution observed in 2023zkd. The H and He I features at +90d suggest the fast-moving CSM is more He-rich than the slow-moving CSM, contrary to expectations for an H-rich LBV outburst. The post-LBV primary could launch fast and He-rich winds as a WN after the outburst, but it is difficult to explain how the WN alone could enrich the polar regions with enough He-rich CSM to power interaction signatures spanning 200 days from mass loss in the single year between the start of Precursor B and the transient's discovery. The spectral sequence may alternatively be reconciled if the LBV outburst sweeps up and accelerates He-rich winds from the binary disk; but this would require a composition inversion (the He-rich material must be distributed along the poles before the H-rich LBV outburst occurs) and additional assumptions about the evolutionary history of the companion.

8.4. Final Remarks on the 2023zkd Progenitor

We summarize the key observational properties of 2023zkd and the evidence for and against the leading progenitor scenarios in Table 4 below.

From the above considerations, we conclude that a binary system with two main eruptive episodes that produce structured polar CSM and a slow equatorial outflow before merger is the most likely explanation for SN 2023zkd. The binary companion is likely to be a BH, or involve colliding stellar winds between binary components at luminosities without strong theoretical or observational support. We present a conceptual picture for this scenario at key phases in the pre- and post-explosion system in Figure 15, and note its strong similarity to the progenitor systems suggested by N. Smith (2017b), S. L. Schrøder et al. (2020; though our event suggests more structured polar outflows), and B. D. Metzger (2022).

In the model proposed by B. D. Metzger (2022), the tidal disruption and hyper-accretion of an He core onto a BH companion produces a luminous transient akin to an SN Ibn or SN IIn without requiring the core collapse of the primary. A massive, H-rich, slowly expanding disk surrounds the binary as a relic of its common-envelope evolution stage (with additional toroidal enrichment from a CBO) and the merger is preceded by H-depleted outflows that expand along the polar axis at $\sim 1000\,\mathrm{km\,s^{-1}}$. The observation of SN 2023zkd as an SN IIn with spectral similarities to an SN Ibn, together with its evidence for equatorially distributed H, would then suggest that SN 2023zkd occurred within 10^3–10^4 yr of the initial mass-transfer phase that tightens the binary.

Though the rise of Precursor B suggests a connection to the final mass-transfer phase, the density profile derived in Section 7.2 indicates that the major mass-loss episodes occurred during Precursor A. Multiple mass-loss mechanisms could power this emission. One is periastron passage of the stellar companion along an eccentric orbit (J. T. Layton et al. 1998; E. Regös et al. 2005), which can accelerate accretion as the companion sweeps through material surrounding the primary (with the orbit's effects on the disk geometry able to drive additional mass loss; D. J. Muñoz & D. Lai 2016). Given the likely polar geometry of the emission, however, it is reasonable to consider outbursts not just from the progenitor star but from the disk itself.

Accretion disk outflows will naturally be oriented toward the polar direction (R. Fernández et al. 2015). Local temperature changes in a hydrogen-rich and convective accretion disk can also drive transitions between ionization modes (from ionized to neutral or neutral to ionized). This transitionary stage is well known to be both thermally and viscously unstable (see J. M. Hameury 2020 for a recent review, and their Figure 1 for the stability criteria associated with each mode), and can power luminous outbursts exhibiting distinct timescales and color temperatures. These modes may explain Precursor A and Precursor B in one self-consistent framework, particularly if the enhanced accretion rates associated with one mode are causally connected to the merger that produces the SN. Thermal-viscous instabilities have been explored for H-rich disks around low-mass binaries (to explain the primary outburst modes of dwarf novae, e.g., S. Mineshige 1986; D. A. Bollimpalli et al. 2018), but little work has been done to investigate their relevance for high-mass binaries such as the putative progenitor to 2023zkd. Very recent work has shown that angular momentum transport from polar disk-driven outflows, in particular, can dramatically impact the orbital separation of a binary and the stability of its associated mass transfer (R. Willcox et al. 2023; M. Gallegos-Garcia et al. 2024). Additional effort on the simulation front is needed to explore whether these effects can reconcile the properties of Precursor A and B (and the geometry of the CSM at the time of explosion).

We have refrained from strongly speculating about the primary component of the progenitor system in the above analysis. Nonetheless, here we note a potential analog to the proposed progenitor system in high-mass X-ray binaries (HMXBs). HMXBs consist of a $>10\,M_\odot$ primary and a black hole or a neutron star companion. Galactic HMXBs undergo accretion-induced instabilities that can produce CSM distributed in a disk around the primary or along the polar axis around the accreting companion (A. Bahramian & N. Degenaar 2023). The circumstellar disk of a Be star can also exhibit double-peaked emission profiles in He I and He II from the star's rotational velocity (as in, e.g., MWC 656; optical line profiles associated with the system are shown in Figure 1 from R. K. Zamanov et al. 2022). Further, outburst modes from the system (actively debated as originating from thermal disk instabilities, periastron passages, X-ray heating, or interaction of accreting material with the compact object's magnetosphere in the case of a neutron star; A. Bahramian & N. Degenaar 2023) have been observed with emission varying over both month- and ∼year-long timescales (e.g., the optical/UV light curve of the Galactic HMXB Swift J0243.6+6124, shown in Figure 1 of J. Alfonso-Garzón et al. 2024).

Table 4
Summary of Candidate Progenitor Scenarios for SN 2023zkd (See the Text for Details)

Observation	Single LBV-like or WN Star	Single WNh Star	Interacting Binary
Precursor Luminosity	× $M_r \approx -15$ mag is ~3 mag above known giant outbursts (a).	× Requires extreme, super-Eddington mass loss for >100 $M_\odot$ star(d).	✓ Super-Eddington accretion onto BH naturally yields $L > 10^{39}$ erg s^{-1} (i)(l).
	✓ Blackbody properties of Precursor B are consistent with an LBV outburst (g).	…	…
Precursor Timescales	? LBV outbursts are diverse (g).	✓ Explains Precursor B's blackbody properties as terminal LBV-like outburst(c).	✓ Runaway mass transfer increasing luminosity spanning years (l).
…	…	? No known mechanism for sustaining super-Eddington outflows for years.	…
Ejecta & CSM Masses	? W-R wind rates (10^{-6}–10^{-4} $M_\odot$ yr^{-1}) require $\gtrsim 10^4$ yr to produce ~ 5 $M_\odot$ of CSM; giant outbursts are possible (f)(m).	? Similar challenges to the LBV/WN scenario; fine-tuning needed to reach $M_{\rm CSM} \approx 5$ $M_\odot$.	✓ Binary mass transfer can easily eject multiple $M_\odot$ of material (h)(l).
CSM Geometry, Composition	✓ Can produce bipolar & toroidal CSM for near-critical rotators, even in a single outburst (b)(c).	✓ Produces fast, He-rich CSM and slow H-rich CSM.	✓ Naturally explains slow (200–400 km s^{-1}) H-rich torus & fast (1200–2200 km s^{-1}) He-rich polar outflow (h)(l).
Spectral Evolution	× Persistent, multicomponent H and He lines require strong mixing of CSM from LBV outburst & WN wind.	? May explain persistent H & He if near-critical rotation leads to explosion as a post-WN LBV.	✓ Matches double-peaked profiles (j).
			✓Stable RLOF phase can leave residual H envelope in low-Z systems (k).
			✓Exact composition sensitive to evolutionary state at the time of final CCSN/merger.
…	…	…	
…	…	…	

References. (a) R. M. Humphreys & K. Davidson (1994); (b) J. P. Cassinelli & R. Ignace (1997); (c) G. Garcia-Segura et al. (1997); (d) N. Smith & P. S. Conti (2008); (e) N. Smith et al. (2011a); (f) N. Smith (2017b); (g) N. Smith (2017a); (h) M. MacLeod et al. (2018a); (i) M. Brightman et al. (2019); (j) A. Suzuki et al. (2019); (k) E. Laplace et al. (2020); (l) D. Tsuna et al. (2024); (m) C. L. Ransome & V. A. Villar (2025)

Though the inefficient accretion rates suggested by some black hole–Be star HMXBs may drive X-ray quiescence in a progenitor system (and optical variability has been seen in some BeXRBs without coincident X-rays; M. J. Coe et al. 2023), the X-ray luminosities observed in even the most-luminous HMXB outbursts are still dimmer than the optical precursor observed in 2023zkd. Our binned detections at $\sim 10^{41}$ erg s^{-1} are more comparable to Ultraluminous X-ray Sources (ULXs), e.g., M101-X1 (a system with a putative W-R primary and ~ 10 $M_\odot$ black hole companion inferred from kinematic modeling; R. F. Shen et al. 2015) and MCG-03-34 (whose X-ray luminosities are comparable to the optical luminosity of Precursor A G. Miniutti et al. 2006). ULXs have recently been shown to exhibit long-lived variability at UV wavelengths (N. Khan & M. J. Middleton 2023), and systematic optical searches for additional variability have recently begun (S. Allak et al. 2022).

There is substantial observational overlap between HMXBs/ULXs and SNe IIn regardless of whether a causal link exists: the optical spectra of ULXs might be able to mimic LBVs and W-Rs due to their fast, hydrogen-rich disk winds (S. Fabrika et al. 2015), and the composite spectrum from a strong accretion phase may mimic that of a young SN IIn (S. Fabrika et al. 2015). Nonetheless, a ULX-like progenitor was very recently proposed to explain periodic variations in the post-explosion light curve for the stripped-envelope SN 2020jli (P. Chen et al. 2024). There may be additional similarities between the physical environments of XRBs and the progenitors of long-lived and multipeaked SNe IIn; we consider this a promising avenue of future research.

9. Conclusion

We have presented photometric and spectroscopic observations of the double-peaked and helium-rich type IIn SN 2023zkd. We describe the most significant properties of the explosion from our analysis below:

1. A host galaxy with a mass at the lowest end of the distribution of observed SN IIn hosts ($M_* \approx 10^8$ $M_\odot$), and with negligible (~ 0.01 $M_\odot$ yr^{-1}) ongoing global star formation;
2. A double-peaked photometric evolution, with the event reaching an r-band maximum of $M_r \approx -18.7$ mag at the first peak and $M_r \approx -18.4$ mag at a second, concave-down peak ~224 days later (in the rest frame), followed by a rapid (~60 days) dimming and associated reddening to $g - r > 1$;
3. A precursor phase characterized by persistent (~1500 days) and luminous ($M_r \approx -15$ mag) emission, a final ~400 days ramp-up to event discovery;
4. Multicomponent, asymmetric Balmer and He I emission features that evolve minimally from the decline of the first light curve peak through the decline of the second; fits to the Hα profiles of the dominant line-emitting region suggest CSM velocities starting at ~1170 km s^{-1} at +90 days and reaching ~1800 km s^{-1} at the conclusion of the secondary brightening phase. Fits to the P-Cygni absorption of the Hβ profiles indicate an SN–CSM shell velocity decreasing from ~4700 km s^{-1} at +90 days to

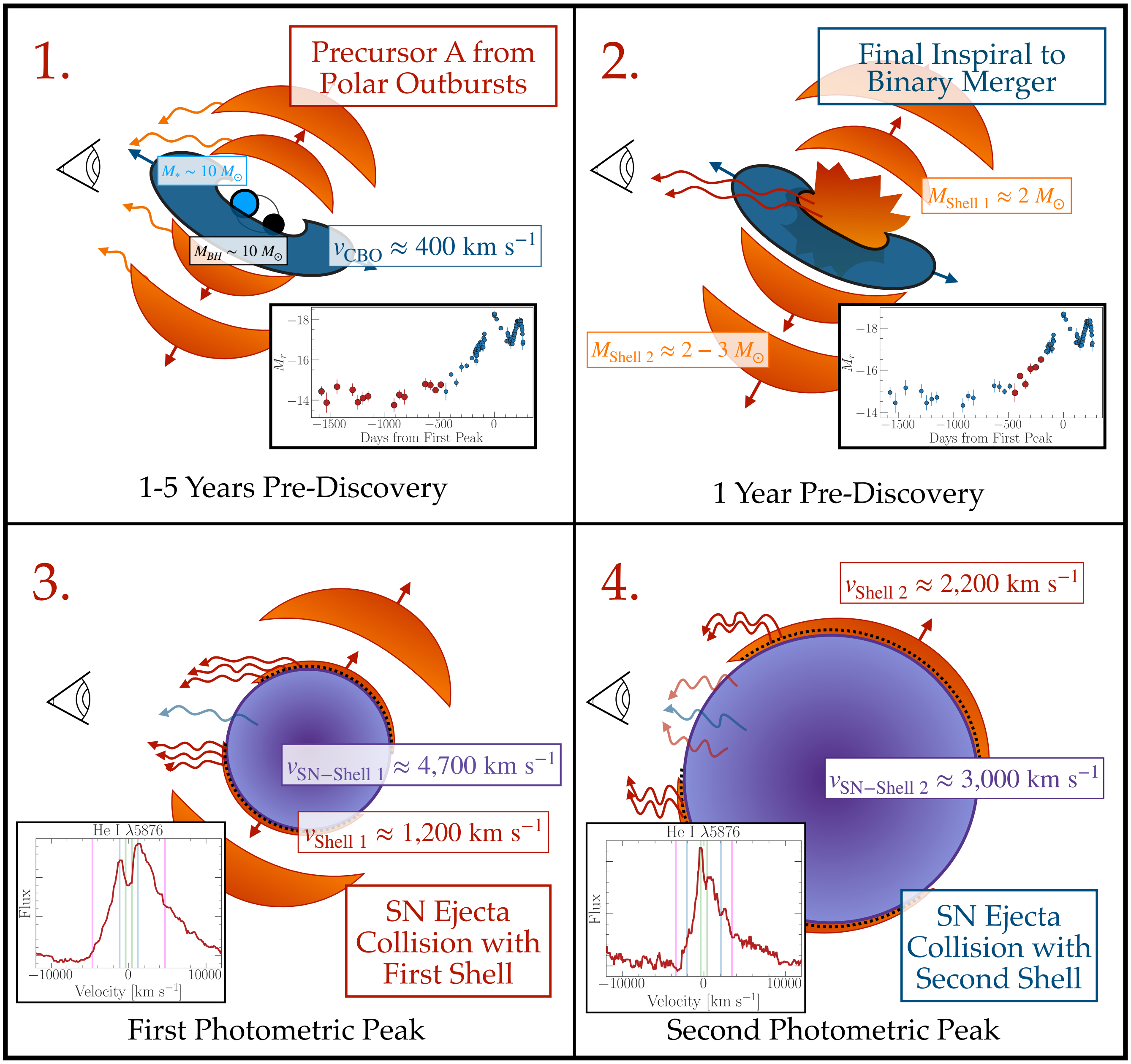

Figure 15. The proposed evolution of the putative binary system associated with SN 2023zkd. 1. From 1–5 yr before discovery, photometric variability (red points) is detected from two polar pre-merger outbursts that each eject $\sim 2\,M_\odot$ from the system. 2. During the final year pre-explosion, runaway accretion leads to a tightening of the binary. The early photometric rise (red points) is associated either with unstable and enhanced accretion onto the black hole following a tightening of the binary, or an LBV-like outburst from the primary star. 3. The primary merges with the black hole companion and explodes. The dense equatorial CBO funnels the ejecta along the polar axis and into the fast-moving, He-rich polar shells. Interaction with the first shell powers the first light curve peak, and He I profiles are seen in double-peaked emission at the shell velocity (magenta). 4. Interaction with the second polar shell powers the second light curve peak, with potential additional luminosity provided by CBO-interaction photons that scatter through the cooling shell (causing a peak in the He I profiles at the CBO velocity in green). The transient rapidly dims when the SN interaction shell reaches the edge of the outer polar material.

$\sim$2800 km s^{-1} at the conclusion of the secondary peak; a slow-moving and persistent ($\sim$400 km s^{-1}) CSM component is also detected that contributes to the observed luminosity of the secondary peak;

5. A double-peaked emission profile for He I lines in the +90 day spectrum, with emission peaks at the CSM velocity; this strongly suggests an axisymmetric outflow whose interaction with the SN ejecta powers the first photometric peak;
6. A mass-loss history characterized by maximum mass ejection rates $\sim$1–2 yr and $\sim$3 yr prior to discovery, with a total CSM mass of 5–6 $M_\odot$ ejected in comparable proportions during each mass-loss episode;
7. A low Balmer decrement of $\sim$2.0 at +90 days and 1.3–1.7 at all subsequent spectra, suggesting collisional excitation in an extremely high-density plasma ($n_e > 10^{13}$ cm^{-2}) comparable to the material powering the 2012-B brightening of 2009ip;
8. An Hα/He I λ5876 ratio of 2–5, intermediate between He-rich SNe IIn (1996al, 2021adou, 2016jbu) and the growing sample of transitional SNe IIn/Ibn (2011hw, 2021foa, 2020bqj, 2005la, and iPTF15akq).

The above properties are well matched to a merger-driven explosion between an $M_{\rm ZAMS} > 30\,M_\odot$ He core and an $\sim 10\,M_\odot$ black hole companion following years of unstable mass transfer. Interestingly, our analysis suggests that the peak in the progenitor system's mass-loss rate does not coincide with the more-luminous precursor event (Precursor B), and instead may be associated with the lower-luminosity, longer-lived pre-explosion emission (Precursor A). This finding may naturally explain why two eruptive episodes are suggested by the mass-loss histories of multiple double-peaked SNe IIn, but the majority of pre-explosion detections suggest only a single brightening phase in the progenitor's final year (this includes 2021qqp; D. Hiramatsu et al. 2024b; 2016jbu; S. J. Brennan et al. 2022; 2019zrk; C. Fransson et al. 2022; among others). Caution should be taken in interpreting the months-long precursor emission detected in some SNe IIn (e.g., N. L. Strotjohann et al. 2021). Decade-long photometric baselines will allow us to confirm luminous emission at a secondary pre-explosion phase for the most nearby double-peaked SNe; if a secondary outburst is not observed, it will force us to critically re-examine the photometric signposts of pre-explosion mass loss.

The shock models employed in this work are one-zone, and assume that the luminosity of the explosion at a given phase can be explained by CSM interaction at a single radius. As our spectral sequence for SN 2023zkd reveals, the reality can be significantly more complicated. Future studies will require more sensitive probes of CSM geometry, aided both by multizone models and theoretical studies of unstable mass loss in single and binary systems, to be able to more reliably follow the thread of circumstellar interaction back to a likely progenitor system.

Our final conceptual picture for the progenitor system of 2023zkd is supported by the existence of a partially resolved, low-velocity narrow component observed in hydrogen and helium at the decline of both light curve peaks. This feature has been observed in multiple other SNe IIn. In cases where this component is completely blended with the other velocity components, it is reasonable to expect that only the higher-velocity CSM can be identified. Conversely, in cases where both a narrow and an intermediate-width components are seen, the intermediate-width component may be mistakenly attributed to radiative or collisional acceleration of a portion of the same slow-moving CSM. These dramatic differences in interpretation may be to blame for some of the scatter in CSM velocities reported for archival SNe IIn (which span 100–1000 km s^{-1}; C. L. Ransome & V. A. Villar 2025). Alternatively, it may be the case that the multicomponent geometry associated with 2023zkd is uncommon among SNe IIn.

If higher-resolution spectroscopy confirms the presence of equatorial CSM in an upcoming strongly interacting SN IIn, the structure of that profile over time can shed light on its evolution and fate (including whether it is fully destroyed or only partially disrupted by the SN ejecta). These data will allow us to answer more targeted questions about the explosion than have been possible in many other areas of SN science. The spectra of strongly interacting SNe are substantially more complex than those of noninteracting SNe: electron scattering, asymmetric/clumpy CSM, dust formation, and differences in line intensities spanning wide dynamic ranges in optical depth, composition, and temperature may all produce ambiguous structure at small wavelength scales. High-resolution spectroscopy is critical for disentangling these physical effects.

The final photometry associated with 2023zkd suggests that the interaction shell had overrun the CSM whose interaction powered the second light curve peak. Nevertheless, if the SN ejecta or one of the polar shells is able to maintain its density structure and velocity, additional re-brightening phases may be possible. We advocate for continued multiwavelength monitoring of this explosion to further constrain the properties of the CSM and confirm both a core-collapse explosion and a binary origin. Given the complex geometry and high inferred CSM masses, SN 2023zkd is also a prime target for late-time studies of dust formation at NIR wavelengths with JWST (J. P. Gardner et al. 2006) and the Nancy Grace Roman Space Telescope (R. Akeson et al. 2019; e.g., O. D. Fox et al. 2011, 2021).

Photometric samples of SNe IIn will dramatically increase in 2025, with the advent of the Vera C. Rubin Observatory's Legacy Survey for Space and Time expected to discover $\sim 10^5\ \mathrm{yr}^{-1}$ (C. L. Ransome & V. A. Villar 2025). Algorithms designed to flag these long-lived and re-brightening transients will play a critical role in characterizing the full breadth of strongly interacting events. Future studies of the phases and phenomenology of pre-explosion emission will be equally valuable for probing the progenitor system in its final years, although seasonal gaps combined with the relatively low single-band cadence of LSST data will present additional challenges in reconstructing a physical picture.

Acknowledgments

We thank Edo Berger, Stan Woosley, Seán Brennan, Monica Gallegos-Garcia, Peter Blanchard, Harsh Kumar, Brian Metzger, and Kevin Burdge for helpful conversations that improved this manuscript. We additionally thank Yuri Beletsky and Dave Osip for obtaining the spectroscopic observations of SN 2023zkd with Magellan/LDSS-3. Finally, we are indebted to the National Institute of Standards and Technology (NIST); their H and He line lists have proven invaluable for a thorough analysis of the spectroscopic sequence of SN 2023zkd.

This work is supported by the National Science Foundation under Cooperative Agreement PHY-2019786 (The NSF AI-Institute for Artificial Intelligence and Fundamental Interactions, http://iaifi.org/). A.G. also acknowledges support from the AI Institutes Virtual Organization (AIVO) and the MIT Libraries. The Villar Astro Time Lab acknowledges support through the David and Lucile Packard Foundation, National Science Foundation under AST-2433718, AST-2407922 and AST-2406110, as well as an Aramont Fellowship for Emerging Science Research. C.R.A. is supported by the European Research Council (ERC) under the European Union's Horizon 2020 research and innovation program (grant agreement No. 948381) D.O.J. acknowledges support from NSF grants AST-2407632 and AST-2429450, NASA grant 80NSSC24M0023, and HST/JWST grants HST-GO-17128.028, HST-GO-16269.012, and JWST-GO-05324.031, awarded by the Space Telescope Science Institute (STScI), which is operated by the Association of Universities for Research in Astronomy, Inc., for NASA, under contract NAS5-26555. Parts of this research were supported by the Australian Research Council Centre of Excellence for Gravitational Wave Discovery (OzGrav), through project

No. CE230100016. D.T. is supported by the Sherman Fairchild Postdoctoral Fellowship at Caltech. K.A.B. is supported by an LSST-DA Catalyst Fellowship; this publication was thus made possible through the support of Grant 62192 from the John Templeton Foundation to LSST-DA. D.F. is supported by a VILLUM FONDEN Young Investigator Grant (VIL25501). The UCSC team is supported in part by a fellowship from the David and Lucile Packard Foundation to R.J.F. C.G. is supported by research grants (VIL25501 and VIL69896) from VILLUM FONDEN. The LCO group is supported by NSF grants AST-1911225 and AST-1911151. This work makes use of data from the Las Cumbres Observatory global telescope network. M.M. gratefully acknowledges support from a Clay Postdoctoral Fellowship of the Smithsonian Astrophysical Observatory. G.N. gratefully acknowledges NSF support from a CAREER grant, AST-2239364, supported in part by funding from Charles Simonyi, AST-2206195, OAC-2311355, and AST-2432428. G.N. and the NSF-Simons AI-Institute for the Sky (SkAI) are supported via NSF AST-2421845 and Simons Foundation MPS-AI-00010513. This work was partially performed at the NSF-Simons SkAI Institute. G.N. is also supported by the DOE through the Department of Physics at the University of Illinois, Urbana-Champaign (No. 13771275), and support from the HST Guest Observer Program through HST-GO-16764 and HST-GO-17128 (PI: R. Foley). K.W.S. acknowledges funding from the Royal Society. Q.W. is supported by the Sagol Weizmann-MIT Bridge Program. This work is supported by research grants (VIL16599,VIL54489) from VILLUM FONDEN.

The Young Supernova Experiment (YSE) and its research infrastructure is supported by the European Research Council under the European Union’s Horizon 2020 research and innovation program (ERC grant agreement 101002652, PI K. Mandel), the Heising-Simons Foundation (2018-0913, PI R. Foley; 2018-0911, PI R. Margutti), NASA (NNG17PX03C, PI R. Foley), NSF (AST–1720756, AST–1815935, PI R. Foley; AST–1909796, AST-1944985, PI R. Margutti), the David & Lucille Packard Foundation (PI R. Foley), VILLUM FONDEN (project 16599, PI J. Hjorth), and the Center for AstroPhysical Surveys (CAPS) at the National Center for Supercomputing Applications (NCSA) and the University of Illinois Urbana-Champaign.

Pan-STARRS is a project of the Institute for Astronomy of the University of Hawaii, and is supported by the NASA SSO Near Earth Observation Program under grants 80NSSC18K0971, NNX14AM74G, NNX12AR65G, NNX13AQ47G, NNX08AR22G, and 80NSSC21K1572, and by the State of Hawaii. The Pan-STARRS1 Surveys (PS1) and the PS1 public science archive have been made possible through contributions by the Institute for Astronomy, the University of Hawaii, the Pan-STARRS Project Office, the Max-Planck Society and its participating institutes, the Max Planck Institute for Astronomy, Heidelberg and the Max Planck Institute for Extraterrestrial Physics, Garching, The Johns Hopkins University, Durham University, the University of Edinburgh, the Queen’s University Belfast, the Harvard-Smithsonian Center for Astrophysics, the Las Cumbres Observatory Global Telescope Network Incorporated, the National Central University of Taiwan, STScI, NASA under grant NNX08AR22G issued through the Planetary Science Division of the NASA Science Mission Directorate, NSF grant AST-1238877, the University of Maryland, Eotvos Lorand University (ELTE), the Los Alamos National Laboratory, and the Gordon and Betty Moore Foundation.

Based on observations obtained at the international Gemini Observatory, a program of NSF NOIRLab, which is managed by the Association of Universities for Research in Astronomy (AURA) under a cooperative agreement with the U.S. National Science Foundation on behalf of the Gemini Observatory partnership: the U.S. National Science Foundation (United States), National Research Council (Canada), Agencia Nacional de Investigación y Desarrollo (Chile), Ministerio de Ciencia, Tecnologìa e Innovación (Argentina), Ministério da Ciência, Tecnologia, Inovações e Comunicações (Brazil), and Korea Astronomy and Space Science Institute (Republic of Korea). Data were taken by program GN-2024A-Q-136. This work was enabled by observations made from the Gemini-North telescope, located within the Maunakea Science Reserve and adjacent to the summit of Maunakea. We are grateful for the privilege of observing the Universe from a place that is unique in both its astronomical quality and its cultural significance.

A major upgrade of the Kast spectrograph on the Shane 3 m telescope at Lick Observatory was made possible through generous gifts from the Heising-Simons Foundation as well as William and Marina Kast. Research at Lick Observatory is partially supported by a generous gift from Google.

This work makes use of data from the Las Cumbres Observatory global telescope network. The LCO group is supported by NSF grants AST-1911225 and AST-1911151.

This work has made use of data from the Asteroid Terrestrial-impact Last Alert System (ATLAS) project. The Asteroid Terrestrial-impact Last Alert System (ATLAS) project is primarily funded to search for near earth asteroids through NASA grants NN12AR55G, 80NSSC18K0284, and 80NSSC18K1575; byproducts of the NEO search include images and catalogs from the survey area. This work was partially funded by Kepler/K2 grant J1944/80NSSC19K0112 and HST-GO-15889, and STFC grants ST/T000198/1 and ST/S006109/1. The ATLAS science products have been made possible through the contributions of the University of Hawaii Institute for Astronomy, the Queen’s University Belfast, the Space Telescope Science Institute, the South African Astronomical Observatory, and The Millennium Institute of Astrophysics (MAS), Chile.

The ZTF forced photometry service was funded under the Heising-Simons Foundation grant No. 12540303 (PI: Graham).

This publication makes use of data products from the Two Micron All Sky Survey, which is a joint project of the University of Massachusetts and the Infrared Processing and Analysis Center/California Institute of Technology, funded by the National Aeronautics and Space Administration and the National Science Foundation.

Funding for the Sloan Digital Sky Survey IV has been provided by the Alfred P. Sloan Foundation, the U.S. Department of Energy Office of Science, and the Participating Institutions. SDSS-IV acknowledges support and resources from the Center for High Performance Computing at the University of Utah. The SDSS website is www.sdss4.org. SDSS-IV is managed by the Astrophysical Research Consortium for the Participating Institutions of the SDSS Collaboration including the Brazilian Participation Group, the Carnegie Institution for Science, Carnegie Mellon University, Center for Astrophysics | Harvard & Smithsonian, the Chilean Participation Group, the French Participation Group, Instituto de Astrofísica de Canarias, The Johns Hopkins University, Kavli Institute for the Physics and Mathematics of the Universe (IPMU)/University of Tokyo, the Korean Participation Group, Lawrence Berkeley National Laboratory, Leibniz Institut für Astrophysik Potsdam (AIP), Max-Planck-Institut für Astronomie (MPIA Heidelberg), Max-Planck-Institut für Astrophysik (MPA Garching), Max-Planck-Institut für Extraterrestrische Physik (MPE), National Astronomical Observatories of China, New Mexico State University, New York University, University of Notre Dame, Observatário Nacional/MCTI, The Ohio State University, Pennsylvania State University, Shanghai Astronomical Observatory, United Kingdom Participation Group, Universidad Nacional Autónoma de México, University of Arizona, University of Colorado Boulder, University of Oxford, University of Portsmouth, University of Utah, University of Virginia, University of Washington, University of Wisconsin, Vanderbilt University, and Yale University. Collaboration Overview Affiliate Institutions Key People in SDSS Collaboration Council Committee on Inclusiveness Architects SDSS-IV Survey Science Teams and Working Groups Code of Conduct SDSS-IV Publication Policy How to Cite SDSS External Collaborator Policy For SDSS-IV Collaboration Members.

The Legacy Surveys consist of three individual and complementary projects: the Dark Energy Camera Legacy Survey (DECaLS; Proposal ID No. 2014B-0404; PIs: David Schlegel and Arjun Dey), the Beijing-Arizona Sky Survey (BASS; NOAO Prop. ID No. 2015A-0801; PIs: Zhou Xu and Xiaohui Fan), and the Mayall *z*-band Legacy Survey (MzLS; Prop. ID No. 2016A-0453; PI: Arjun Dey). DECaLS, BASS, and MzLS together include data obtained, respectively, at the Blanco telescope, Cerro Tololo Inter-American Observatory, NSF's NOIRLab; the Bok telescope, Steward Observatory, University of Arizona; and the Mayall telescope, Kitt Peak National Observatory, NOIRLab. Pipeline processing and analyses of the data were supported by NOIRLab and the Lawrence Berkeley National Laboratory (LBNL). The Legacy Surveys project is honored to be permitted to conduct astronomical research on Iolkam Du'ag (Kitt Peak), a mountain with particular significance to the Tohono O'odham Nation. NOIRLab is operated by the Association of Universities for Research in Astronomy (AURA) under a cooperative agreement with the National Science Foundation. LBNL is managed by the Regents of the University of California under contract to the U.S. Department of Energy. This project used data obtained with the Dark Energy Camera (DECam), which was constructed by the Dark Energy Survey (DES) collaboration. Funding for the DES Projects has been provided by the U.S. Department of Energy, the U.S. National Science Foundation, the Ministry of Science and Education of Spain, the Science and Technology Facilities Council of the United Kingdom, the Higher Education Funding Council for England, the National Center for Supercomputing Applications at the University of Illinois at Urbana-Champaign, the Kavli Institute of Cosmological Physics at the University of Chicago, Center for Cosmology and Astro-Particle Physics at the Ohio State University, the Mitchell Institute for Fundamental Physics and Astronomy at Texas A&M University, Financiadora de Estudos e Projetos, Fundacao Carlos Chagas Filho de Amparo, Financiadora de Estudos e Projetos, Fundacao Carlos Chagas Filho de Amparo a Pesquisa do Estado do Rio de Janeiro, Conselho Nacional de Desenvolvimento Cientifico e Tecnologico and the Ministerio da Ciencia, Tecnologia e Inovacao, the Deutsche Forschungsgemeinschaft and the Collaborating Institutions in the Dark Energy Survey. The Collaborating Institutions are Argonne National Laboratory, the University of California at Santa Cruz, the University of Cambridge, Centro de Investigaciones Energeticas, Medioambientales y Tecnologicas-Madrid, the University of Chicago, University College London, the DES-Brazil Consortium, the University of Edinburgh, the Eidgenossische Technische Hochschule (ETH) Zurich, Fermi National Accelerator Laboratory, the University of Illinois at Urbana-Champaign, the Institut de Ciencies de l'Espai (IEEC/CSIC), the Institut de Fisica d'Altes Energies, Lawrence Berkeley National Laboratory, the Ludwig Maximilians Universitat Munchen and the associated Excellence Cluster Universe, the University of Michigan, NSF's NOIRLab, the University of Nottingham, the Ohio State University, the University of Pennsylvania, the University of Portsmouth, SLAC National Accelerator Laboratory, Stanford University, the University of Sussex, and Texas A&M University.

The Legacy Surveys imaging of the DESI footprint is supported by the Director, Office of Science, Office of High Energy Physics of the U.S. Department of Energy under contract No. DE-AC02-05CH1123, by the National Energy Research Scientific Computing Center, a DOE Office of Science User Facility under the same contract; and by the U.S. National Science Foundation, Division of Astronomical Sciences under contract No. AST-0950945 to NOAO.

The stellar population modeling in this work is based on data from the MILES library service developed by the Spanish Virtual Observatory in the framework of the IAU Commission G5 Working Group: Spectral Stellar Libraries.

YSE-PZ was developed by the UC Santa Cruz Transients Team with support from The UCSC team is supported in part by NASA grants NNG17PX03C, 80NSSC19K1386, and 80NSSC20K0953; NSF grants AST-1518052, AST-1815935, and AST-1911206; the Gordon & Betty Moore Foundation; the Heising-Simons Foundation; a fellowship from the David and Lucile Packard Foundation to R. J. Foley; Gordon and Betty Moore Foundation postdoctoral fellowships and a NASA Einstein fellowship, as administered through the NASA Hubble Fellowship program and grant HST-HF2-51462.001, to D.O.J.; and a National Science Foundation Graduate Research Fellowship, administered through grant No. DGE-1339067, to D.A.C.

Software: Astropy (Astropy Collaboration et al. 2013, 2018, 2022), BLAST (D. O. Jones et al. 2024), corner (D. Foreman-Mackey 2016), dust-extinction (K. D. Gordon et al. 2023), Matplotlib (J. D. Hunter 2007), Prospector (B. D. Johnson et al. 2021), Numpy (C. R. Harris et al. 2020), Pandas (pandas development team T. 2024), Scipy (P. Virtanen et al. 2020), Seaborn (M. L. Waskom 2021), sfdmap2,[43] SNANA (R. Kessler et al. 2009), and YSE-PZ (D. A. Coulter et al. 2022, 2023).

---

[43] https://github.com/AmpelAstro/sfdmap2

Appendix A
Confirming the ZTF Pre-discovery Flux Excess

Here, we evaluate the probability that the binned pre-explosion ZTF detections coincident with the SN site do not arise from the progenitor of SN 2023zkd. We define 10 evenly spaced positions along an annulus of radius 5″ centered on the SN position, and query the ZTF Forced Photometry Service for all flux measurements at these positions (while ensuring that these positions lie in the same field as SN 2023zkd and were observed with the same CCD). For each control light curve, we undertake the same analysis as for the SN 2023zkd light curve and calculate the uncertainty-weighted flux in 50 day bins spanning the same pre-explosion epochs. In each bin, we calculate the mean and standard deviation of the flux across all control light curves and use these values to convert the binned flux measurements for SN 2023zkd to *z*-scores (after combining the uncertainties of our control light curves and our precursor detections in quadrature). We show the results of this experiment in the top-left panel of Figure 16.

Note that 74% (25/34) of the reported pre-discovery detections for SN 2023zkd lie $\gtrsim 3\sigma$ above the distribution of binned background fluxes, and 24% (8/34) are at $>5\sigma$. The earliest $>5\sigma$ detection occurs at MJD ≈ 59029.4, 1194.3 days before first peak in the rest frame. This supports the marginal detection of excess flux in the case of Precursor A. We further note the potential presence of correlated structure in both filters in the 500 days prior to discovery, which we cannot clearly resolve in our final detections.

We can also calculate the probability that Precursor A is consistent with emission at a constant flux. We calculate the mean and standard deviation of binned flux values prior to MJD = 59850 in each filter and again convert the measured flux values to z-scores. The results are shown in the middle panel of Figure 16. All flux measurements are $<3\sigma$ from the mean flux (the most significant deviation is 2.3σ in ZTF-*g* and 1.3σ in ZTF-*r*), indicating that the photometric variability about the mean of Precursor A is statistically insignificant.

Finally, we calculate the statistical significance of the brightening associated with Precursor B. We calculate z-scores for each precursor detection relative to the mean and standard deviation of the flux measurements of Precursor A. The results are shown in the right panel of Figure 16. Two detections in ZTF-*g* and four detections in ZTF-*r* lie $>3\sigma$ above the mean flux of Precursor A; all occur in the 400 days prior to discovery and increase in significance prior to discovery (the final binned detection is $\sim 15\sigma$ above the precursor flux of Precursor A). The earliest statistically significant deviation from Precursor A occurs at MJD = 59873.4 in ZTF-*r* (395.1 days prior to first peak in the rest frame); as a result, we confirm the brightening of the progenitor system in its final year and mark the division between Precursor A and B at MJD ≈ 59873.

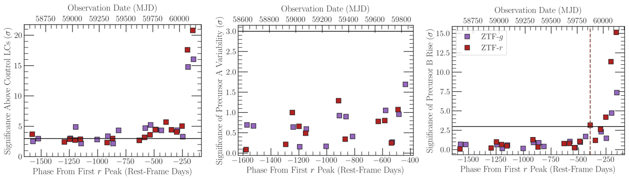

Figure 16. Left panel: statistical significance of binned pre-explosion photometry from the Zwicky Transient Facility (ZTF) in ZTF-*g* (purple) and ZTF-*r* (red) above the variability of control light curves surrounding the explosion site. The majority of measurements are at $>3\sigma$ significance (horizontal black line) in both filters. Middle panel: significance of variability during Precursor A about the mean flux (see the text for details). No measurements in either filter reach $>3\sigma$ significance, and we are unable to distinguish between multiple eruptions and persistent enhanced emission. Right panel: significance of flux measurements from Precursor B above the baseline flux for Precursor A. Multiple observations starting ~400 days from first peak (dashed vertical line) are statistically significant, suggesting a persistent rise in the year prior to event discovery.

Appendix B
Identification of SN 2023zkd as a Photometric Anomaly with `LAISS`

`LAISS` is a random forest classifier trained to distinguish between typical and atypical SNe on the basis of their photometric evolution and host-galaxy properties. We can interpret the predictions of the model using a force plot, which visualizes the approximate Shapley values associated with a candidate's features. Shapley values estimate the mean marginal contribution of each feature to a model output via additive feature attribution (see S. Lundberg & S.-I. Lee 2017). They were originally developed in the context of cooperative game theory but have seen widespread adoption in the field of machine learning interpretability (S. Hart 1989).

We use Shapley values to predict which features are most significant in determining the final anomaly score predicted for 2023zkd. We use the SHAP[44] package to calculate the Shapley values associated with SN 2023zkd's properties at MJD = 60327, the epoch when the event was originally flagged. Light curve properties have been calculated with the `light-curve` package (K. L. Malanchev et al. 2021) and the host-galaxy properties have been calculated with the `GHOST` package (A. Gagliano et al. 2021).

We show a force plot of the features with largest Shapley values in Figure 17. The Shapley values indicate that an anomaly label was assigned predominantly by the slope of a linear fit to the light curve across ZTF filters. This metric was also the single most important feature for distinguishing spectroscopic anomalies in P. D. Aleo et al. (2024), where it was attributed to the unique color evolution of relatively blue (e.g., I. Arcavi et al. 2014) and red (e.g., stripped-envelope SNe; F. Taddia et al. 2018; S. Khakpash et al. 2024) transients relative to the spectroscopically "normal" SNe Ia and SNe II. In this case, the dimming of ZTF-*g* after peak relative to ZTF-*r* is due to the prominent Hα emission feature that overlaps with ZTF-*r*, which dominates the luminosity of SNe IIn as the continuum fades. We will further explore `LAISS`'s ability to identify SNe with ongoing photometric signatures of CSM interaction in an upcoming work.

---

[44] https://shap.readthedocs.io/en/latest/index.html

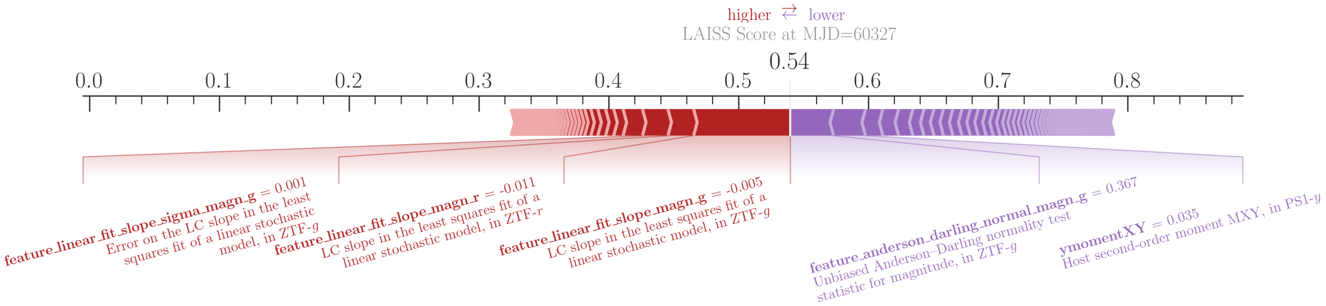

Figure 17. Force plot of SN 2023zkd for its properties on MJD ≈ 60327, when the event was first flagged by `LAISS`. Light curve and host-galaxy parameters with the largest positive Shapley values (indicating positive mean marginal contribution to the predicted anomaly score) are shown in red, and parameters with the largest negative values are shown in blue. The top positive Shapley features are the small negative linear slopes of ZTF-g and ZTF-r photometry, suggesting that an anomalous decline from first peak led to SN 2023zkd's identification as an unusual transient.

Appendix C
MOSFiT Corner Plot

Figure 18 shows the posterior samples after burn-in for the `MOSFiT` model fit to the second light curve peak (described in Section 7.1). The ejecta mass of the SN is fixed at $10\,M_{\odot}$, and the priors associated with each parameter are presented in Table 3.

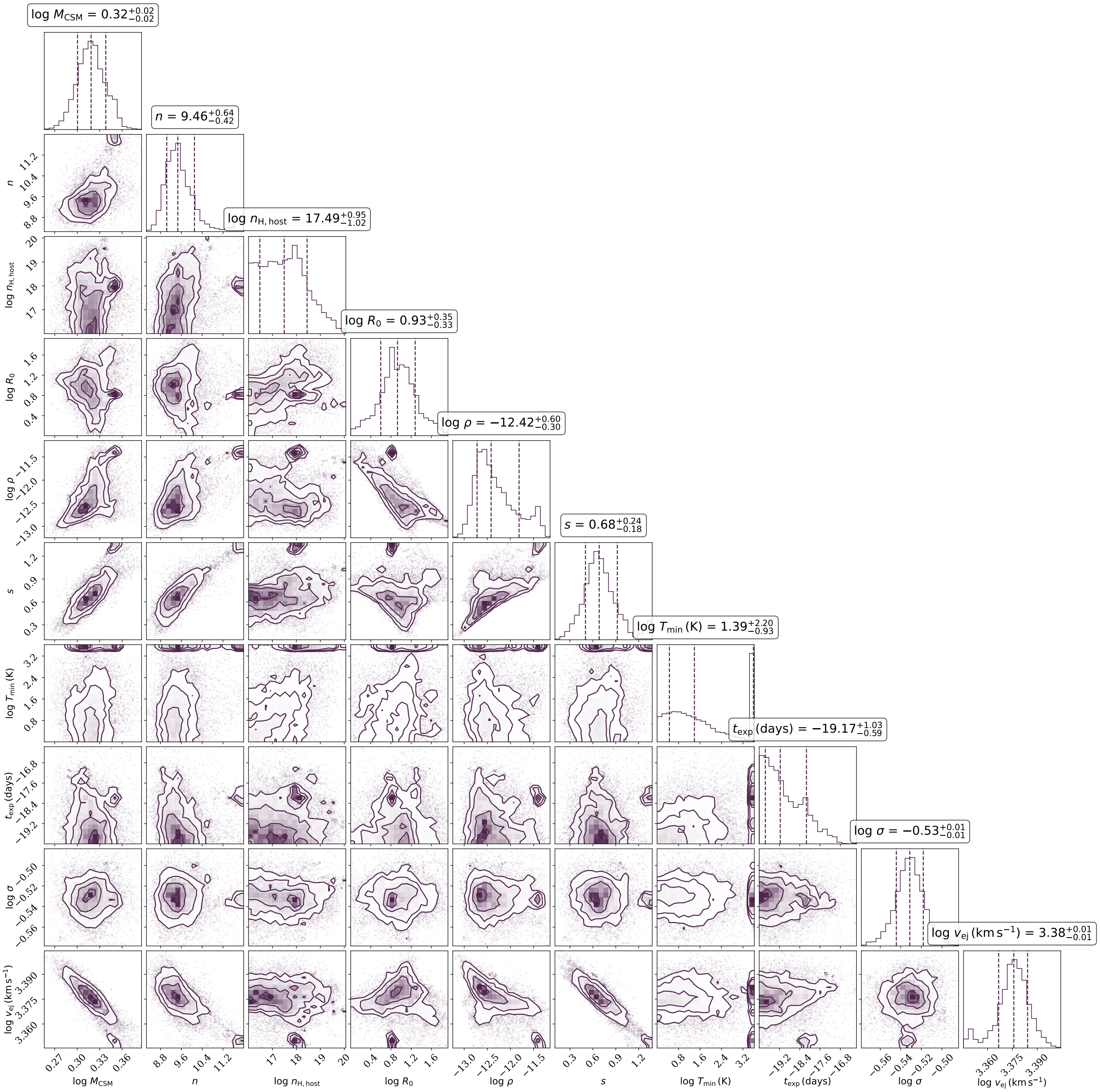

Figure 18. Posterior samples for the `MOSFiT` model fit to the event photometry associated with the second peak. Marginal distributions are shown at the top, with vertical lines corresponding to the median and 1σ range of the posteriors.

Appendix D
Prospector Corner Plot

Figure 19 shows the posterior samples for the `Prospector` model fit to the photometry and spectroscopy of SN 2023zkd's host galaxy. Details of the fitting procedure are provided in Section 3.

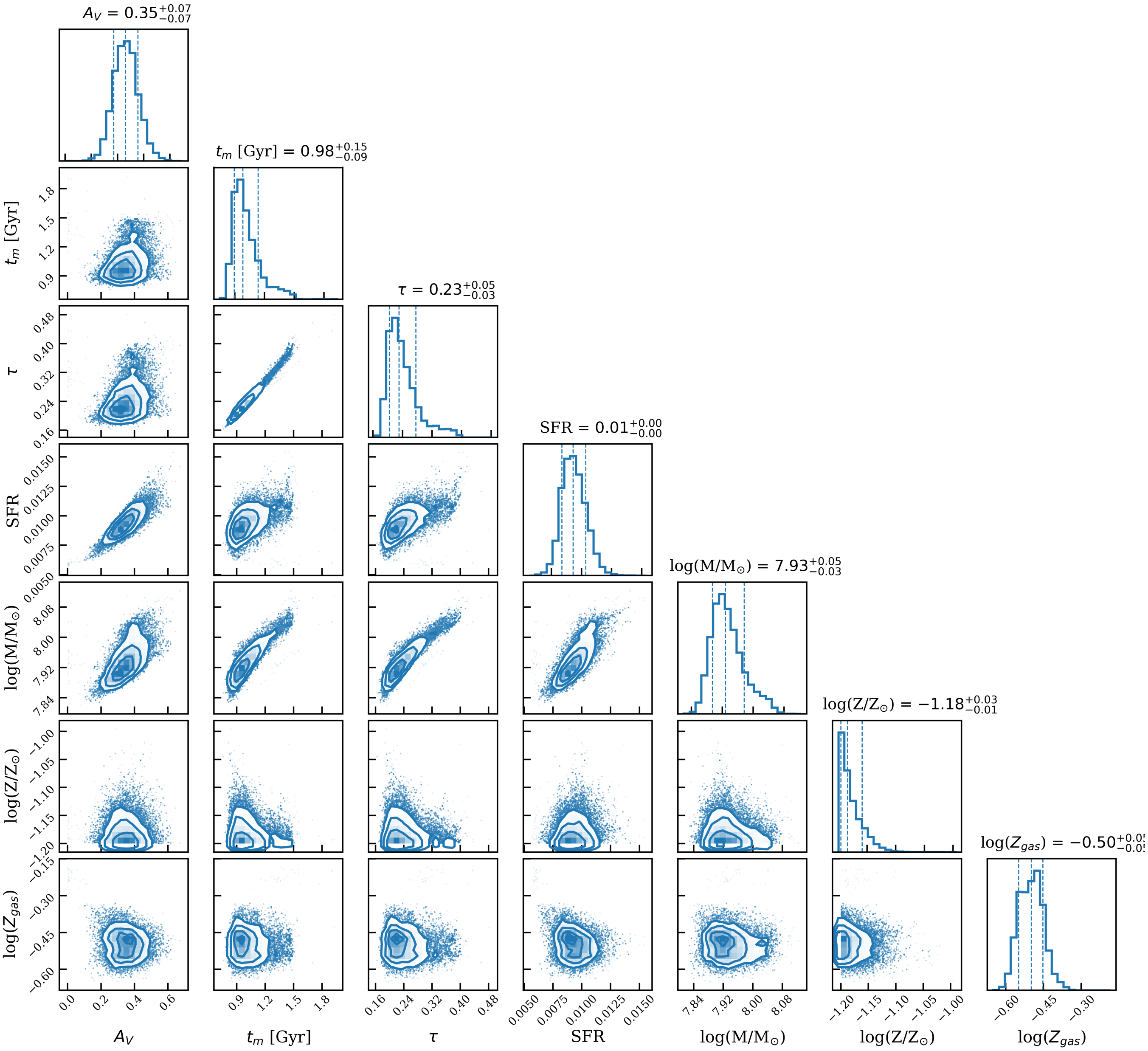

Figure 19. Posterior samples for the `Prospector` model fit to the host-galaxy photometry and spectroscopy. Marginal distributions are shown at the top, with vertical lines corresponding to the median and 1σ range of the posteriors.

Appendix E
Spectral Line Fitting Corner Plot

Figure 20 shows the posteriors associated with our continuum-subtracted line fit to He I λ5876 in the NOT/ALFOSC spectrum obtained on MJD = 60519 (+216 days relative to the observed r-band maximum at MJD = 60290.6). The variables μ and σ are in angstroms for each Gaussian component, while the amplitude A is in units of 10^{-17} erg $\mathrm{s}^{-1}\mathrm{cm}^{-2}$ Å^{-1}.

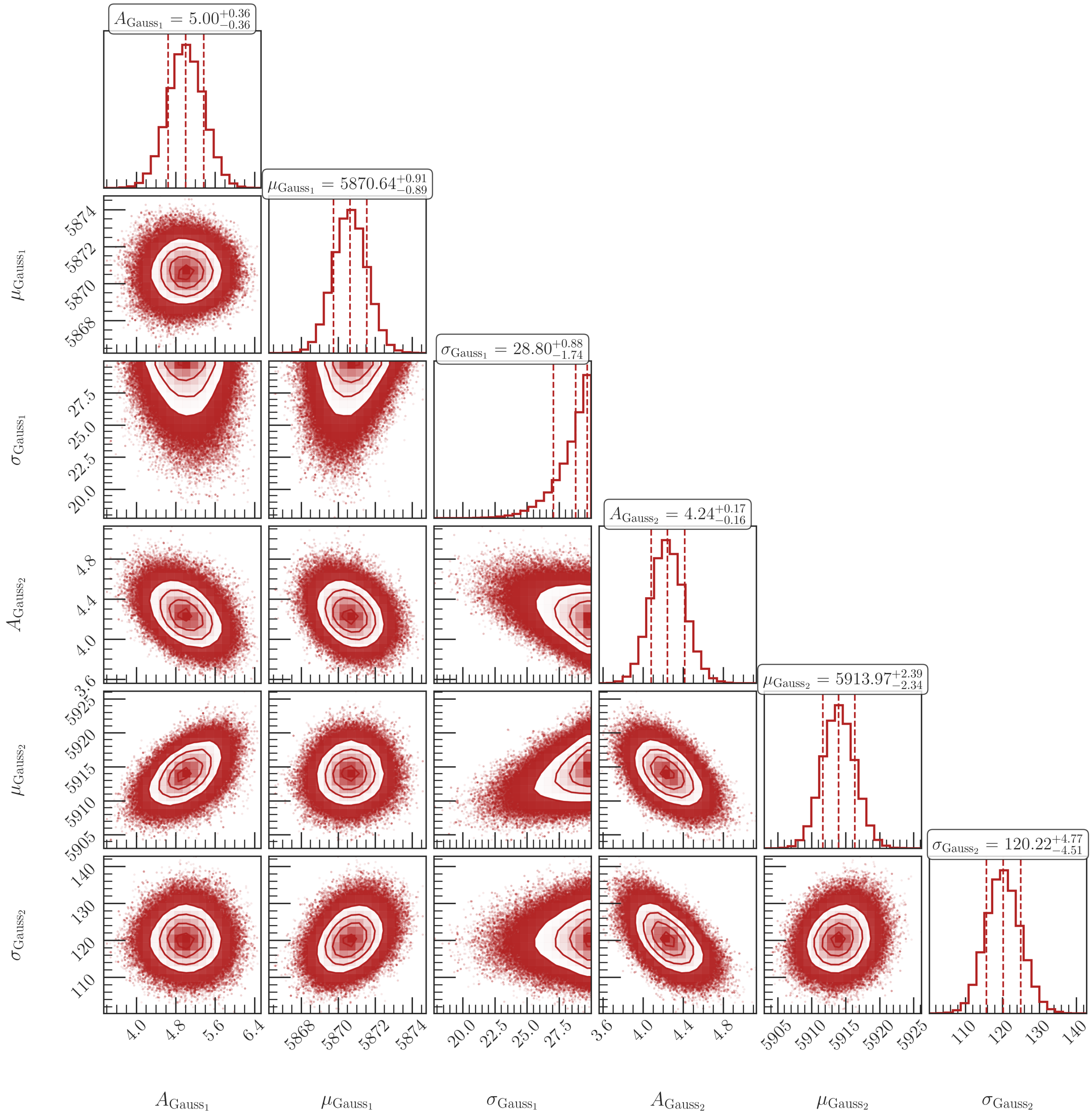

Figure 20. Corner plot showing the posteriors for the parameters corresponding to the continuum-subtracted He I λ5876 profile of the Magellan/LDSS-3 spectrum at MJD = 60519 (+216 days). The asymmetric profile is best fit by two Gaussian components parameterized by an amplitude A_{Gauss}, center μ_{Gauss}, and standard deviation σ_{Gauss}. The median and 1σ ranges of each parameter are shown as vertical dashed lines.

ORCID iDs

A. Gagliano https://orcid.org/0000-0003-4906-8447
V. A. Villar https://orcid.org/0000-0002-5814-4061
T. Matsumoto https://orcid.org/0000-0002-9350-6793
D. O. Jones https://orcid.org/0000-0002-6230-0151
C. L. Ransome https://orcid.org/0000-0003-4175-4960
A. E. Nugent https://orcid.org/0000-0002-2028-9329
D. Hiramatsu https://orcid.org/0000-0002-1125-9187
K. Auchettl https://orcid.org/0000-0002-4449-9152
D. Tsuna https://orcid.org/0000-0002-6347-3089
Y. Dong https://orcid.org/0000-0002-7937-6371
S. Gomez https://orcid.org/0000-0001-6395-6702
P. D. Aleo https://orcid.org/0000-0002-6298-1663
C. R. Angus https://orcid.org/0000-0002-4269-7999
T. de Boer https://orcid.org/0000-0001-5486-2747
K. A. Bostroem https://orcid.org/0000-0002-4924-444X
K. C. Chambers https://orcid.org/0000-0001-6965-7789
D. A. Coulter https://orcid.org/0000-0003-4263-2228
K. W. Davis https://orcid.org/0000-0002-5680-4660
J. Farah https://orcid.org/0000-0002-6886-269X
D. Farias https://orcid.org/0000-0002-6886-269X
R. J. Foley https://orcid.org/0000-0002-2445-5275
C. Gall https://orcid.org/0000-0002-8526-3963
H. Gao https://orcid.org/0000-0003-1015-5367
E. P. Gonzalez https://orcid.org/0000-0003-0209-9246
D. A. Howell https://orcid.org/0000-0003-4253-656X
M. E. Huber https://orcid.org/0000-0003-1059-9603
C. D. Kilpatrick https://orcid.org/0000-0002-5740-7747
C.-C. Lin https://orcid.org/0000-0002-7272-5129
T. B. Lowe https://orcid.org/0000-0002-9438-3617
M. E. MacLeod https://orcid.org/0000-0002-1417-8024
E. A. Magnier https://orcid.org/0000-0002-7965-2815
C. McCully https://orcid.org/0000-0001-5807-7893
P. Mínguez https://orcid.org/0009-0003-8803-8643
G. Narayan https://orcid.org/0000-0001-6022-0484
M. Newsome https://orcid.org/0000-0001-9570-0584
K. C. Patra https://orcid.org/0000-0002-1092-6806
A. Rest https://orcid.org/0000-0002-4410-5387
S. Rest https://orcid.org/0000-0002-3825-0553
S. Smartt https://orcid.org/0000-0002-8229-1731
K. W. Smith https://orcid.org/0000-0001-9535-3199
G. Terreran https://orcid.org/0000-0003-0794-5982
R. J. Wainscoat https://orcid.org/0000-0002-1341-0952
Q. Wang https://orcid.org/0000-0001-5233-6989
S. K. Yadavalli https://orcid.org/0000-0002-0840-6940
Y. Zenati https://orcid.org/0000-0002-0632-8897

References

Aamer, A., Nicholl, M., Jerkstrand, A., et al. 2024, MNRAS, 527, 11970
Abaroa, L., Romero, G. E., & Sotomayor, P. 2023, A&A, 671, A9
Aghakhanloo, M., Smith, N., Milne, P., et al. 2023, MNRAS, 521, 1941
Akeson, R., Armus, L., Bachelet, E., et al. 2019, arXiv:1902.05569
Akras, S., & López, J. A. 2012, MNRAS, 425, 2197
Alard, C. 2000, A&AS, 144, 363
Albareti, F. D., Allende Prieto, C., Almeida, A., et al. 2017, ApJS, 233, 25
Aleo, P. D., Engel, A. W., Narayan, G., et al. 2024, ApJ, 974, 172
Aleo, P. D., Malanchev, K., Sharief, S., et al. 2023, ApJS, 266, 9
Alfonso-Garzón, J., van den Eijnden, J., Kuin, N. P. M., et al. 2024, A&A, 683, A45
Allak, S., Akyuz, A., Sonbas, E., & Dhuga, K. S. 2022, MNRAS, 515, 3632
Allington-Smith, J., Breare, M., Ellis, R., et al. 1994, PASP, 106, 983
Alloin, D., Collin-Souffrin, S., Joly, M., & Vigroux, L. 1979, A&A, 78, 200
Angus, C. R., Woosley, S. E., Foley, R. J., et al. 2024, ApJL, 977, L41
Arcavi, I., Gal-Yam, A., Sullivan, M., et al. 2014, ApJ, 793, 38
Astropy Collaboration, Price-Whelan, A. M., Lim, P. L., et al. 2022, ApJ, 935, 167
Astropy Collaboration, Price-Whelan, A. M., Sipőcz, B. M., et al. 2018, AJ, 156, 123
Astropy Collaboration, Robitaille, T. P., Tollerud, E. J., et al. 2013, A&A, 558, A33
Baer-Way, R., Chandra, P., Modjaz, M., et al. 2025, ApJ, 983, 101
Bahramian, A., & Degenaar, N. 2023, Handbook of X-ray and Gamma-ray Astrophysics (Berlin: Springer), 120
Bak Nielsen, A.-S., Hjorth, J., & Gall, C. 2018, A&A, 611, A67
Becker, A. 2015, HOTPANTS: High Order Transform of PSF ANd Template Subtraction, Astrophysics Source Code Library, ascl:1504.004
Bednarek, W., & Pabich, J. 2011, A&A, 530, A49
Begelman, M. C. 2002, ApJL, 568, L97
Bellm, E. C., Kulkarni, S. R., Graham, M. J., et al. 2019, PASP, 131, 018002
Benetti, S., Chugai, N. N., Utrobin, V. P., et al. 2016, MNRAS, 456, 3296
Bertin, E., & Arnouts, S. 1996, A&AS, 117, 393
Berger, E., Foley, R., & Ivans, I. 2009, ATel, 2184, 1
Bertin, E., Mellier, Y., & Radovich, M. 2002, in ASP Conf. Ser. 281, Astronomical Data Analysis Software and Systems XI, ed. D. A. Bohlender, D. Durand, & T. H. Handley (San Francisco, CA: ASP), 228
Bilinski, C., Smith, N., Williams, G. G., et al. 2024, MNRAS, 529, 1104
Blanton, M. R., Bershady, M. A., Abolfathi, B., et al. 2017, AJ, 154, 28
Bollimpalli, D. A., Hameury, J. M., & Lasota, J. P. 2018, MNRAS, 481, 5422
Brennan, S. J., Fraser, M., Johansson, J., et al. 2022, MNRAS, 513, 5642
Brennan, S. J., Schulze, S., Lunnan, R., et al. 2024b, A&A, 690, A259
Brennan, S. J., Sollerman, J., Irani, I., et al. 2024a, A&A, 684, L18
Brightman, M., Bachetti, M., Earnshaw, H. P., et al. 2019, BAAS, 51, 352
Brown, P. J., Kuin, P., Scalzo, R., et al. 2014, ApJ, 787, 29
Brown, T. M., Baliber, N., Bianco, F. B., et al. 2013, PASP, 125, 1031
Calzetti, D., Armus, L., Bohlin, R. C., et al. 2000, ApJ, 533, 682
Cassinelli, J. P., & Ignace, R. 1997, in ASP Conf. Ser. 120, Luminous Blue Variables: Massive Stars in Transition, ed. A. Nota & H. Lamers (San Francisco, CA: ASP), 166
Chabrier, G. 2003, PASP, 115, 763
Chambers, K. C., Magnier, E. A., Metcalfe, N., et al. 2016, arXiv:1612.05560
Chandra, P., Chevalier, R. A., Chugai, N., Fransson, C., & Soderberg, A. M. 2015, ApJ, 810, 32
Chatzopoulos, E., Wheeler, J. C., & Vinko, J. 2012, ApJ, 746, 121
Chen, P., Gal-Yam, A., Sollerman, J., et al. 2024, Natur, 625, 253
Chevalier, R. A. 1982, ApJ, 258, 790
Chevalier, R. A. 2012, ApJL, 752, L2
Choi, J., Dotter, A., Conroy, C., et al. 2016, ApJ, 823, 102
Chugai, N. N. 2009, MNRAS, 400, 866
Chugai, N. N., Blinnikov, S. I., Cumming, R. J., et al. 2004, MNRAS, 352, 1213
Chugai, N. N., & Utrobin, V. P. 2023, AstL, 49, 639
Coe, M. J., Kennea, J. A., Monageng, I. M., et al. 2023, MNRAS, 524, 3263
Colgate, S. A., & McKee, C. 1969, ApJ, 157, 623
Conroy, C., & Gunn, J. E. 2010, FSPS: Flexible Stellar Population Synthesis, Astrophysics Source Code Library, ascl:1010.043
Conroy, C., Gunn, J. E., & White, M. 2009, ApJ, 699, 486
Coulter, D. A., Jones, D. O., McGill, P., et al. 2022, An Open-source Target and Observation Management System, v0.3.0, doi:10.5281/zenodo.7278430
Coulter, D. A., Jones, D. O., McGill, P., et al. 2023, PASP, 135, 064501
Danehkar, A. 2022, ApJS, 260, 14
Das, K. K., Kasliwal, M. M., Sollerman, J., et al. 2024, ApJ, 972, 91
Davidson, K. 2020, Galax, 8, 10
Davidson, K., Ebbets, D., Johansson, S., et al. 1997, AJ, 113, 335
Dekany, R., Smith, R. M., Riddle, R., et al. 2020, PASP, 132, 038001
Dessart, L., Hillier, D. J., Gezari, S., Basa, S., & Matheson, T. 2009, MNRAS, 394, 21
Dey, A., Schlegel, D. J., Lang, D., et al. 2019, AJ, 157, 168
Dickinson, D., Smith, N., Andrews, J. E., et al. 2024, MNRAS, 527, 7767
Dong, Y., Tsuna, D., Valenti, S., et al. 2024, ApJ, 977, 254
Dotter, A. 2016, ApJS, 222, 8
Drake, A. J., Howerton, S., McNaught, R., et al. 2012, ATel, 4334, 1
Drake, S. A., & Ulrich, R. K. 1980, ApJS, 42, 351
Duarte, J., Gonzalez-Gaitan, S., Gutierrez, C., & Bruch, R. J. 2024, ePESSTO + Transient Classification Report for 2024-07-13 2024-2424, 2024-2424
Dwarkadas, V. V. 2011, MNRAS, 412, 1639
Dwarkadas, V. V., & Owocki, S. P. 2001, AAS Meeting, 199, 135.09
Elias-Rosa, N., Pastorello, A., Benetti, S., et al. 2016, MNRAS, 463, 3894
Elias-Rosa, N., Van Dyk, S. D., Benetti, S., et al. 2018, ApJ, 860, 68

Ercolino, A., Jin, H., Langer, N., & Dessart, L. 2024, A&A, 685, A58
Fabrika, S., Ueda, Y., Vinokurov, A., Sholukhova, O., & Shidatsu, M. 2015, NatPh, 11, 551
Falcón-Barroso, J., Sánchez-Blázquez, P., Vazdekis, A., et al. 2011, A&A, 532, A95
Farias, D., Gall, C., Narayan, G., et al. 2024, ApJ, 977, 152
Fernández, R., Kasen, D., Metzger, B. D., & Quataert, E. 2015, MNRAS, 446, 750
Filippenko, A. V. 1989, AJ, 97, 726
Filippenko, A. V. 1997, ARA&A, 35, 309
Folatelli, G., Contreras, C., Phillips, M. M., et al. 2006, ApJ, 641, 1039
Foley, R. J., Berger, E., Fox, O., et al. 2011, ApJ, 732, 32
Foley, R. J., Smith, N., Ganeshalingam, M., et al. 2007, ApJL, 657, L105
Foreman-Mackey, D. 2016, JOSS, 1, 24
Fox, O. D., Chevalier, R. A., Skrutskie, M. F., et al. 2011, ApJ, 741, 7
Fox, O. D., Khandrika, H., Rubin, D., et al. 2021, MNRAS, 506, 4199
Frank, A., Balick, B., & Davidson, K. 1995, ApJL, 441, L77
Fransson, C., Ergon, M., Challis, P. J., et al. 2014, ApJ, 797, 118
Fransson, C., Sollerman, J., Strotjohann, N. L., et al. 2022, A&A, 666, A79
Fraser, M., Inserra, C., Jerkstrand, A., et al. 2013, MNRAS, 433, 1312
Fremling, C. 2023, TNSTR, 2023-3189, 1
Fuller, J. 2017, MNRAS, 470, 1642
Fuller, J., & Ro, S. 2018, MNRAS, 476, 1853
Gagliano, A., Berger, E., Villar, V. A., et al. 2025, ApJ, 978, 110
Gagliano, A., Narayan, G., Engel, A., Carrasco Kind, M. & LSST Dark Energy Science Collaboration 2021, ApJ, 908, 170
Gal-Yam, A. 2012, Sci, 337, 927
Gal-Yam, A., Bruch, R., Schulze, S., et al. 2022, Natur, 601, 201
Gal-Yam, A., & Leonard, D. C. 2009, Natur, 458, 865
Gal-Yam, A., Yaron, O., Pastorello, A., et al. 2021, TNSAN, 76, 1
Galbany, L., Stanishev, V., Mourão, A. M., et al. 2016, A&A, 591, A48
Gall, C., Andersen, A. C., & Hjorth, J. 2011, A&A, 528, A14
Gall, C., Hjorth, J., Watson, D., et al. 2014, Natur, 511, 326
Gallazzi, A., Charlot, S., Brinchmann, J., White, S. D. M., & Tremonti, C. A. 2005, MNRAS, 362, 41
Gallegos-Garcia, M., Berry, C. P. L., Marchant, P., & Kalogera, V. 2021, ApJ, 922, 110
Gallegos-Garcia, M., Jacquemin-Ide, J., & Kalogera, V. 2024, ApJ, 973, 168
Gangopadhyay, A., Dukiya, N., Moriya, T. J., et al. 2025, MNRAS, 537, 2898
Gangopadhyay, A., Misra, K., Hiramatsu, D., et al. 2020, ApJ, 889, 170
Gangopadhyay, A., Misra, K., Kawabata, K., Dastidar, R., & Singh, M. 2022, JApA, 43, 51
Garcia-Segura, G., Langer, N., & Mac Low, M. M. 1997, in ASP Conf. Ser. 120, Luminous Blue Variables: Massive Stars in Transition, ed. A. Nota & H. Lamers (San Francisco, CA: ASP), 332
Gardner, J. P., Mather, J. C., Clampin, M., et al. 2006, SSRv, 123, 485
Gomez, S. 2024, gmzsebastian/redspec: redspec, v0.1, doi:10.5281/zenodo.14291063
Gomez, S., Berger, E., Hosseinzadeh, G., et al. 2021, ApJ, 913, 143
Gomez, S., Berger, E., Nicholl, M., Blanchard, P. K., & Hosseinzadeh, G. 2022, ApJ, 941, 107
Gomez, S., Berger, E., Nicholl, M., et al. 2019, ApJ, 881, 87
Gordon, K. D., Clayton, G. C., Decleir, M., et al. 2023, ApJ, 950, 86
Gormaz-Matamala, A. C., Romagnolo, A., & Belczynski, K. 2025, A&A, 696, A72
Graham, M. L., Bigley, A., Mauerhan, J. C., et al. 2017, MNRAS, 469, 1559
Graham, M. L., Sand, D. J., Valenti, S., et al. 2014, ApJ, 787, 163
Groh, J. H., Damineli, A., Hillier, D. J., et al. 2009, ApJL, 705, L25
Groh, J. H., Hillier, D. J., Madura, T. I., & Weigelt, G. 2012, MNRAS, 423, 1623
Guevel, D., & Hosseinzadeh, G. 2017, dguevel/PyZOGY: Initial release, v0.0.1, doi:10.5281/zenodo.1043973
Guillochon, J., Nicholl, M., Villar, V. A., et al. 2018, ApJS, 236, 6
Gutiérrez, C. P., Bersten, M. C., Orellana, M., et al. 2021, MNRAS, 504, 4907
Habergham, S. M., Anderson, J. P., James, P. A., & Lyman, J. D. 2014, MNRAS, 441, 2230
Hameury, J. M. 2020, AdSpR, 66, 1004
Harris, C. R., Millman, K. J., van der Walt, S. J., et al. 2020, Natur, 585, 357
Hart, S. 1989, in Shapley Value, ed. J. Eatwell, M. Milgate, & P. Newman (London: Macmillan), 210
Henden, A. A., Templeton, M., Terrell, D., et al. 2016, ycat, 2336
Hillier, D. J., Davidson, K., Ishibashi, K., & Gull, T. 2001, ApJ, 553, 837
Hiramatsu, D., Berger, E., Gomez, S., et al. 2024a, arXiv:2411.07287
Hiramatsu, D., Matsumoto, T., Berger, E., et al. 2024b, ApJ, 964, 181
Hosseinzadeh, G., Arcavi, I., Valenti, S., et al. 2017, ApJ, 836, 158
Howell, D. A. 2017, AAS Meeting, 230, 318.03
Huang, C., & Chevalier, R. A. 2018, MNRAS, 475, 1261
Humphreys, R. M., & Davidson, K. 1994, PASP, 106, 1025
Hunter, J. D. 2007, CSE, 9, 90
Immler, S., Brown, P. J., Milne, P., et al. 2006, ApJL, 648, L119
Israelian, G., & de Groot, M. 1999, SSRv, 90, 493
Jacobson-Galán, W., Margutti, R., Orzechowski, G., Terreran, G., & Berton, M. 2021, TNSAN, 288, 1
Jacobson-Galán, W. V., Davis, K. W., Kilpatrick, C. D., et al. 2024, ApJ, 972, 177
Jacobson-Galán, W. V., Dessart, L., Jones, D. O., et al. 2022, ApJ, 924, 15
Jencson, J. E., Sand, D. J., Andrews, J. E., et al. 2022, ApJL, 935, L33
Jiang, B., Jiang, S., & Ashley Villar, V. 2020, RNAAS, 4, 16
Jiang, Y.-F., Cantiello, M., Bildsten, L., et al. 2018, Natur, 561, 498
Johnson, B. D., Leja, J., Conroy, C., & Speagle, J. S. 2021, ApJS, 254, 22
Jones, D. O., Foley, R. J., Narayan, G., et al. 2021, ApJ, 908, 143
Jones, D. O., McGill, P., Manning, T. A., et al. 2024, arXiv:2410.17322
Kangas, T., Kuncarayakti, H., Nagao, T., et al. 2024, A&A, 689, A182
Kashi, A. 2010, arXiv:1009.4307
Kessler, R., Bernstein, J. P., Cinabro, D., et al. 2009, PASP, 121, 1028
Khakpash, S., Bianco, F. B., Modjaz, M., et al. 2024, ApJS, 275, 37
Khan, N., & Middleton, M. J. 2023, MNRAS, 524, 4302
Khatami, D. K., & Kasen, D. N. 2024, ApJ, 972, 140
Kilpatrick, C. D., Foley, R. J., Drout, M. R., et al. 2018, MNRAS, 473, 4805
Kilpatrick, C. D., Foley, R. J., Jacobson-Galán, W. V., et al. 2023, ApJL, 952, L23
Klencki, J., Nelemans, G., Istrate, A. G., & Pols, O. 2020, A&A, 638, A55
Kool, E. C., Karamehmetoglu, E., Sollerman, J., et al. 2021, A&A, 652, A136
Kriek, M., & Conroy, C. 2013, ApJL, 775, L16
Kuncarayakti, H., Sollerman, J., Izzo, L., et al. 2023, A&A, 678, A209
Langer, N. 1997, in ASP Conf. Ser. 120, Luminous Blue Variables: Massive Stars in Transition, ed. A. Nota & H. Lamers (San Francisco, CA: ASP), 83
Laplace, E., Götberg, Y., de Mink, S. E., Justham, S., & Farmer, R. 2020, A&A, 637, A6
Layton, J. T., Blondin, J. M., Owen, M. P., & Stevens, I. R. 1998, NewA, 3, 111
Leja, J., Carnall, A. C., Johnson, B. D., Conroy, C., & Speagle, J. S. 2019, ApJ, 876, 3
Leonard, D. C., Filippenko, A. V., Barth, A. J., & Matheson, T. 2000, ApJ, 536, 239
Leung, S.-C., & Fuller, J. 2020, ApJ, 900, 99
Levesque, E. M., Stringfellow, G. S., Ginsburg, A. G., Bally, J., & Keeney, B. A. 2014, AJ, 147, 23
Lignieres, F., Catala, C., & Mangeney, A. 2000, arXiv:astro-ph/0002026
Lundberg, S., & Lee, S.-I. 2017, arXiv:1705.07874
MacLeod, M., & Loeb, A. 2020a, ApJ, 895, 29
MacLeod, M., & Loeb, A. 2020b, ApJ, 893, 106
MacLeod, M., Ostriker, E. C., & Stone, J. M. 2018a, ApJ, 863, 5
MacLeod, M., Ostriker, E. C., & Stone, J. M. 2018b, ApJ, 868, 136
Magnier, E. A., Chambers, K. C., Flewelling, H. A., et al. 2020a, ApJS, 251, 3
Magnier, E. A., Sweeney, W. E., Chambers, K. C., et al. 2020b, ApJS, 251, 5
Malanchev, K. L., Pruzhinskaya, M. V., Korolev, V. S., et al. 2021, MNRAS, 502, 5147
Marchant, P., Pappas, K. M. W., Gallegos-Garcia, M., et al. 2021, A&A, 650, A107
Margutti, R., Milisavljevic, D., Soderberg, A. M., et al. 2014, ApJ, 780, 21
Martin, D. C., Fanson, J., Schiminovich, D., et al. 2005, ApJL, 619, L1
Martin, J. C., Hambsch, F.-J., Margutti, R., et al. 2014, AJ, 149, 9
Martins, F. 2023, A&A, 680, A22
Masci, F. J., Laher, R. R., Rusholme, B., et al. 2019, PASP, 131, 018003
Masci, F. J., Laher, R. R., Rusholme, B., et al. 2023, arXiv:2305.16279
Matheson, T., Stubens, C., Wolf, N., et al. 2021, AJ, 161, 107
Matsumoto, T., & Metzger, B. D. 2022, ApJ, 936, 114
Matsuoka, T., & Sawada, R. 2024, ApJ, 963, 105
Matzner, C. D., & McKee, C. F. 1999, ApJ, 510, 379
Mauerhan, J., & Smith, N. 2012, MNRAS, 424, 2659
Mauerhan, J. C., Smith, N., Filippenko, A. V., et al. 2013, MNRAS, 430, 1801
Maza, J., Hamuy, M., Antezana, R., et al. 2009, CBET, 1928, 1
Metzger, B. D. 2022, ApJ, 932, 84
Miller, A. A., Silverman, J. M., Butler, N. R., et al. 2010, MNRAS, 404, 305
Mineshige, S. 1986, PASJ, 38, 831
Miniutti, G., Ponti, G., Dadina, M., et al. 2006, MNRAS, 373, L1
Moriya, T. J. 2015, ApJL, 803, L26
Moriya, T. J., Galbany, L., Jiménez-Palau, C., et al. 2023, A&A, 677, A20
Moriya, T. J., Maeda, K., Taddia, F., et al. 2013, MNRAS, 435, 1520
Moriya, T. J., Maeda, K., Taddia, F., et al. 2014, MNRAS, 439, 2917
Morris, T., & Podsiadlowski, P. 2006, MNRAS, 365, 2

Muñoz, D. J., & Lai, D. 2016, ApJ, 827, 43

Nugent, A. E., Fong, W., Dong, Y., et al. 2020, ApJ, 904, 52

Nugent, A. E., Fong, W.-F., Dong, Y., et al. 2022, ApJ, 940, 57

Nyholm, A., Sollerman, J., Tartaglia, L., et al. 2020, A&A, 637, A73

Ofek, E. O., Sullivan, M., Cenko, S. B., et al. 2013, Natur, 494, 65

Osterbrock, D. E., & Ferland, G. J. 2006, Astrophysics of Gaseous Nebulae and Active Galactic Nuclei (Sausalito, CA: Univ. Science Books)

Panagiotou, C., & Walter, R. 2018, A&A, 610, A37

pandas development team T. 2024, pandas-dev/pandas: Pandas, v2.2.2, doi:10.5281/zenodo.10957263

Panjkov, S., Auchettl, K., Shappee, B. J., et al. 2024, PASA, 41, e059

Pastorello, A., Benetti, S., Brown, P. J., et al. 2015, MNRAS, 449, 1921

Pastorello, A., Cappellaro, E., Inserra, C., et al. 2013, ApJ, 767, 1

Pastorello, A., Kochanek, C. S., Fraser, M., et al. 2018, MNRAS, 474, 197

Pastorello, A., Mattila, S., Zampieri, L., et al. 2008a, MNRAS, 389, 113

Pastorello, A., Quimby, R. M., Smartt, S. J., et al. 2008b, MNRAS, 389, 131

Pavlovskii, K., Ivanova, N., Belczynski, K., & Van, K. X. 2017, MNRAS, 465, 2092

Paxton, B., Bildsten, L., Dotter, A., et al. 2011, ApJS, 192, 3

Paxton, B., Cantiello, M., Arras, P., et al. 2013, ApJS, 208, 4

Paxton, B., Marchant, P., Schwab, J., et al. 2015, ApJS, 220, 15

Pellegrino, C., Howell, D. A., Terreran, G., et al. 2022, ApJ, 938, 73

Pessi, T., Cartier, R., Hueichapan, E., et al. 2024, A&A, 688, L28

Pessi, T., Prieto, J. L., & Dessart, L. 2023, A&A, 677, L1

Prieto, J. L., Brimacombe, J., Drake, A. J., & Howerton, S. 2013, ApJL, 763, L27

Prieto, J. L., Kistler, M. D., Thompson, T. A., et al. 2008, ApJ, 681, L9

Prochaska, J. X., Hennawi, J. F., Westfall, K. B., et al. 2020, JOSS, 5, 2308

Qin, Y.-J., & Zabludoff, A. 2024, MNRAS, 533, 3517

Quataert, E., & Shiode, J. 2012, MNRAS, 423, L92

Rakavy, G., & Shaviv, G. 1967, ApJ, 148, 803

Ralchenko, Y., & Kramida, A. 2020, Atoms, 8, 56

Ransome, C. L., Habergham-Mawson, S. M., Darnley, M. J., James, P. A., & Percival, S. M. 2022, MNRAS, 513, 3564

Ransome, C. L., & Villar, V. A. 2025, ApJ, 987, 13

Regös, E., Bailey, V. C., & Mardling, R. 2005, MNRAS, 358, 544

Reguitti, A., Pignata, G., Pastorello, A., et al. 2024, A&A, 686, A231

Reilly, E., Maund, J. R., Baade, D., et al. 2017, MNRAS, 470, 1491

Rest, A., Stubbs, C., Becker, A. C., et al. 2005, ApJ, 634, 1103

Rest, A., Scolnic, D., Foley, R. J., et al. 2014, ApJ, 795, 44

Rest, S., Rest, A., Kilpatrick, C. D., et al. 2025, ApJ, 979, 114

Roming, P. W. A., Kennedy, T. E., Mason, K. O., et al. 2005, SSRv, 120, 95

Saio, H. 2009, in Proc. of the 38th Liege International Astrophysical Colloquium: Evolution and Pulsation of Massive Stars on the Main Sequence and Close to it, ed. A. Noels, C. Aerts, J. Montalban et al. (Vienna: Austrian Academy of Sciences Press), 245

Sana, H., de Mink, S. E., de Koter, A., et al. 2012, Sci, 337, 444

Sánchez-Blázquez, P., Peletier, R. F., Jiménez-Vicente, J., et al. 2006, MNRAS, 371, 703

Schlafly, E. F., & Finkbeiner, D. P. 2011, ApJ, 737, 103

Schlegel, E. M. 1990, MNRAS, 269, 244

Schrøder, S. L., MacLeod, M., Loeb, A., Vigna-Gómez, A., & Mandel, I. 2020, ApJ, 892, 13

Schulze, S., Yaron, O., Sollerman, J., et al. 2021, ApJS, 255, 29

Sharma, Y., Sollerman, J., Kulkarni, S. R., et al. 2024, ApJ, 966, 199

Shen, R. F., Barniol Duran, R., Nakar, E., & Piran, T. 2015, MNRAS, 447, L60

Shingles, L., Smith, K. W., Young, D. R., et al. 2021, TNSAN, 7, 1

Shiode, J. H., & Quataert, E. 2014, ApJ, 780, 96

Shivvers, I., Groh, J. H., Mauerhan, J. C., et al. 2015, ApJ, 806, 213

Skrutskie, M. F., Cutri, R. M., Stiening, R., et al. 2006, AJ, 131, 1163

Smith, K. W., Smartt, S. J., Young, D. R., et al. 2020, PASP, 132, 085002

Smith, N. 2014, ARA&A, 52, 487

Smith, N. 2017a, RSPTA, 375, 20160268

Smith, N. 2017b, in Handbook of Supernovae, ed. A. W. Alsabti & P. Murdin (Berlin: Springer)

Smith, N., Andrews, J. E., Filippenko, A. V., et al. 2022, MNRAS, 515, 71

Smith, N., & Arnett, W. D. 2014, ApJ, 785, 82

Smith, N., & Conti, P. S. 2008, ApJ, 679, 1467

Smith, N., Foley, R. J., & Filippenko, A. V. 2008, ApJ, 680, 568

Smith, N., Li, W., Miller, A. A., et al. 2011b, ApJ, 732, 63

Smith, N., Li, W., Silverman, J. M., Ganeshalingam, M., & Filippenko, A. V. 2011a, MNRAS, 415, 773

Smith, N., Mauerhan, J. C., & Prieto, J. L. 2013, MNRAS, 438, 1191

Smith, N., Mauerhan, J. C., Silverman, J. M., et al. 2012a, MNRAS, 426, 1905

Smith, N., Miller, A., Li, W., et al. 2010, AJ, 139, 1451

Smith, N., Silverman, J. M., Filippenko, A. V., et al. 2012b, AJ, 143, 17

Smith, N., & Tombleson, R. 2014, MNRAS, 447, 598

Soker, N., & Kashi, A. 2013, ApJL, 764, L6

Speagle, J. S. 2020, MNRAS, 493, 3132

Strotjohann, N. L., Ofek, E. O., Gal-Yam, A., et al. 2021, ApJ, 907, 99

Suzuki, A., Moriya, T. J., & Takiwaki, T. 2019, ApJ, 887, 249

Taddia, F., Stritzinger, M. D., Bersten, M., et al. 2018, A&A, 609, A136

Taddia, F., Stritzinger, M. D., Fransson, C., et al. 2020, A&A, 638, A92

Taddia, F., Stritzinger, M. D., Sollerman, J., et al. 2013, A&A, 555, A10

Thomas, B. P., Wheeler, J. C., Dwarkadas, V. V., et al. 2022, ApJ, 930, 57

Thompson, T. A., Prieto, J. L., Stanek, K. Z., et al. 2009, ApJ, 705, 1364

Thöne, C. C., de Ugarte Postigo, A., Leloudas, G., et al. 2017, A&A, 599, A129

Tonry, J. L., Denneau, L., Heinze, A. N., et al. 2018, PASP, 130, 064505

Tsuna, D., Wu, S. C., Fuller, J., Dong, Y., & Piro, A. L. 2024, OJAp, 7, 82

Valenti, S., Howell, D. A., Stritzinger, M. D., et al. 2016, MNRAS, 459, 3939

van Marle, A. J., Langer, N., & García-Segura, G. 2005, A&A, 444, 837

Villar, V. A., Berger, E., Metzger, B. D., & Guillochon, J. 2017, ApJ, 849, 70

Virtanen, P., Gommers, R., Oliphant, T. E., et al. 2020, NatMe, 17, 261

Waskom, M. L. 2021, JOSS, 6, 3021

Wegner, G., & Swanson, S. R. 1996, MNRAS, 278, 22

Weng, S.-S., & Zhang, S.-N. 2011, ApJ, 739, 42

Willcox, R., MacLeod, M., Mandel, I., & Hirai, R. 2023, ApJ, 958, 138

Willingale, R., Starling, R. L. C., Beardmore, A. P., Tanvir, N. R., & O'Brien, P. T. 2013, MNRAS, 431, 394

Woosley, S. E., Heger, A., & Weaver, T. A. 2002, RvMP, 74, 1015

Wu, S. C., & Fuller, J. 2022, ApJL, 940, L27

Yaron, O., & Gal-Yam, A. 2012, PASP, 124, 668

York, D. G., Adelman, J., Anderson, J. E., Jr., et al. 2000, AJ, 120, 1579

Young, D. 2023, panstamps, v0.6.2, doi:10.5281/zenodo.8037665

Zamanov, R. K., Stoyanov, K. A., Marchev, D., et al. 2022, AN, 343, e24019

Zapata, L. A., Loinard, L., Fernández-López, M., et al. 2022, ApJ, 935, 76

Zhao, X., & Fuller, J. 2020, MNRAS, 495, 249